A NEUTRAL HYDROGEN LINE RECEIVER FOR THE FLEURS SYNTHESIS TELESCOPE

A Thesis

Presented to

the Faculty of the School of Electrical Engineering

University of Sydney

In Fulfillment

of the Requirements for the Degree

Doctor of Philosophy

by

Henry Yao

March 1983

PREFACE

This thesis is the result of a project in providing the Fleurs Synthesis Telescope with the capability of mapping radiation from neutral hydrogen in galaxies outside the Milky Way. The instrument is the first of its kind in the Southern Hemisphere and lays the foundation for high resolution studies of the kinematics and dynamics of galaxies. Angular structures down to 1.3' can be mapped with a velocity resolution of 30 km/s. The author carried the project from its conceptual stage, through design, construction and operation of the instrument. A spiral galaxy in the southern sky was studied.

Chapter I is introduced by the quest of high angular resolution telescopes in the astronomical world leading to the development of the theory of aperture synthesis. The theory was developed with special attention to Earth rotational synthesis having line arrays arranged in an EW and a NS configuration. Synthesised beam patterns were studied leading to the beamwidth dependence on sky coordinates. Brightness temperature scales were developed. Evaluation of the data sampling requirement led to the possibility of trading instrument sensitivity for observation speed.

Chapter II covers the design and construction of the Fleurs neutral hydrogen spectrometer. General concept of the instrument was discussed. The spectrometer was designed with a low level of hardware change and efficient use of existing correlator channels. The instrument used analogue filters as velocity band-select

elements. The construction of the filters and the reconfiguration of the original Fleurs system were the responsibility of the author. The author analysed the spectrometer in terms of bandwidth, noise and dynamic range. Effect of imperfect delay tracking on correlators was studied. Possible performance of the new instrument was presented. Future improvement to the instrument was proposed.

Chapter III includes the necessary procedures to obtain a successful observation. The author developed data reduction software to accommodate special requirements of the neutral hygrogen data. Calibration procedures were discussed in connection with multi-frequency measurements.

Chapter IV presents the results from an observation of N300. System performance was evaluated by the observation of point sources. Parameters for N300 were evaluated and compared with other low angular resolution measurements. The neutral hydrogen distribution and the velocity field of N300 were presented. Models of velocity fields were given in Appendix B.

Chapter V discusses sources of interference and their effect on aperture synthesis data. The author investigated two particular cases in detail, interference generated within the spectrometer and interference from external sources. A mathematical basis was developed for each of the cases.

ACKNOWLEDGEMENTS

This thesis results from work by the author under the supervision of Dr R. H. Frater. Prof. T. W. Cole provided valuable guidance during the final stages of writing since Dr Frater's departure to CSIRO. Thanks go to Dr K. J. Wellington for his helpful suggestions in the design of the line receiver. Thanks also to Dr C. K. Kwong for his HI observation control software and Dr C. F. Chen for his CLEAN machine. This work cannot progress without the help of Mr A. Watkinson and the staff at the Fleurs Radio Observatory. Special thanks are extended to Mr G. R. Graves. Help from Mr R. Gough, Mrs D. S. Retallack and Miss N. Strevens during the preliminary stages of data reduction is appreciated. Staff support from the Faculty of Engineering Computing Center is noted. The work was supported during the period 1974 to 1977 by a University Research Studentship.

CONTENTS

CHAPTER I APERTURE SYNTHESIS

1.1 Radio Telescopes

During 1931, a radio engineer from the Bell Telephones Laboratories, K. G. Jansky, was studying the direction of arrival of thunderstorm statics. One result of the study was that he recognised some electrical disturbances as of extraterrestrial origin (1933). The antenna he used operated at a frequency of 20.5 MHz and had a fan beam of approximately 30 degrees in width.

Since that time, it has been realised that radio waves of extraterrestrial origin illuminate the Earth over a broad frequency range, from under 30 MHz to over 30 GHz. Through this radio window, scientists have gathered new information about the universe. Astronomers have long been studying the sky through the optical window using optical telescopes. Similarly, radio telescopes were and are being developed for use over the radio window. Jansky's telescope had a half power beamwidth of 30 degrees in the narrower direction. It will resolve any structures separated by 30 degrees in that direction. Clearly this will only provide limited information about the sky. One problem in radio astronomy has been to achieve better angular resolution.

One method which does not involve any modification to the telescope is occultation. An object with a well defined edge is made to pass in front of the source under observation. From the diffraction pattern generated, it is possible to deduce structures down

to 1" arc. The Moon has been used as such a knife edge. However, the application of this method is rather limited.

The more common method of achieving better angular resolution is to build better telescopes. The beam pattern of a telescope and its aperture distribution form a Fourier transform pair. A property of the transform is that the product of the corresponding quantities in the two domains is a constant. A large quantity in the aperture domain will produce a small quantity in the pattern domain, meaning better angular resolution. One way to increase the effective aperture is to operate the telescope at a higher frequency, reducing the wavelength. This requires better surfaces for the telescope. The improvement in resolution in this case is limited by the atmospheric turbulence. Thus, at optical frequencies, the resolution is at best 1" arc on the ground. This figure can improve if the telescope is outside the Earth's atmosphere. Given a fixed physical aperture, a certain resolution can only be achieved at a certain frequency.

Another way to increase the effective aperture is to increase its physical dimensions. At a fixed frequency, it is then possible to get better resolution. However, there is a limit to the sizes of apertures that can be built. The spherical reflector at Arecibo has a diameter of 305 meters and operates at up to 2380 MHz with a 2.7' arc resolution (LaLonde 1974). A variable profile design has been used for RATAN-600 of the Special Astrophysical Observatory (Belitzky 1976).

It is composed of multiple independently adjustable reflecting elements which simulate a section of a large reflector. It is 576 meters in diameter and at 15 GHz has a resolution of 12" × 1.2'. These large aperture instruments have limited tracking ability.

It is not necessary to have very large filled apertures to achieve good angular resolution. An interferometer with a spacing equal to the diameter of the filled aperture can achieve a similar result. The tradeoff is in sensitivity. It also produces a rather elongated beam. Experiments with very long baseline interferometry have been carried out with resolution down to 0.1 milliarc seconds (Batchelor et al. 1976).

To map a radiation field in the sky, it is necessary in the filled aperture case to point the beam at various portions of the region under investigation. It is also possible to map the sky using interferometers. Recall again the Fourier relationship between the beam pattern and the aperture distribution of a telescope. This is a special case of the general relationship between the sky distribution and the aperture distribution. When the radiation field is concentrated within a region of the sky, sampling theorem says that it can be uniquely and completely determined by appropriate discrete measurements on the aperture domain. This unfilled aperture can be constructed by interferometers. The fact that an infinite spacing is not available in practice limits the angular resolution that can be achieved. The resolution is essentially determined

by the longest spacing present. The required spacings to perform the measurements can be generated by movable antennas and by the rotation of the Earth. The Cambridge 5 km telescope has four fixed and four movable antennas to produce a resolution of 2" arc at 5 GHz (Ryle 1975).

1.2 Fleurs Synthesis Telescope

The Fleurs Synthesis Telescope (FST) is an Earth rotational synthesis telescope operating at 1.4 GHz with an angular resolution of 40" arc. Its latitude is at 33.8625 degrees south of the equator. There are two perpendicular fixed arrays, one in the eastwest (EW) direction, and the other in the northsouth (NS) direction (Figure 1-1). Each array has thirty two 5.5 meter and two 13.7 meter parabolic antennas. The antennas are equatorially mounted with a nominal tracking range of 4 hours before transit to 4 hours after transit.

Each array can be used as a set of sixty four interferometers. An interferometer is formed by one of the large antennas and one of the small antennas. the available spacings are given by $(i + \frac{1}{2})d$, with i an integer ranging from 1 to 64. Each measurement point is integrated over one minute, producing 480 x 64 sample points per eight hour observation.

1.3 Coordinate System

To facilitate discussions on certain properties of an aperture synthesis telescope, a coordinate system needs to be defined. The system to be used has the three axes designated as X, Y, and Z (Figure 1-2).

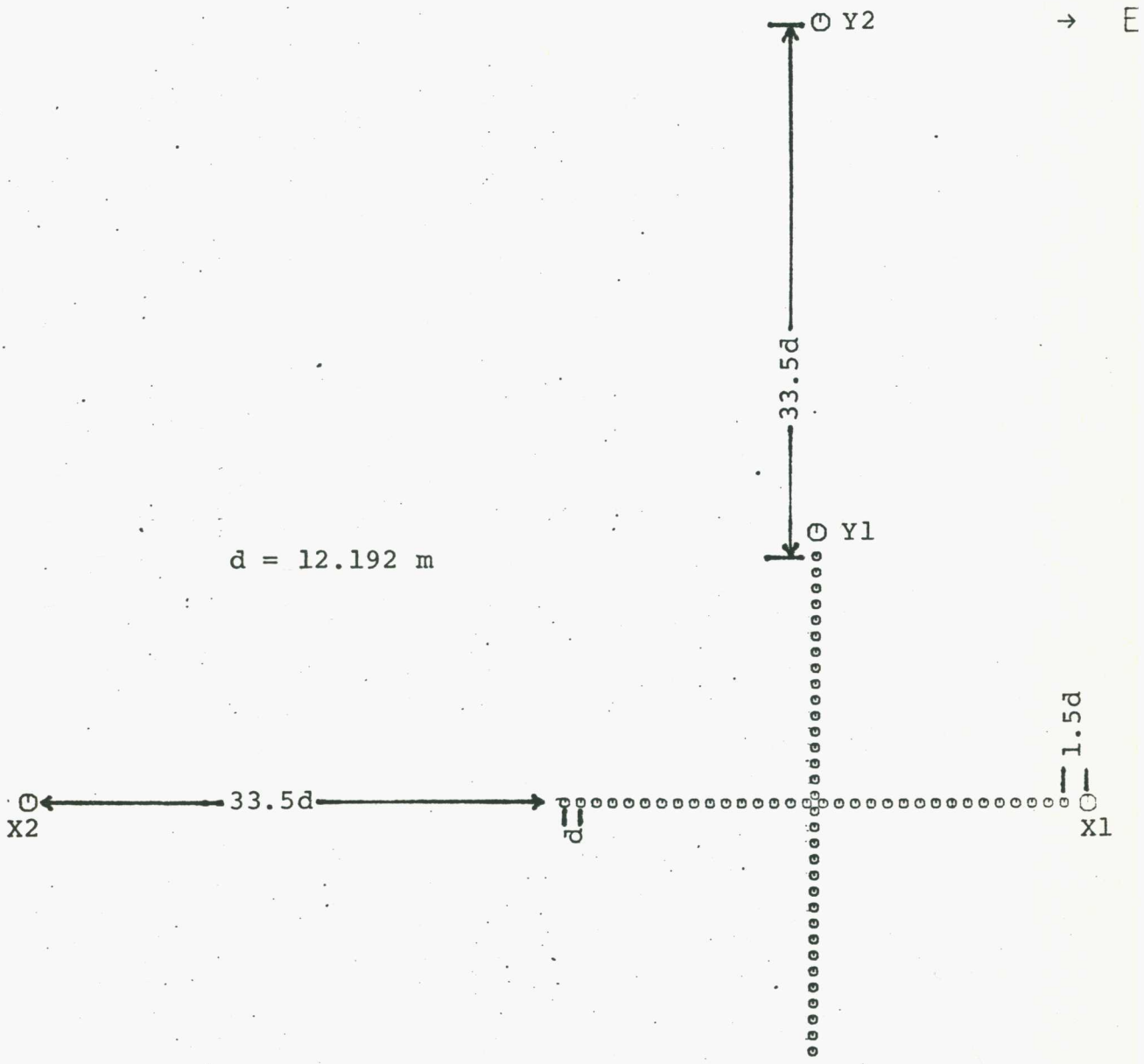

Figure 1-1 FST Layout

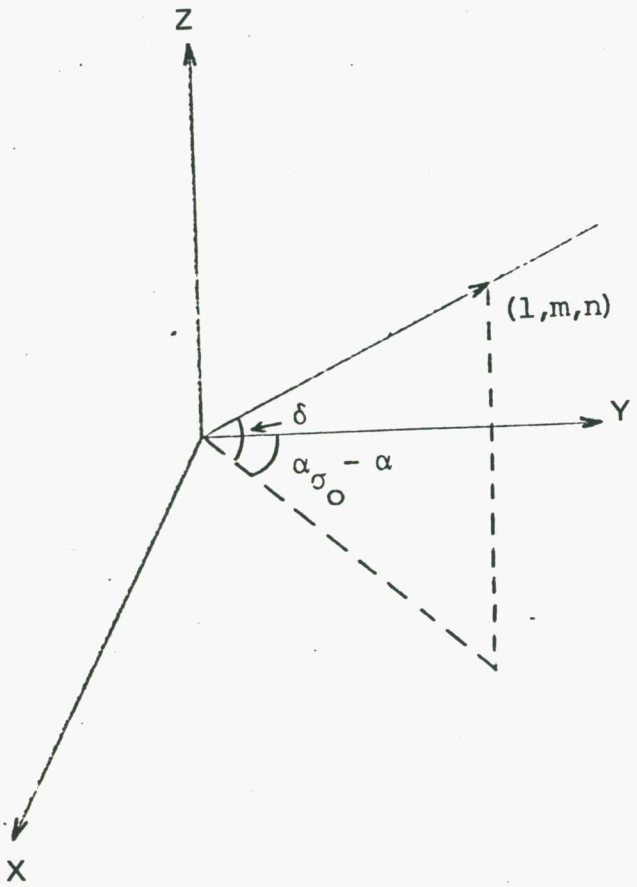

Figure 1-2 Coordinate System

The Z axis points towards the north celestial pole and the YZ plane is positioned such that it passes through the synthesis field center in the sky. Such a system is thus a function of the right ascension of the synthesis center. An interferometer fixed on Earth moves in an anticlockwise direction around the Z axis in time.

The sky coordinates are defined by a corresponding set of direction cosines l, m, and n. A radiation field is defined on the surface of a unit sphere and the following relationship holds,

$$l^2 + m^2 + n^2 = 1 \qquad (1\text{-}1)$$

The direction cosines can be expressed in terms of the equatorial coordinates α (right ascension) and δ (declination),

$$\begin{aligned} l &= -\cos(\delta)\sin(\alpha - \alpha_{\sigma_o}) \\ m &= \cos(\delta)\cos(\alpha - \alpha_{\sigma_o}) \\ n &= \sin(\delta) \end{aligned} \qquad (1\text{-}2)$$

where σ_o denotes the synthesis center.

1.4 Formulation of Aperture Synthesis

The basic technique of aperture synthesis is to utilise discrete pairs of antennas to measure the spatial frequencies which characterise the radiation of interest. A set of these measurements is then manipulated to produce a distribution of the strength of the radiation over the sky. The measurements define an aperture distribution.

The strength of a radiator can be represented

by its brightness $B(\hat{\sigma},\nu)$, defined as the received power per unit area per unit frequency from a unit solid angle of the sky, or flux density per square radian. The response of an interferometer to the radiator is

$$\beta(\vec{r},\tau) = \int B(\hat{\sigma},\nu)P(\hat{\sigma},\nu)f(\nu)e^{-j2\pi\nu/c \times (c\tau - \vec{r}\cdot\hat{\sigma})}d\hat{\sigma}d\nu \qquad (1\text{-}3)$$

where $P(\hat{\sigma},\nu)$ is the primary beam pattern of an interferometer and $f(\nu)$ is the frequency response of the receiver. The vector $\vec{r}$ is the line joining two antennas and the vector $\hat{\sigma}$ points towards a point in the sky (Figure 1-3). The quantity τ is the relative time between the signal arriving at the two antennas and c is the velocity of light. Separating the double integral, the equation becomes

$$\beta(\vec{r},\tau) = \int b(\vec{r},\nu)f(\nu)e^{-j2\pi\nu\tau}d\nu \qquad (1\text{-}4)$$

where

$$b(\vec{r},\nu) = \int B(\hat{\sigma},\nu)P(\hat{\sigma},\nu)e^{j2\pi\nu/c \times \vec{r}\cdot\hat{\sigma}}d\hat{\sigma} \qquad (1\text{-}5)$$

The baseline vector decomposes into its three components as

$$\vec{r} = r_x\hat{x} + r_y\hat{y} + r_z\hat{z} \qquad (1\text{-}6)$$

where $\hat{x}$, $\hat{y}$, and $\hat{z}$ are unit vectors along the respective axis. Its orientation can be specified by a declination δ_r and an hour angle h_r. The three components are

$$\begin{aligned} r_x &= r\cos(\delta_r)\sin(h_r - h_{\sigma_o}) \\ r_y &= r\cos(\delta_r)\cos(h_r - h_{\sigma_o}) \\ r_z &= r\sin(\delta_r) \end{aligned} \qquad (1\text{-}7)$$

Expanding the inner product, the phase term in (1-5) becomes

$$\psi = 2\pi\nu/c \times (lr_x + mr_y + nr_z) \qquad (1\text{-}8)$$

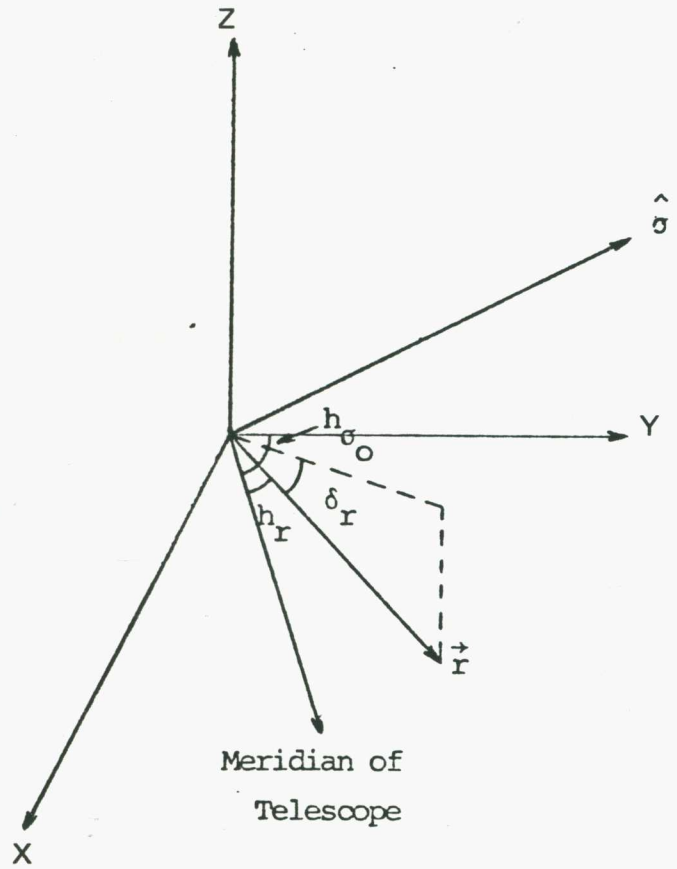

Figure 1-3 Baseline and Sky Vectors

A synthesis telescope is normally electrically steered to track a point in the sky. This point is taken to be the synthesis field center. The response of the telescope to radiation from this point is such that the phase of the measured quantity is zero. The phase of the response to the synthesis center as given by (1-8) is

$$\psi_{\sigma_o} = 2\pi\nu/c \times (m_{\sigma_o} r_y + n_{\sigma_o} r_z) \qquad (1\text{-}9)$$

Tracking will require this term to be cancelled, giving

$$\psi' = \psi - \psi_{\sigma_o} \qquad (1\text{-}10)$$

Defining a new set of variables,

$$\begin{aligned} l' &= l \\ m' &= m - m_{\sigma_o} \\ n' &= n - n_{\sigma_o} \end{aligned} \qquad (1\text{-}11)$$

the derotated phase takes on a form similar to (1-8),

$$\psi' = 2\pi\nu/c \times (l'r_x + m'r_y + n'r_z) \qquad (1\text{-}12)$$

The variables l', m', and n' are not independent, but are related through (1-1) and (1-11). Within each hemisphere, it suffices to know l' and m' to fix the sky coordinates. Projecting the hemisphere onto the lm plane, the aperture distribution at a particular frequency is

$$b'(r_x,r_y,\nu) = \iint \{B(l',m',\nu)P(l',m',\nu)e^{j2\pi\nu/c \times n'r_z/n}\} e^{j2\pi\nu/c \times (l'r_x + m'r_y)} dl'dm' \qquad (1\text{-}13)$$

The n' term can be made to disappear under approximation for a small region around the synthesis center. The exact relationships between the shifted sky coordinates and the equatorial coordinates are

$$l' = -\cos(\delta)\sin(\alpha - \alpha_{\sigma_o})$$
$$m' = \cos(\delta)\cos(\alpha - \alpha_{\sigma_o}) - \cos(\delta_{\sigma_o}) \qquad (1\text{-}14)$$
$$n' = \sin(\delta) - \sin(\delta_{\sigma_o})$$

Letting $\Delta\alpha = \alpha - \alpha_{\sigma_o}$ and $\Delta\delta = \delta - \delta_{\sigma_o}$, then in the neighborhood of the synthesis center, the sky coordinates (away from the equator) are approximated by

$$l' \simeq -\Delta\alpha\cos(\delta_{\sigma_o})$$
$$m' \simeq -\Delta\delta\sin(\delta_{\sigma_o}) \qquad (1\text{-}15)$$
$$n' \simeq \Delta\delta\cos(\delta_{\sigma_o})$$

However, it must be noted that for a fixed field around the synthesis center, the approximation deteriorates towards the two celestial poles. At the poles, the coordinates are more appropriately approximated by

$$l' \simeq -\Delta\delta_p\sin(\Delta\alpha)$$
$$m' \simeq -\Delta\delta_p\cos(\Delta\alpha) \qquad (1\text{-}16)$$
$$n' \simeq 0$$

where $\Delta\delta_p$ is the absolute offset in declination from the pole. The position in sky dimensions of a point in the field with respect to the center (away from the poles and equator) is

$$L \simeq l'$$
$$M \simeq m'/\sin(\delta_{\sigma_o}) \qquad (1\text{-}17)$$

From (1-15), it will be noted that

$$n' \simeq -m'\cot(\delta_{\sigma_o}) \qquad (1\text{-}18)$$

and the total phase becomes

$$\psi' \simeq 2\pi\nu/c \times (l'r_x + m'r_y') \qquad (1\text{-}19)$$

where $r_y' = r_y - r_z\cot(\delta_{\sigma_o})$. Equation (1-13) can now be seen as a Fourier relationship between $b'(r_x, r_y', \nu)$ and $B(l', m', \nu)P(l', m', \nu)/n$. The inversion is

$$B(l',m',\nu)P(l',m',\nu)/n \simeq (\nu/c)^2 \int\int b'(r_x,r'_y,\nu)e^{-j\psi'} dr_x dr'_y \qquad (1\text{-}20)$$

For line arrays which point towards a declination of zero, r_z vanishes and the brightness can be obtained exactly by a two-dimensional inversion of (1-13). This applies to an EW array. For line arrays which point to a non-zero declination, the brightness is approximated by the two-dimensional inversion (1-20). The equation is exact for radiation coming from the synthesis centre. When the radiation is away from the synthesis centre, errors are introduced through the approximation in sky coordinates. This applies to a NS array.

From here onwards the sky coordinates will be measured with respect to the synthesis center, and the prime's will be dropped.

1.5 Aperture Coverage

The aperture of a synthesis telescope is filled by measurements at a number of baselines. The length of the baseline is given by the number of wavelengths separating the two antennas. These can be expressed in terms of parameters on the Earth.

The orientation of an interferometer on the horizon can be specified by μ, the angle it subtends with the plane of the meridian circle, or the azimuth (Figure 1-5). For an interferometer at a latitude θ,

$$\begin{aligned} \delta_r &= \sin^{-1}\{\cos(\mu)\cos(\theta)\} \\ h_r &= -\sin^{-1}\{\sin(\mu)/\cos(\delta_r)\} \end{aligned} \qquad (1\text{-}22)$$

Armed with information about the baselines and the synthesis center, the aperture coverage can readily

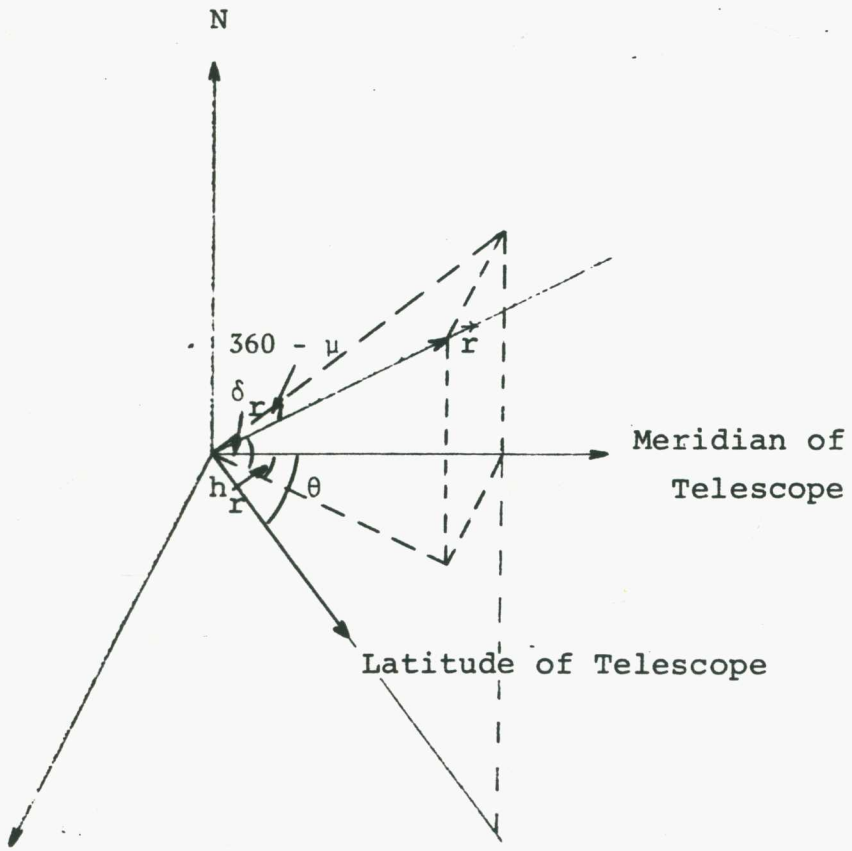

Figure 1-5 Orientation of an Interferometer

be determined. Examples can be found in Wellington (1968).

Each interferometer provides two baseline orientations, one directing from antenna 1 to antenna 2, and the other directing from antenna 2 to antenna 1. Thus for each measurement $b'(\vec{r},\nu)$, there is a corresponding measurement $b'(-\vec{r},\nu)$ given by

$$b'(-\vec{r},\nu) = \int\int B(l,m,\nu)P(l,m,\nu)e^{-j\psi}dldm/\sin(\delta) \qquad (1\text{-}23)$$

When the weighted brightness distribution is real, the aperture distribution is Hermitian,

$$b'(-\vec{r},\nu) = b'^{*}(\vec{r},\nu) \qquad (1\text{-}24)$$

where the superscript * denotes a complex conjugate. It is thus only necessary to physically cover half the aperture surface, the other half is obtained by conjugating the measurements. In any case, it is physically impossible to have a 360 degree coverage in hour angle for most region of the sky. Under this condition, the inversion is given by twice the real part of (1-20).

1.6 Beam Pattern of a Synthesis Telescope

The true brightness distribution can be recovered only if all its spatial frequency components are measured. A synthesis telescope can only measure a subset of these. This subset is given by $g(r_x,r'_y)b'(r_x,r'_y,\nu)$ where $g(r_x,r'_y)$ is the measurement window. The result is a convolution in the sky domain as follows,

$$S(l,m,\nu) = \int\int B(l',m',\nu)P(l',m',\nu)G(l-l',m-m',\nu)\,dl'dm'/\sin(\delta) \qquad (1\text{-}25)$$

where $S(l,m,\nu)$ is the flux density per synthesised beam and

$G(l,m,\nu)$ is the Fourier transform of $g(r_x,r'_y)$. The synthesised beam, $P_s(l,m,\nu)$, is defined as $G(-l,-m,\nu)$,

$$P_s(l,m,\nu) \simeq 2(\nu/c)^2 Re\{\int\int g(r_x,r'_y)e^{j2\pi\nu/c \times (lr_x + mr'_y)} dr_x dr'_y\} \quad (1\text{-}26)$$

It appears to be position invariant under the approximation. However, in the exact formulation, it can be seen that this is true only if r_z is zero.

In view of the configuration of the FST, two cases will be considered. They are those of synthesis via the rotation of the Earth by an EW array and by a NS array. These are special cases of the general collinear arrays which synthesise a conical surface. To simplify analysis, $g(r_x,r'_y)$ will be assumed to be unity over the measurement window. Before proceding further, it will be noted that the differential element in the inversion is

$$dr_x dr'_y = dr_x\{dr_y - \cot(\delta_{\sigma_o})dr_z\} \quad (1\text{-}27)$$

or, in terms of $drdh_{\sigma_o}$,

$$dr_x dr'_y = r\cos(\delta_r)\{\cos(\delta_r) - \cot(\delta_{\sigma_o})\sin(\delta_r)\cos(h_r - h_{\sigma_o})\} drdh_{\sigma_o} \quad (1\text{-}28)$$

For interferometers lying in an EW direction, μ can be taken to be -90^o, giving an h_r of 90^o and a δ_r of 0^o. The Z component of the baseline vanishes and the cone degenerates to a circle. The differential element becomes $rdrdh_{\sigma_o}$ and the synthesised beam is exact,

$$P_{sW}(l,m,\nu) = 2(\nu/c)^2\int\int\cos\{2\pi\nu/c \times r(l\cos(h_{\sigma_o}) + m\sin(h_{\sigma_o}))\} rdrdh_{\sigma_o} \quad (1\text{-}29)$$

To facilitate further evaluation, the following parameters

are defined,

$$l = \rho\cos(\phi)$$
$$m = \rho\sin(\phi) \qquad (1\text{-}30)$$

and

$$P_{sW}(\rho,\phi,\nu) = 2(\nu/c)^2 \int\int \cos\{2\pi\nu/c \times r\rho\cos(\phi - h_{\sigma_o})\} r\,dr\,dh_{\sigma_o} \qquad (1\text{-}31)$$

For an hour angle coverage of 180°, the double integral can be performed in closed form. Integration in hour angle gives

$$P_{sW}(\rho,\phi,\nu) = 2(\nu/c)^2 \int_{r_1}^{r_2} J_o(2\pi\nu/c \times r\rho)\,r\,dr \qquad (1\text{-}32)$$

where r_1 and r_2 are the lengths of the minimum and the maximum available baseline respectively. This is in the form of an Hankel transform and results in

$$P_{sW}(\rho,\phi,\nu) = \pi(\nu/c)^2\{[2J_1(2\pi\nu/c \times r_2\rho)/(2\pi\nu/c \times r_2\rho)]r_2^2 - [2J_1(2\pi\nu/c \times r_1\rho)/(2\pi\nu/c \times r_1\rho)]r_1^2\} \qquad (1\text{-}33)$$

The square bracketed terms in (1-33) are of the form $2J_1(\upsilon)/\upsilon$ which drops to half its maximum value at $|\upsilon| \simeq 2.2$. For the case where r_1 is zero, the half power widths of the beam at $m = 0$ and $l = 0$ are respectively

$$L_W \simeq 2.2/(\pi\nu/c \times r_2)$$
$$M_W \simeq 2.2/\{\pi\nu/c \times r_2\sin(\delta_{\sigma_o})\} \qquad (1\text{-}34)$$

For interferometers lying in a NS direction, μ will be taken to be 180°. The declination is $-\sin^{-1}\{\cos(\theta)\}$. However, the hour angle is two valued, 0° and 180° for the northern and southern hemispheres respectively. The Z component of the baseline is non zero and a conical surface is described as the Earth rotates. For the

array in either hemisphere,

$$r_{xS} = -r\sin(\theta)\sin(h_{\sigma_o})$$
$$r_{yS} = r\sin(\theta)\cos(h_{\sigma_o}) \qquad (1\text{-}35)$$
$$r_{zS} = -r\cos(\theta)$$

The differential element is

$$dr_x dr'_y = r\sin^2(\theta)drdh_{\sigma_o} + r\cot(\delta_{\sigma_o})\sin(\theta)\cos(\theta)\cos(h_{\sigma_o})$$
$$drdh_{\sigma_o} \qquad (1\text{-}36)$$

Inversion in hour angle is rather complicated. However, useful information about the beam pattern can be obtained at individual hour angles. Inversion in r gives

$$P_{sS}(l,m,\nu) \simeq (\nu/c)^2 \int\{r_2 F(\nu/c \times r_2\eta) - r_1 F(\nu/c \times r_1\eta)$$
$$\xi dh_{\sigma_o} \qquad (1\text{-}37)$$

where $\eta = 2\pi\{-l\sin(\theta)\sin(h_{\sigma_o}) + m[\sin(\theta)\cos(h_{\sigma_o}) + \cos(\theta)\cot(\delta_{\sigma_o})]\}$

$$\xi = \sin^2(\theta) + \cot(\delta_{\sigma_o})\sin(\theta)\cos(\theta)\cos(h_{\sigma_o})$$

and $F(\upsilon) = 2\{[\cos(\upsilon) - 1]/\upsilon + \sin(\upsilon)/\upsilon\}$

The function $F(\upsilon)$ describes the normalised beam pattern at a particular hour angle when r_1 is zero. It drops to half its maximum value at $|\upsilon| \simeq 1.6$ (Figure 1-6). The half power widths at h_{σ_o} for $l = 0$ and $m = 0$ are respectively

$$L_S \simeq 1.6/\{\pi\nu/c \times r_2\sin(\theta)\sin(h_{\sigma_o})$$
$$M_S \simeq 1.6/\{\pi\nu/c \times r_2[\sin(\theta)\cos(h_{\sigma_o})\sin(\delta_{\sigma_o}) + \cos(\theta)\cos(\delta_{\sigma_o})]\} \qquad (1\text{-}38)$$

1.7 Beam Shaping

In telescopes with unfilled aperture, the beam pattern is the transform of sampled points on the measurement surface. The sampling is necessarily finite. The transformation results in grating ring

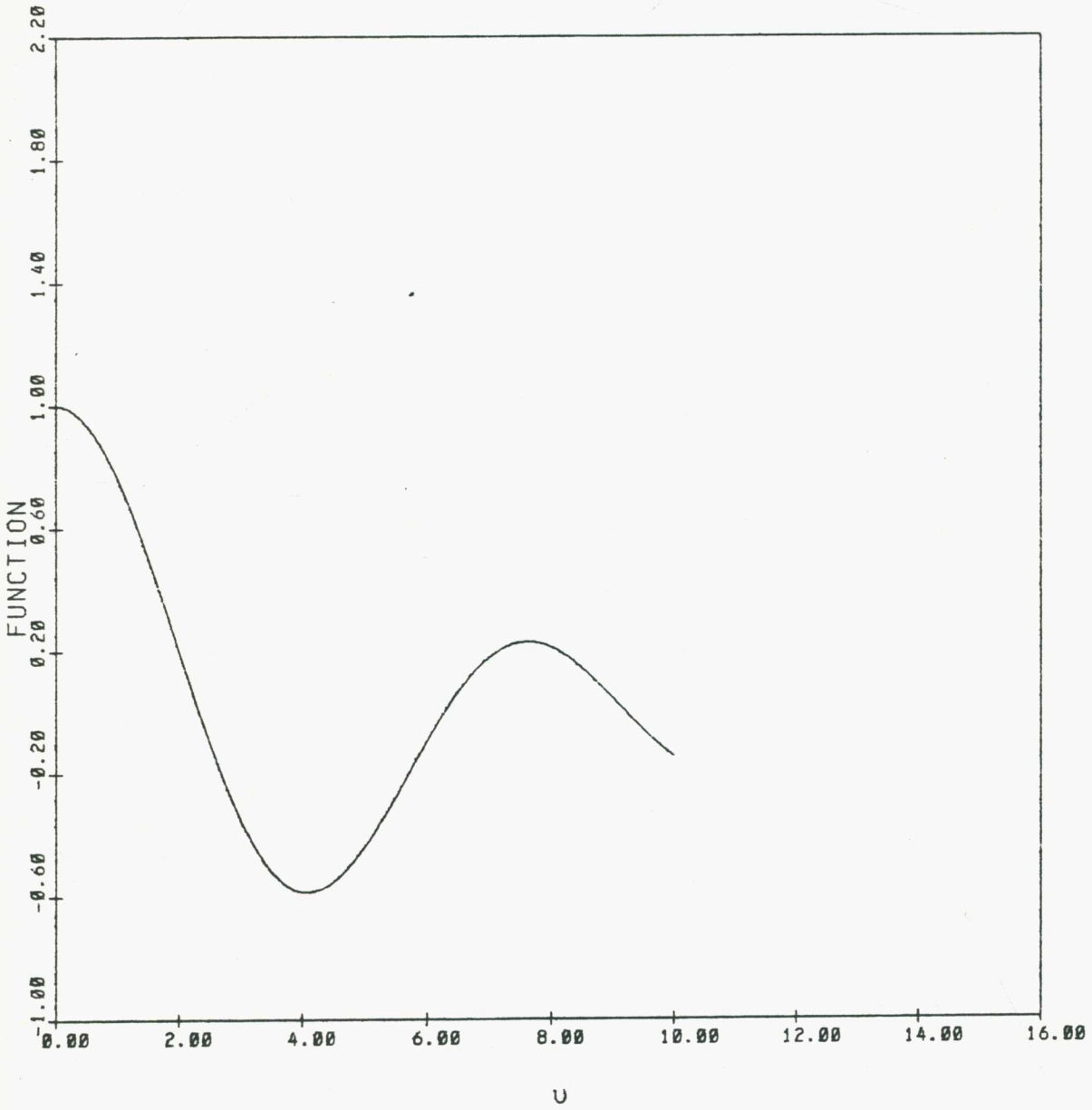

Figure 1-6 One Dimensional NS Beam Pattern

and sidelobe responses. Grating interference is a consequence of the discrete nature of sampling. It comes from radiation outside the region of interest. Sidelobe interference is due to the finite coverage of the measurement surface. This can be due to incomplete coverage in hour angle or baseline, and can be controlled by appropriately weighing the data. The simplest weighting that can be used is not to apply one, or natural weighting.

Each baseline vector samples a point on the measurement surface. The distance travelled by the tip of the baseline over a differential hour angle is

$$ds = \{r\{\cos^2(\delta_r) - \sin(\delta_r)\cos(\delta_r)\cot(\delta_{\sigma_o})\cos(h_r - h_{\sigma_o})\}/ \{\cos^2(\delta_r) - 2\cos(\delta_r)\sin(\delta_r)\cot(\delta_{\sigma_o})\cos(h_r - h_{\sigma_o}) + \cot^2(\delta_{\sigma_o})\sin^2(\delta_r)\}^{\frac{1}{2}}\}dh_{\sigma_o} \quad (1\text{-}39)$$

In Earth rotational synthesis, each measurement is performed over a finite hour angle, Δh_k, and covers an arc $s(r,\Delta h_k)$. The sampling density is

$$d(r,\Delta h_k) = 1/s(r,\Delta h_k) \quad (1\text{-}40)$$

When synthesis is performed by a collinear array, the density of measurement at short baselines is proportionally higher than the density of measurement at long baselines. If furthermore r_z is not zero, the density of measurement for each baseline varies with the hour angle. To obtain a uniform measurement density, an appropriate weighting can be applied. Further control of the beam pattern can be realised by superimposing on this an extra grading. The overall weighting becomes

$$W(r,\Delta h_k) \propto s(r,\Delta h_k)g(r,\Delta h_k) \quad (1\text{-}41)$$

Two useful gradings are the Gaussian and the linear. As examples, gradings which are not functions of hour angles will be investigated. The Gaussian grading has the form

$$g_G(r) = e^{(r/r_2)^2 \ln(q)} \qquad (1\text{-}42)$$

where q is the value of the grading at the maximum baseline r_2. The linear grading is

$$g_L(r) = 1 + r/r_2 \times (q - 1) \qquad (1\text{-}43)$$

This grading is normally set to zero when its value becomes negative. It provides a means of screening out long baselines when producing maps with a lower angular resolution.

Two FST beams have been generated using respectively the natural weighting and the baseline proportional Gaussian weighting (Figure 1-7). The maximum spacing is 32 and the hour angle coverage is 8 hours or 120°. The first gives a low extended response with small negative sidelobes. The second gives a better beam definition with a high negative sidelobe level.

1.8 Brightness Temperature Scale

A telescope has a finite beamwidth and the measurement is a beam smoothed quantity, flux density per beam,

$$S(l,m,\nu) = \int\int B(l',m',\nu)P(l',m',\nu)P_s(l'-l,m'-m,\nu) \, dl'dm'/\sin(\delta) \qquad (1\text{-}44)$$

Distributing the brightness uniformly over the beam, an observed brightness distribution can be defined,

$$B_o(l,m,\nu) = S(l,m,\nu)/\{\int\int P(l',m',\nu)P_s(l'-l,m'-m,\nu) \, dl'dm'/\sin(\delta)\} \qquad (1\text{-}45)$$

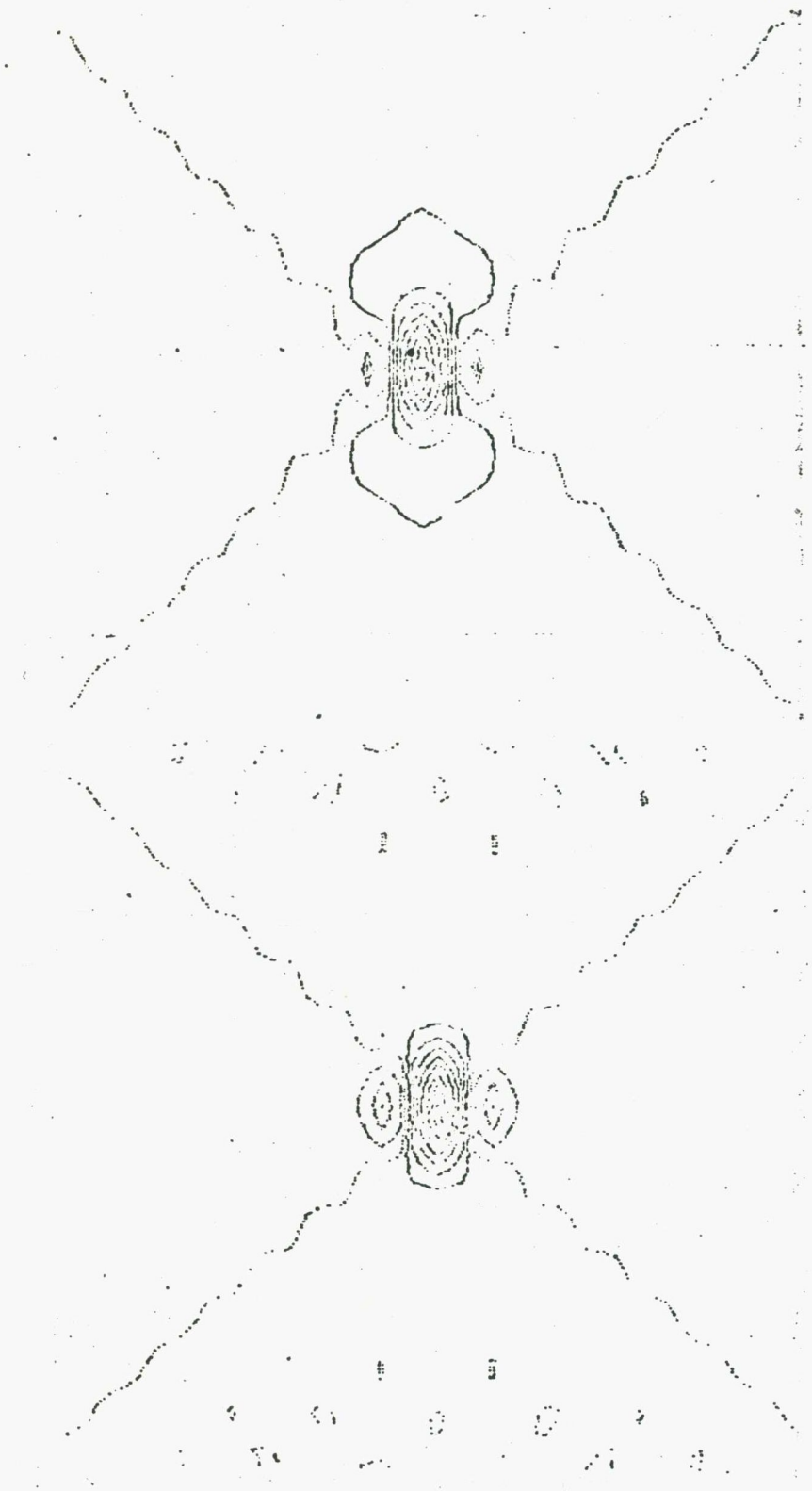

Natural
Weighting

Baseline
Proportional
Gaussian
Weighting

q = .25

Figure 1-7 FST Beam Patterns

The synthesised beam is concentrated over a small region of the sky over which $P(l',m',\nu)/\sin(\delta)$ can be assumed to be constant. The double integral is then over the synthesised beam only.

To relate the brightness to the absolute flux density scale, $S_a(l,m,\nu)$, normalised beam patterns $P_n(l,m,\nu)$ and $P_{sn}(l,m,\nu)$ have to be used. The Fourier relationship between the synthesised beam and the measurement window leads to

$$\int\int\{P_s(l,m,\nu)/P_s(0,0,\nu)\}dldm \times 2(\nu/c)^2 Re\{\int\int \{g(r_x,r'_y)/g(0,0)\}dr_x dr'_y\} = 1 \qquad (1\text{-}46)$$

The second term is the effective aperture area, A, or in terms of the physical quantity, $(\nu/c)^2 A_p$. The observed brightness can now be expressed as

$$B_o(l,m,\nu) = (\nu/c)^2 A_p \sin(\delta) S_a(l,m,\nu)/P_n(l,m,\nu) \qquad (1\text{-}47)$$

The brightness temperature is approximated by the Rayleigh Jean's Law,

$$T_{B_o}(l,m,\nu) = 1/(2k) \times A_p \sin(\delta) S_a(l,m,\nu)/P_n(l,m,\nu) \qquad (1\text{-}48)$$

where k is Boltzmann's constant. Note that the brightness temperature scale is independent of the frequency characteristics of the array. It does, however, depend on the frequency characteristics of each individual antenna. More significantly, it exhibits a $\sin(\delta)$ dependence over the sky. This is the factor which projects the xy plane towards the field of interest.

To fix the brightness temperature scale, it is necessary to evaluate A_p. This will be evaluated for

cases applicable to the FST. The elemental aperture area is given by (1-27). In the EW case, the aperture is described by $rdrdh_{\sigma_o}$. For a coverage of Δh in hour angle, the aperture area is

$$A_{pW} = 2\Delta h Re\{\int g(r)rdr\} \qquad (1\text{-}49)$$

For the three cases of uniform, Gaussian, and linear gradings, the integral gives respectively

$$\begin{aligned} I_U &= (r_2^2 - r_1^2)/2 \\ I_G &= r_2^2\{q - e^{(r_1/r_2)^2 \ln(q)}\}/\{2\ln(q)\} \\ I_L &= (r_2 - r_1)\{(r_2 + r_1)/2 + (q - 1)(r_2^2 + r_2 r_1 + r_1^2)/(3r_2)\} \end{aligned} \qquad (1\text{-}50)$$

In the NS case, the aperture is described by (1-36). The aperture area is

$$\begin{aligned} A_{pS} = 2\{&\Delta h \sin^2(\theta) + 2\cot(\delta_{\sigma_o})\sin(\theta)\cos(\theta) \\ &\cos\{(h_{\sigma_{of}} + h_{\sigma_{oi}})/2\}\sin(\Delta h/2)\}I \end{aligned} \qquad (1\text{-}51)$$

where Δh ranges from $h_{\sigma_{oi}}$ to $h_{\sigma_{of}}$ and I is one of (1-50). The brightness temperature scale in the direction of the synthesis center is plotted in Figure 1-8.

1.9 Sensitivity

The sensitivity of a radio telescope is determined by its inherent noisiness. This is quantified by the root mean square (rms) value of the noise in the data. A signal is deemed detectable when an output signal to noise ratio (S/N) better than unity is achieved. In terms of flux density, the minimum detectable quantity is

$$S_{min} = 2kMT_s/\{A_e(\Delta\nu_r t)^{\frac{1}{2}}\} \qquad (1\text{-}52)$$

where M is the detection inefficiency factor, T_s is the system noise temperature, A_e is the effective collecting area of the antenna, $\Delta\nu_r$ is the receiver bandwidth,

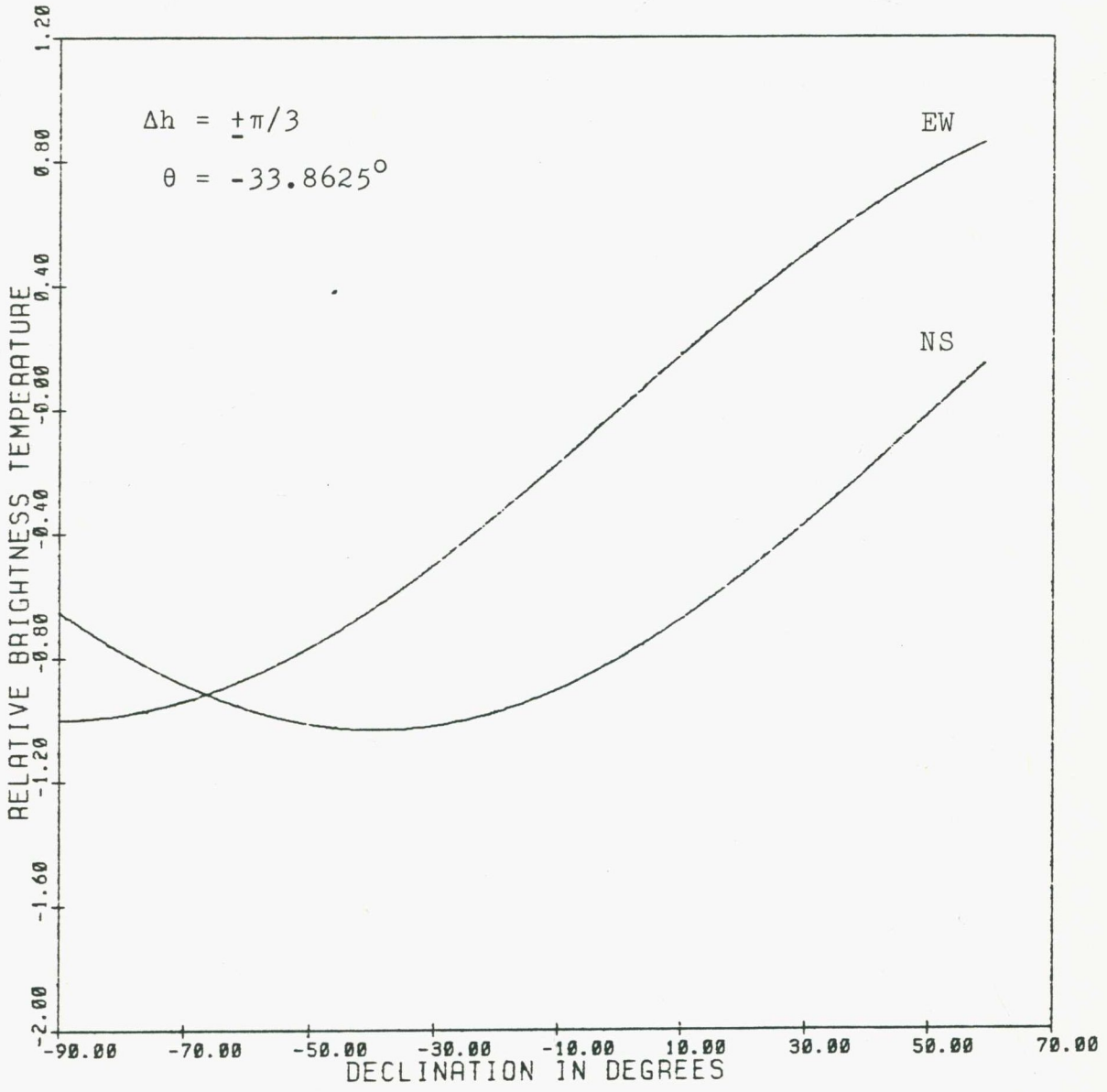

Figure 1-8 Variation of the Brightness Temperature Scale in Declination

and t is the sample integration time. A synthesis telescope is built from pairs of correlating interferometers. For such interferometers the system noise temperature and the effective collecting area are

$$T_s = (T_{s1}T_{s2})^{\frac{1}{2}}$$
$$A_e = 2(A_{e1}A_{e2})^{\frac{1}{2}} \qquad (1\text{-}53)$$

where 1 and 2 denote the component antennas of each interferometer. Given the nature of signal and noise, the minimum detectable flux density for a synthesis telescope is

$$S_{min} = 2kMT_s/\{A_e(\Delta\nu_r t)^{\frac{1}{2}}\} \times (\Sigma W_i)^{\frac{1}{2}}/\Sigma W_i \qquad (1\text{-}54)$$

where W_i is the weight which is applied to the ith spacing. The relative effect of some common weights on sensitivity can be found in O'Sullivan (1974).

The minimum detectable signal can also be expressed in terms of a brightness temperature,

$$T_{Bmin} \propto A_p \sin(\delta)/(2k) \times S_{min} \qquad (1\text{-}55)$$

From (1-49) to (1-51), A_p can be seen to be roughly proportional to the maximum baseline available. For the FST, the maximum baseline is given by $(N + \frac{1}{2})d$, with N being the highest spacing used. Maximum sensitivity is achieved with natural weighting,

$$T_{Bmin} \propto (N + \tfrac{1}{2})^2/(N\Delta\nu_r t)^{\frac{1}{2}} \qquad (1\text{-}56)$$

For a fixed t, the sensitivity to an extended region of radiation depends upon N, which determines the angular resolution, and upon $\Delta\nu_r$, which determines the frequency resolution (Figure 1-9).

1.10 Data Sampling Requirement

In aperture synthesis, a sample in the measurement

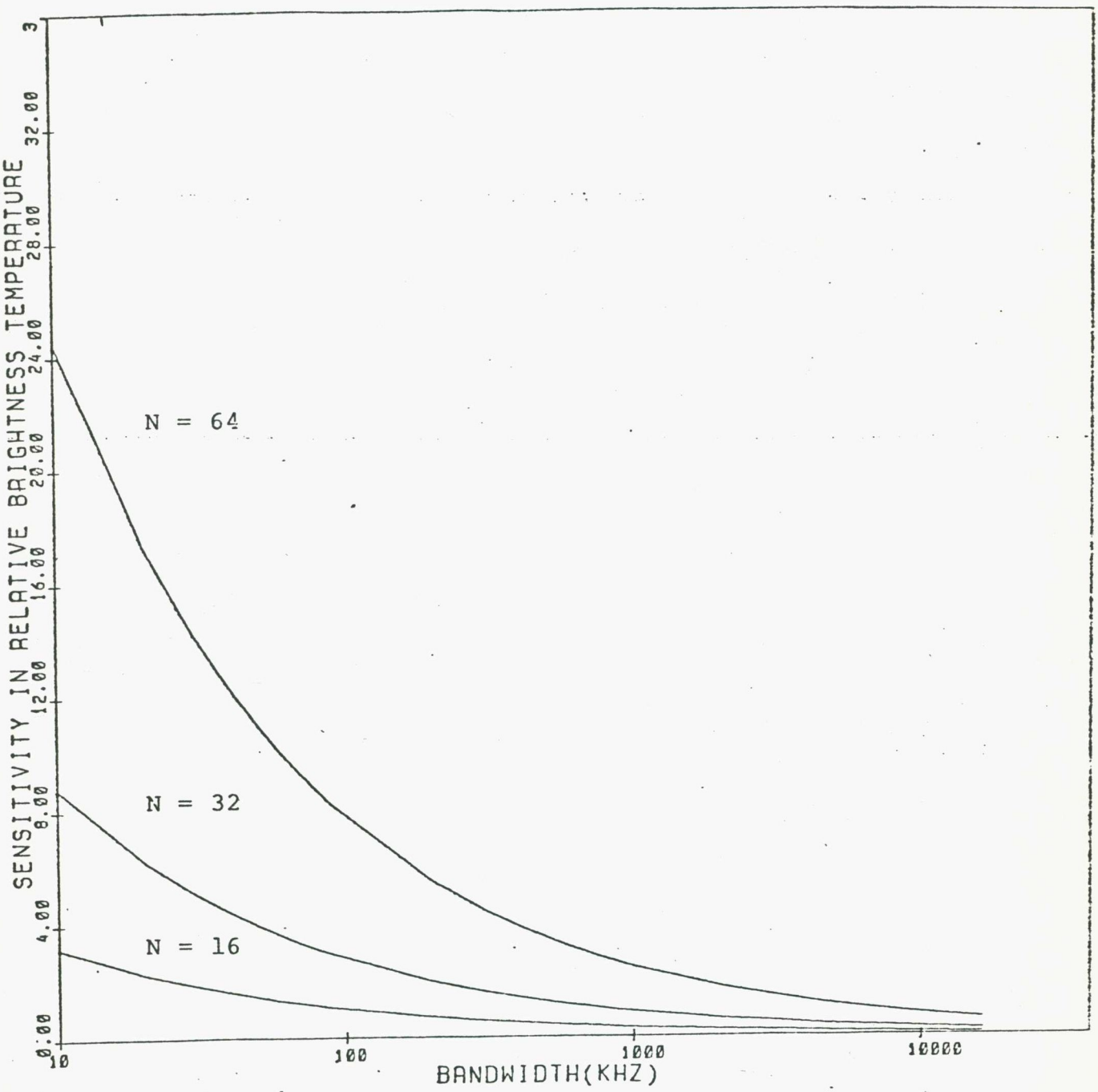

Figure 1-9 Effect of Bandwidth and Spacing Number on Sensitivity

plane is obtained by integrating the received signal over a period of time. Sampling theorem states that if there is to be no loss in information, the frequency of measurement must be at least twice the maximum rate of data variation. It will be assumed that the radiation being measured is constant over the period of synthesis. In this case, the measured data only exhibit a phase variation,

$$d\psi/dh_{\sigma_o} = 2\pi\nu/c \times (ldr_x/dh_{\sigma_o} + mdr_y/dh_{\sigma_o} + ndr_z/dh_{\sigma_o}) \quad (1\text{-}57)$$

with

$$\begin{aligned} dr_x/dh_{\sigma_o} &= -r\cos(\delta_r)\cos(h_r - h_{\sigma_o}) \\ dr_y/dh_{\sigma_o} &= r\cos(\delta_r)\sin(h_r - h_{\sigma_o}) \\ dr_z/dh_{\sigma_o} &= 0 \end{aligned} \quad (1\text{-}58)$$

The maximum rate of the phase variation occurs at an hour angle

$$h_{\sigma_{omax}} = h_r + \tan^{-1}(m/l) \quad (1\text{-}59)$$

and

$$(d\psi/dh_{\sigma_o})_{max} = 2\pi\nu/c \times r\cos(\delta_r)(l^2 + m^2)^{\frac{1}{2}} \quad (1\text{-}60)$$

This peaks for the maximum baseline of an EW array, and

$$(d\psi/dh_{\sigma_o})_{max,p} \simeq 2\pi\nu/c \times r_2\rho \quad (1\text{-}61)$$

Information about any radiation field within ρ can be fully recovered when the measurements are taken at twice the rate as specified in (1-61). The maximum integration time that can be tolerated per measurement is thus

$$t_{max} \simeq 1/(2\nu/c \times r_2\rho\Omega) \quad (1\text{-}62)$$

where Ω is the sidereal rate of rotation of the Earth.

The FST operates with an integration time of one minute per measurement. Given a field of 1.2 degrees, this is tolerable for over 180 spacings (Figure 1-10). With the present 64 spacings, it is permissible to time multiplex the receiver between the EW and NS arrays to synthesise the complete aperture within one observation.

1.11 References

Batchelor, R., D. L. Jauncey, K. J. Johnston, V. A. Efanov, L. R. Kogan, V. I. Kostenko, L. I. Matveenko, I. G. Moiseev, S. H. Knowles, A. Kh. Papatsenko, R. Preston, J. Spenser, A. N. Timofeev, N. F. Fourikis, and R. W. Schnilizzi. "First Global Radio Telescope", Pis'ma Astron. Zh., vol. 2, 467-473, 1976.

Belitzky, B. "New Giant Radio Telescope", Nature, vol. 262, 535-536, 1976.

Jansky, K. G. "Electrical Disturbances Apparently of Extraterrestrial Origin", Proc. IRE, vol. 21, 1387-1398, 1933.

LaLonde, L. M. "The Upgraded Arecibo Observatory", Science, vol. 186, 213-218, 1974.

Ryle, M. "Radio Telescopes of Large Resolving Power", Rev. Modern Phys., vol. 47, 557-566, 1975.

Wellington, K. "A 40 Sec of Arc Radio Telescope". Ph. D. Thesis, The University of Sydney, 1968.

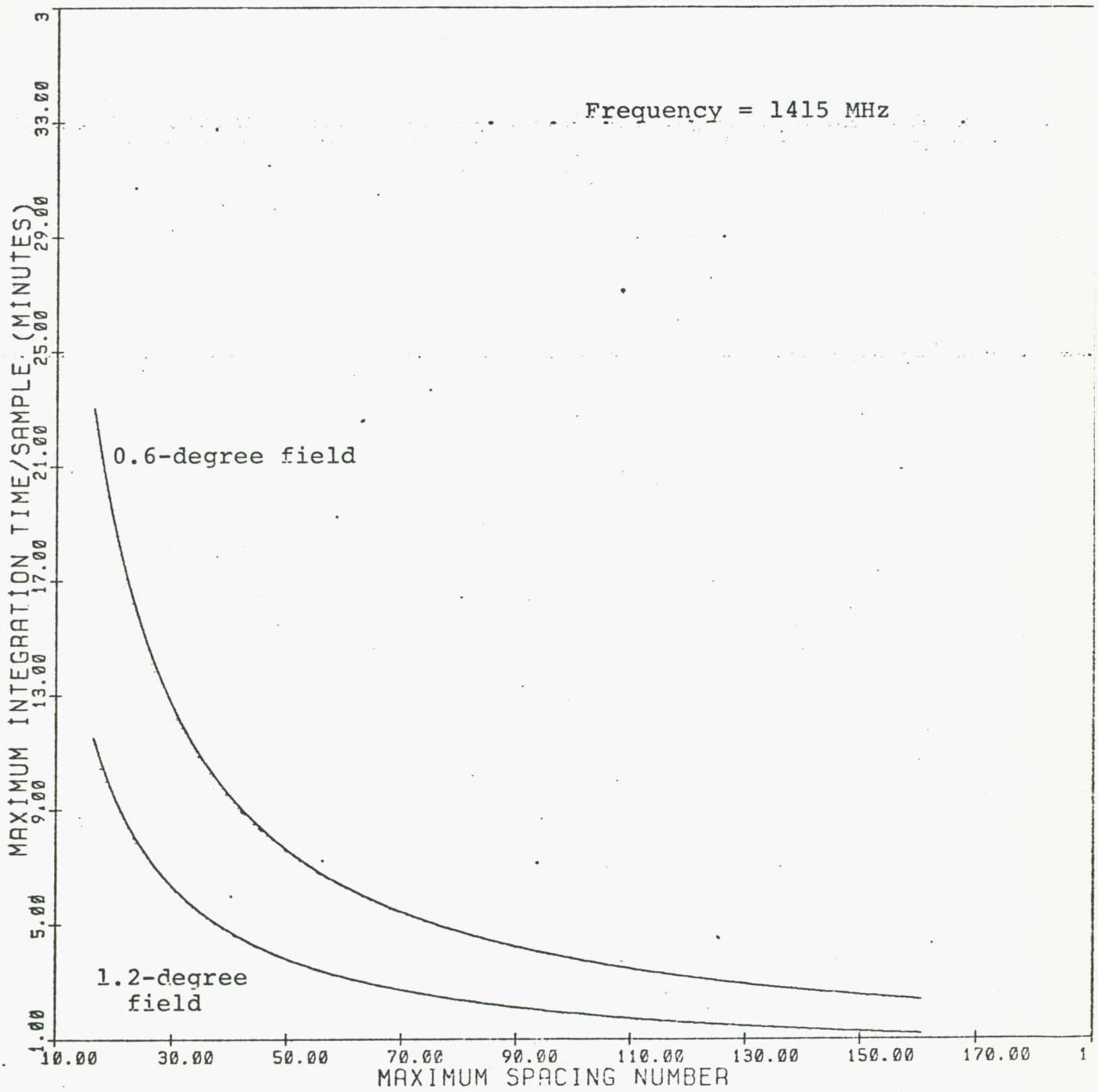

Figure 1-10 Limit on Integration Time

CHAPTER II A SPECTRAL LINE RECEIVER

2.1 Measurement of the Frequency Spectrum

In chapter I, the theory of aperture synthesis has been discussed in terms of the relationship between the aperture distribution and the brightness distribution with the qualification that the radiation is monochromatic. In practice, the radiation will be polychromatic and the receiver will have a finite bandwidth. The measured quantity is given by (1-4) which is a Fourier relationship between $\beta(\vec{r},\tau)$ and $b(\vec{r},\nu)$. The inversion is

$$b(\vec{r},\nu)f(\nu) = \int \beta(\vec{r},\tau)e^{j2\pi\nu\tau}d\tau \qquad (2\text{-}1)$$

It will be realised that $\beta(\vec{r},\tau)$ is the correlation function of the received radiation. In practice, τ is finite and discrete, resulting in

$$b(\vec{r},\nu)f(\nu) * c(\nu) = \int \chi(\tau)\beta(\vec{r},\tau)e^{j2\pi\nu\tau}d\tau \qquad (2\text{-}2)$$

where * denotes convolution. The sampling function, $\chi(\tau)$, and $c(\nu)$ is a Fourier transform pair and

$$\int\{\chi(\tau)/\chi(0)\}d\tau \times \int\{c(\nu)/c(0)\}d\nu = 1 \qquad (2\text{-}3)$$

The first term is the equivalent correlation width and the second term is the corresponding equivalent bandwidth. When the bandwidth of $f(\nu)$ is greater than $c(\nu)$, the former then determines the total bandwidth of interest and the latter determines how fine the structures within the bandwidth can be resolved. This method of spectral estimate is based on the measurement of the correlation function.

When τ is zero, the measured quantity becomes

$$\beta(\vec{r},0) = \int b(\vec{r},\nu)f(\nu)d\nu \qquad (2\text{-}4)$$

which is the total irradiation received. The frequency

resolution is now determined by $f(\nu)$. Measurements obtained with $f(\nu)$ centered at different frequencies then determine the total bandwidth. This method of spectral estimate is employed in the design of the Fleurs spectral line receiver.

2.2 Polychromatic Aperture Synthesis

The fact that the received radiation is over a finite bandwidth modifies the determination of the brightness distribution. Given that $f(\nu)$ is Hermitian, the total irradiation measured can be expressed as

$$\beta(\vec{r},0) = 2\int\int B(\hat{o},\nu')P(\hat{o},\nu')f(\nu')e^{j2\pi\nu'/c \times \vec{r}\cdot\hat{o}} \cos(2\pi\nu_o/c \times \vec{r}\cdot\hat{o})d\nu' d\hat{o} \qquad (2\text{-}5)$$

where ν_o is the frequency of the bandcenter and ν' is the frequency deviation from it. When the bandwidth is narrow enough such that the exponential term involving ν' is approximately unity, the equation can be inverted,

$$2\int B(\hat{o},\nu')P(\hat{o},\nu')f(\nu')d\nu' \simeq (\nu_o/c)^2\int\beta(\vec{r},0) \cos(2\pi\nu_o/c \times \vec{r}\cdot\hat{o})d\vec{r} \qquad (2\text{-}6)$$

The bandwidth requirement can be determined for the case where the primary beam smoothed brightness has a constant spectrum over the receiver passband and

$$\beta(\vec{r},0) \simeq 2\int B(\hat{o},\nu_o)P(\hat{o},\nu_o)\cos(2\pi\nu_o/c \times \vec{r}\cdot\hat{o}) \{\int f(\nu')e^{j2\pi\nu'/c \times \vec{r}\cdot\hat{o}}d\nu'\}d\hat{o} \qquad (2\text{-}7)$$

Except for the curly bracketed term, called the bandwidth pattern, $P_b(\vec{r},\hat{o})$, this is of the same form as that of the monochromatic case. When the bandwidth pattern is much wider than the brightness distribution, it

can be taken out of the integral and (2-7) can be inverted.

Quantitative results will be obtained for a rectangular passband. This provides a guide to the nature of $P_b(\vec{r},\hat{\sigma})$. Let the passband be W Hz wide with unit gain, then the bandwidth pattern is

$$P_b(\vec{r},\hat{\sigma}) = W\sin(\pi W/c \times \vec{r}\cdot\hat{\sigma})/(\pi W/c \times \vec{r}\cdot\hat{\sigma}) \quad (2\text{-}8)$$

It is plotted as a function of σ for various values of $W/c \times r$ (Figure 2-1). It is important in the case of wide bandwidth and long baseline to point the telescope towards the smallest expected radiation structure. When the structures are distributed away from the synthesis center, special attention should be placed on the selectivity of the receiver to enable proper retrieval of the brightness distribution.

2.3 Frequency Dependence of the Synthesised Beam

When the bandwidth pattern is wide, the synthesised beam can be approximated by its shape at the center frequency. In a spectral line receiver, the center frequencies of the different channels are different, and the corresponding synthesised beams are different. The Fourier relationship between the synthesised beam pattern and the aperture grading function can be expressed concisely as

$$P_s(\hat{\sigma},\nu) \leftrightarrow g(\nu/c \times \vec{r}) \quad (2\text{-}9)$$

This is the pattern towards the synthesis center. Under the approximations (1-15), the pattern towards a point (l',m') in the sky can be obtained via the shifting property of the Fourier transform,

$$P_s(l-l',m-m',\nu) \leftrightarrow g\{\nu/c \times (r_x,r'_y)\}e^{j2\pi\nu/c \times (lr_x + mr'_y)} \quad (2\text{-}10)$$

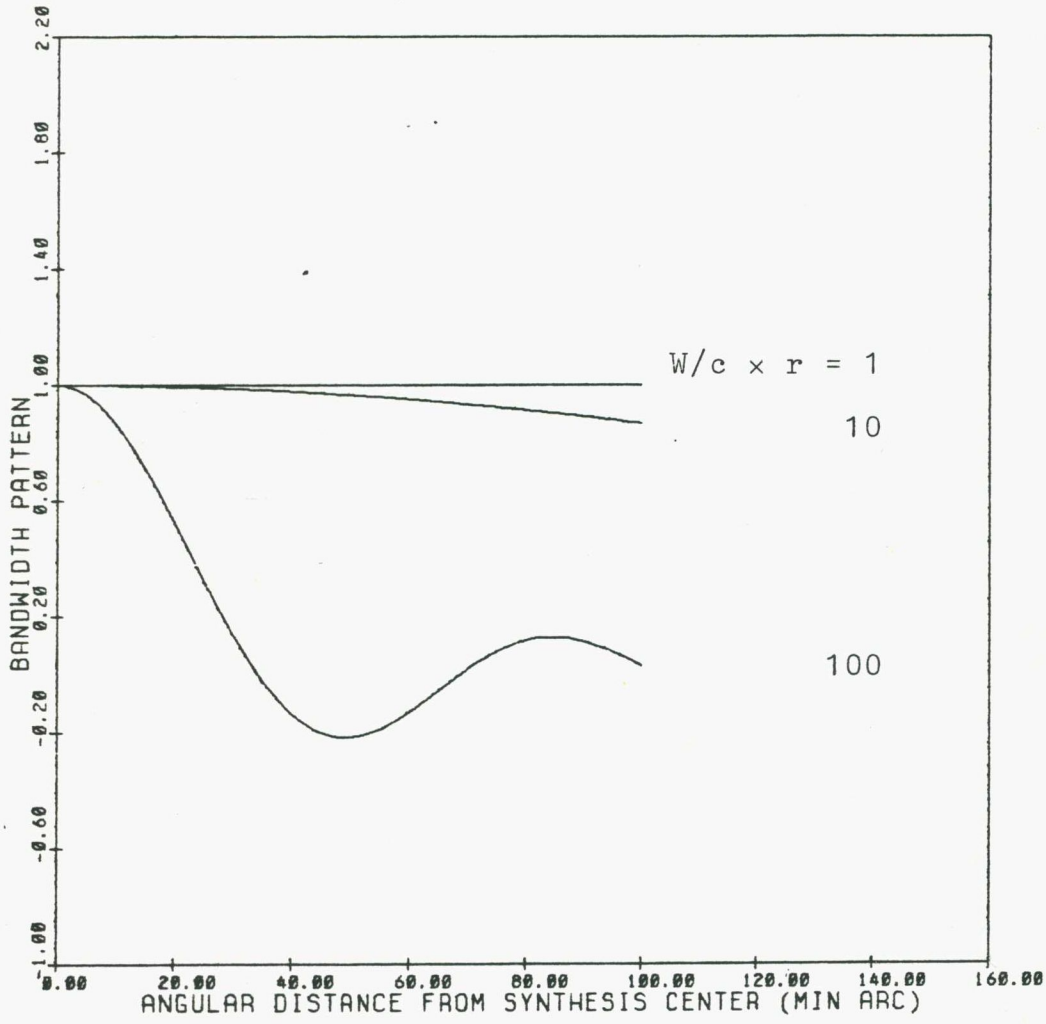

Figure 2-1 Bandwidth Pattern

The pattern at a different frequency, $a\nu$, is obtained via the scaling property,

$$P_s(l-l',m-m',a\nu) = P_s\{(l-l')/a,(m-m')/a,\nu\}/a^2 \qquad (2\text{-}11)$$

Three conclusions result from the equation. Firstly, the gain of the pattern is modified by $1/a^2$. Secondly, the linear beam dimension is modified by $1/a$. Thirdly, the shift in the sky position is modified by $1/a$. The relative gain and the relative dimensions of the different patterns are inveriant over the sky. The shift difference is a function of the distance from the synthesis center. The frequency dependencies are plotted with respect to a reference beam at 1420 MHz pointing towards the pole (Figure 2-2).

2.4 The Fleurs Spectral Line Receiver

The Fleurs spectral line receiver is configured around the existing 64 complex correlators of the FST. The existing instrument is described in Frater (1973). The line receiver provides two frequency channels for each of the 32 lowest spacings (Figure 2-3). When compared with the situation at full angular resolution, the scheme trades off roughly half the angular resolution for better sensitivity to extended radiation structures and shorter mapping time.

The line receiver was designed to keep the amount of additional hardware at a low level. The frequency selection is performed by two narrowband filters in the signal path of the large antenna. No such filters are provided for the small antennas. The number of filters required

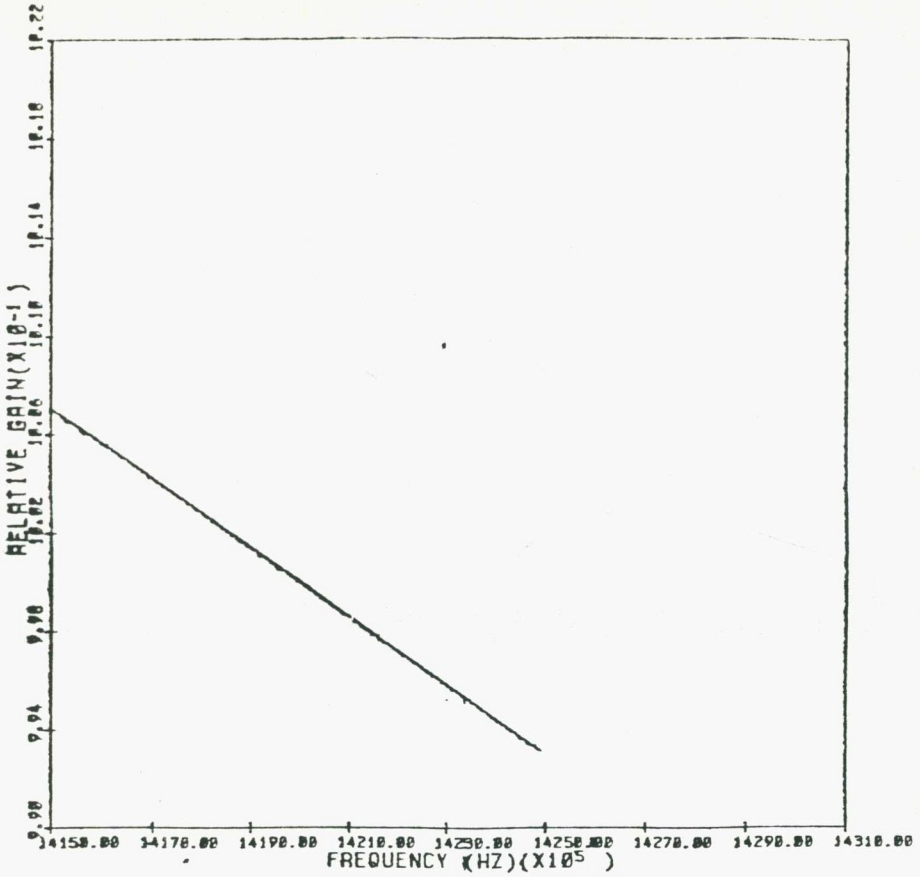

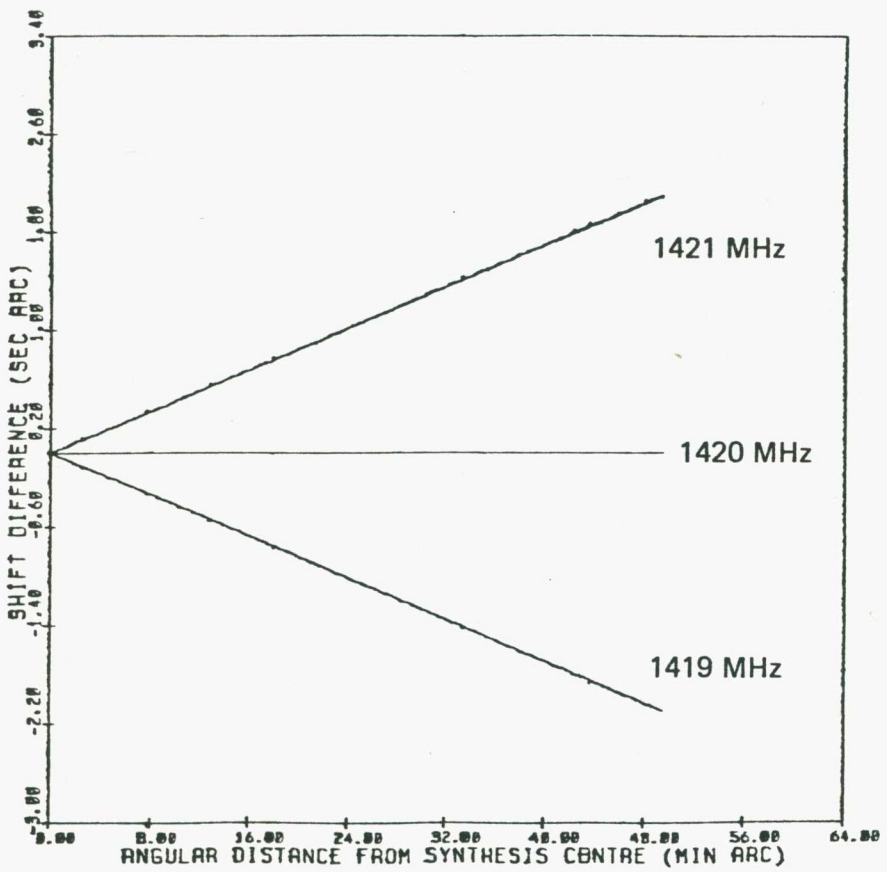

Figure 2-2 Frequency Dependence of Beam Parameters

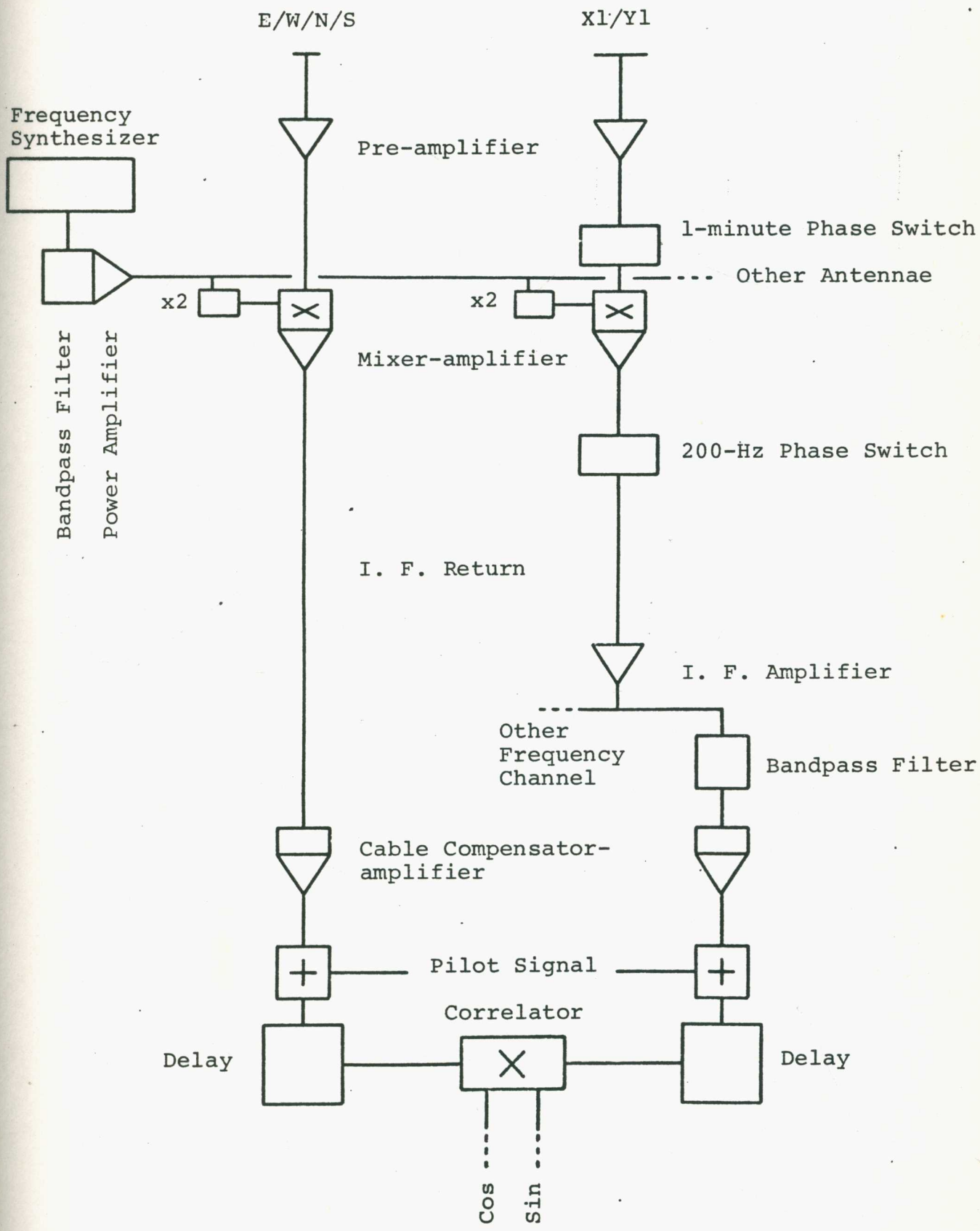

Figure 2-3 Fleurs Spectral Line Receiver

is thus 2 instead of 66. The tradeoff is a loss in sensitivity. An amplifier precedes the filters to fully utilise the dynamic range of the original receiver.

The FST uses a pilot signal in the intermediate frequency (IF) stage to perform the task of phase tracking. This signal must not be discriminated by the filters. The filters have to be placed before the insertion of the pilot. The two frequency channels feed respectively the original X1/Y1 correlators and the modified X2/Y2 correlators.

The X2/Y2 correlators are normally assigned to the higher 32 spacings of the telescope. To assign them to the lowest 32 spacings, the associated phase and delay tracking need to be modified. The phase tracking is made the same as that for X1/Y1 by stopping the X2/Y2 phase rotators. The modification in the delay tracking is a bit more involved. The EW array has the two large antennas located on opposite ends while the NS array has the two large antennas located on the same end. It is first necessary to simulate an antenna at the same end as X1. This is achieved by configuring the bulk delays of the small antennas in the NS mode. A similar situation now exists for both arrays. To bring X2/Y2 to the same position as X1/Y1, its 32 unit bulk delay is switched in and the extra delay is switched out (Figure 2-4). Driving the X2/Y2 delay ladder in unison with the X1/Y1 delay ladder then provides the extra frequency channel for the lowest 32 spacings. The modifications in phase and delay tracking are activated via an online

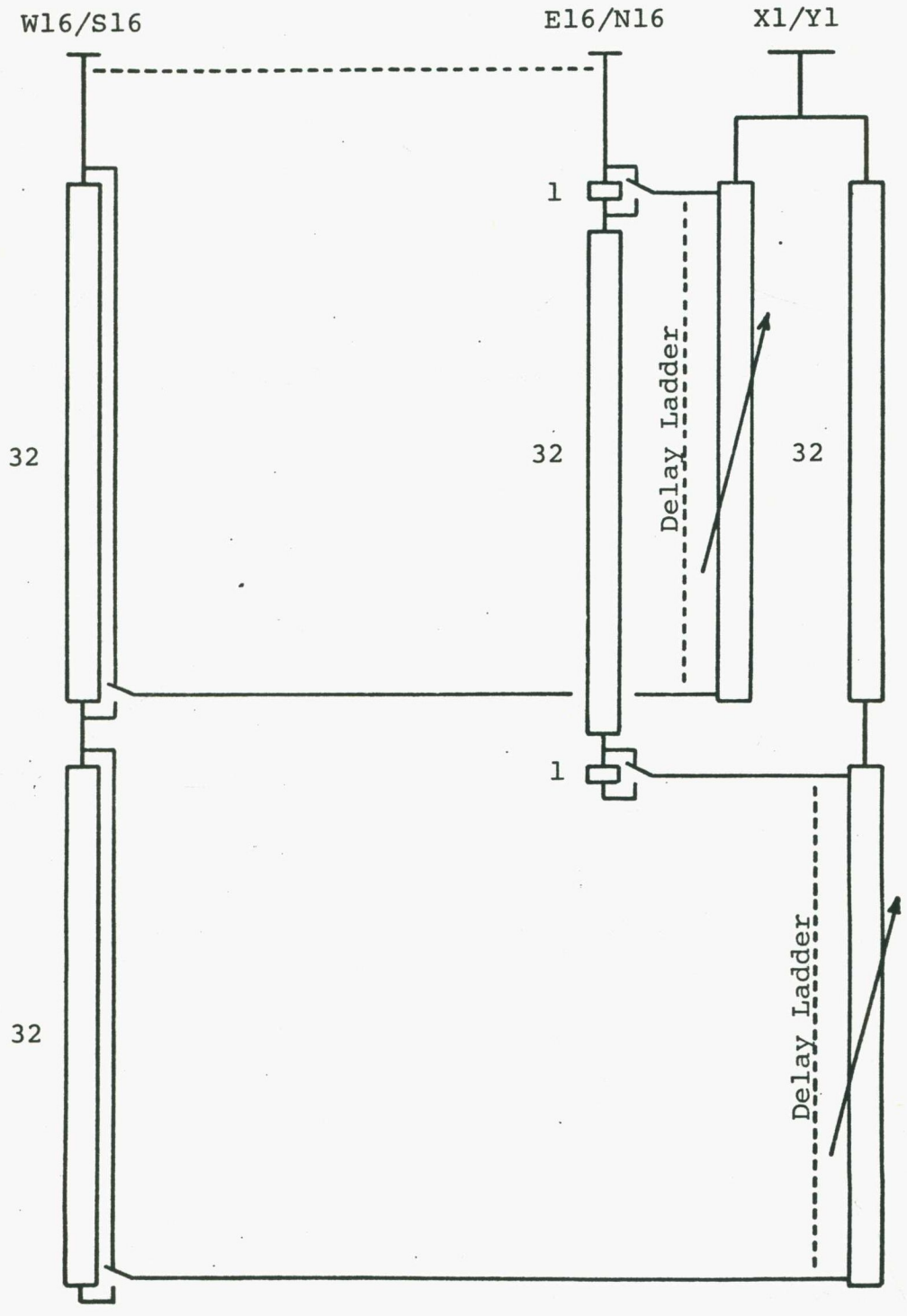

Figure 2-4 Delay Configuration

minicomputer.

Radiation lines have their characteristic frequencies. Nonzero relative velocity between the source of radiation and the observatory will cause the frequencies to be doppler shifted. It is necessary for the receiver to be able to accomodate these shifts. This is achieved by using a tunable local oscillator (LO). The usable frequency range of the FST is from 1410 MHz to 1425 MHz. The 21 cm neutral hydrogen line lies within this band and the receiver is designed to study its characteristics in external galaxies.

2.5 The Correlator

A correlator multiplies two signals together and average the output to separate the information from the noise (Figure 2-5). The completeness of the separation depends on the averaging process. In general the output contains an average term superimposed on a fluctuating term,

$$o(t) = o_s + o_n(t) \tag{2-12}$$

with a mean square value

$$E\{o^2(t)\} = o_s^2 + E\{o_n^2(t)\} \tag{2-13}$$

In terms of system parameters, this can be written as

$$E\{o^2(t)\} = \int\int h_3(t_1)h_3(t_2)R_z(t_1-t_2)dt_1dt_2 \tag{2-14}$$

where R is the correlation function of the parameter denoted by its subscript. When z(t) has an average value, its autocorrelation function is

$$R_z(\tau) = \{E\{z(t)\}\}^2 + R_z'(\tau) \tag{2-15}$$

The mean output is then

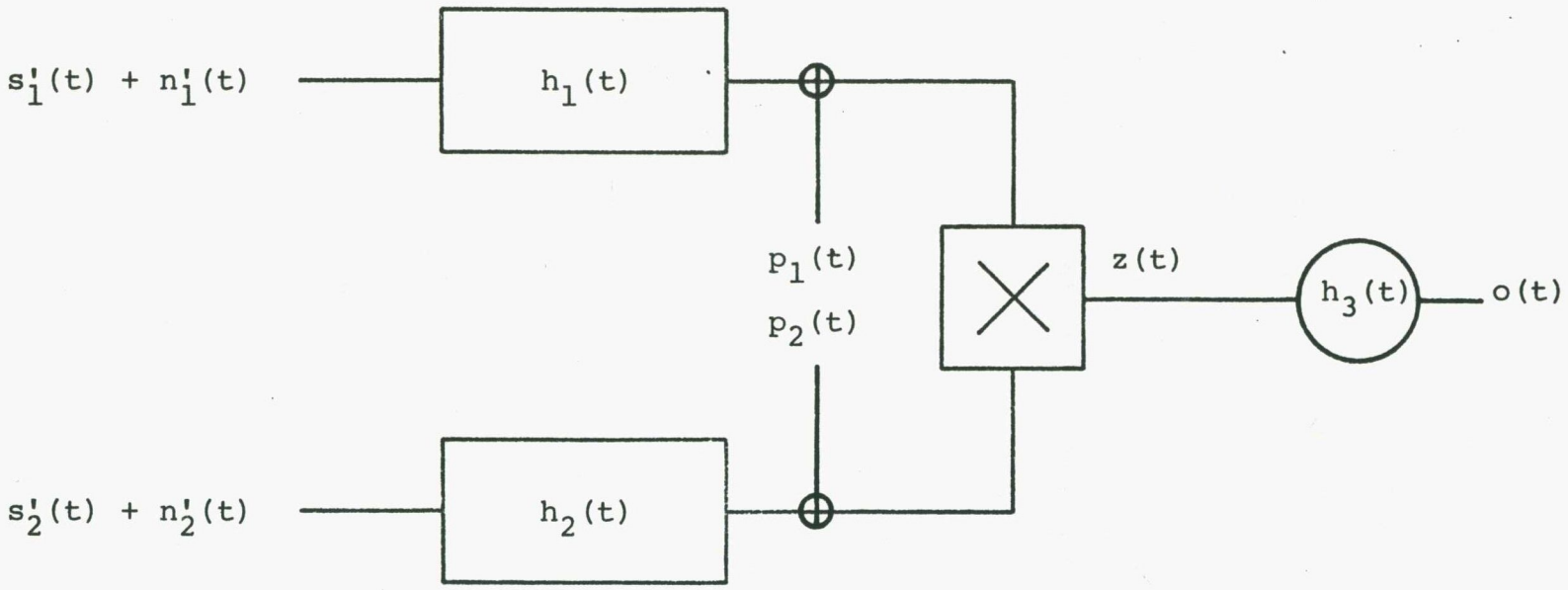

Figure 2-5 Fleurs Correlator

$$o_s = K\{E\{z(t)\}\} \qquad (2\text{-}16)$$

K being a system constant, and the variance of the output is

$$E\{o_n^2(t)\} = \int\int h_3(t_1)h_3(t_2)R_z'(t_1-t_2)dt_1dt_2 \qquad (2\text{-}17)$$

In the Fleurs receiver, each input to the correlator has three components. They are the information s(t), the noise n(t), and the pilot p(t). The first two exhibits independent, stationary normal distributions with zero mean. The last is a single frequency sinusoid. It is phase switched at 800 Hz in one of the two correlating inputs. The information content is then

$$E\{z(t)\} = \int\int h_1(t_1)h_2(t_2)R_{s'}(t_1-t_2)dt_1dt_2 \qquad (2\text{-}18)$$

and using Parseval's theorem,

$$o_s = K\int H_1(\nu)H_2^*(\nu)S_{s'}^*(\nu)d\nu \qquad (2\text{-}19)$$

where $H(\nu)$ and $S(\nu)$ are the respective system function and spectral density. The output noise is represented by its variance. In most radio astronomical work, the input S/N is much less than unity, and

$$R_z'(\tau) \simeq R_{n_1}(\tau)R_{n_2}(\tau) + R_{n_1}(\tau)R_{p_2}(\tau) + R_{p_1}(\tau)R_{n_2}(\tau) \qquad (2\text{-}20)$$

The mean square value of the output noise is then

$$E\{o_n^2(t)\} = \int |H_3(\nu)|^2 S_z'(\nu)d\nu \qquad (2\text{-}21)$$

with

$$S_z'(\nu) = S_{n_1}(\nu) * S_{n_2}(\nu) + S_{n_1}(\nu) * S_{p_2}(\nu) + S_{p_1}(\nu) * S_{n_2}(\nu) \qquad (2\text{-}22)$$

2.6 Frequency Response of the Fleurs Spectral Line Receiver

The Fleurs spectral line receiver is designed to study the large scale properties of external galaxies

using neutral hydrogen (HI) as a trace element. For galaxies with a linear dimension greater than 10' arc, the instrument provides a favorable galaxy size to beam size ratio (Bosma 1978). This enables a good determination of the HI distribution, the average velocity field, and the rotation curve within the galaxy. The HI distribution can be estimated from the integrated brightness temperature,

$$T_{Bint}(\hat{\sigma}) = \int T_B(\hat{\sigma},v)dv \qquad (2\text{-}23)$$

and the average velocity field is given by

$$V(\hat{\sigma}) = \int vT_B(\hat{\sigma})dv/T_{Bint}(\hat{\sigma}) \qquad (2\text{-}24)$$

where v is the relative line of sight velocity between the telescope and the source of radiation. If this is taken as the approach velocity, the relation with frequency is

$$v = c/\nu_1 \times (\nu - \nu_1) \qquad (2\text{-}25)$$

with ν_1 as the rest frequency of the spectral line. Neutral hydrogen radiates at 1420.405 MHz and the conversion factor is 4.74 kHz/(km s^{-1}).

In practice, the measuring instrument modifies the forms of (2-23) and (2-24). The actual quantities obtained are

$$\begin{aligned}\overline{T}_{Bint}(\hat{\sigma}) &= \int T_{Bint}(\hat{\sigma}')P(\hat{\sigma}')P_s(\hat{\sigma}'-\hat{\sigma})d\hat{\sigma}'/\int P(\hat{\sigma}')P_s(\hat{\sigma}'-\hat{\sigma})d\hat{\sigma}' \\ \overline{V}(\hat{\sigma}) &= \int v(\hat{\sigma}')T_{Bint}(\hat{\sigma}')P(\hat{\sigma}')P_s(\hat{\sigma}'-\hat{\sigma})d\hat{\sigma}'/ \\ &\quad \int T_{Bint}(\hat{\sigma}')P(\hat{\sigma}')P_s(\hat{\sigma}'-\hat{\sigma})d\hat{\sigma}' \qquad (2\text{-}26)\end{aligned}$$

Criteria on the frequency response of the receiver have been obtained (Rogstad and Shostak 1971) such that the above quantities can be derived from the measurements as

$$\overline{T}_{Bint}(\hat{\sigma}) = \Sigma T_{B_{oi}}(\hat{\sigma})\Delta_v$$
$$\overline{V}(\hat{\sigma}) = \Sigma v_i T_{B_{oi}}(\hat{\sigma})\Delta_v / \overline{T}_{Bint}(\hat{\sigma}) \quad (2\text{-}27)$$

where $T_{B_{oi}}(\hat{\sigma})$ is the observed brightness temperature of the ith channel, Δ_v is the velocity increment between adjacent channels, and v_i is the velocity centroid of the ith channel.

The telescope measures an observed brightness temperature given by

$$T_{B_{oi}}(\hat{\sigma}) \simeq \int\int T_B(\hat{\sigma}',v)P(\hat{\sigma}',v)f_i(v)P_s(\hat{\sigma}'-\hat{\sigma},v_i)d\hat{\sigma}'dv / \int\int P(\hat{\sigma}',v)f_i(v)P_s(\hat{\sigma}'-\hat{\sigma},v_i)d\hat{\sigma}'dv \quad (2\text{-}28)$$

The receiver response and its velocity centroid are defined such that

$$\int f_i(v)dv = 1$$
$$\int v f_i(v)dv = v_i \quad (2\text{-}29)$$

When the bandwidth pattern is wide, the beam patterns can be regarded as essentially velocity independent and (2-27) will be equivalent to (2-26) if

$$\Sigma f_i(v)\Delta_v = 1$$
$$\Sigma v_i f_i(v)\Delta_v = v \quad (2\text{-}30)$$

A bank of triangular shaped filters can satisfy these requirements (Allen, Hamaker, and Wellington 1973), but it is not realisable in practice. It is necessary to approximate this by a realisable response. From here onwards, velocity and frequency will be used interchangeably. In general velocity is used in astronomical entities and frequency is used in the engineering aspects.

The required response does not need to have a flat passband. A flat passband is actually detrimental

to the estimate of the velocity field. It provides a staircase estimate instead of a linear estimate. The responses of three realisable filters are compared with that of the triangular shaped filter (Figure 2-6). The single tuned filter gives the best passband response, though it has a rather broad wing. The linear phase filter gives reasonable passband response and a sharper cutoff. Another consideration in choosing a particular filter is the effect of decorrelation. Filters are to be implemented in the signal path of the large antenna only. Each filter introduces extra delay causing a delay mismatch in the two correlating inputs with a corresponding reduction in correlation. The group delay of a filter is an increasing function of the number of reactive elements used in its construction. Miltistage filters are therefore not suitable. A single resonator is used as the frequency selecting element.

The information content at the output of the line receiver is given by (2-19). A bandpass system function can be written as

$$H(\nu) = \tilde{H}(\nu) + \tilde{H}^*(-\nu) \qquad (2\text{-}31)$$

Over the narrow bandwidth of interest,

$$\tilde{H}_1(\nu) = e^{-j\tan^{-1}\{2(\nu - \nu_i)/\Delta\nu\}}/\{1 + (2(\nu - \nu_i))^2\}^{\frac{1}{2}}$$

$$\tilde{H}_2(\nu) = 1 \qquad (2\text{-}32)$$

where ν_i is the resonant frequency, and $\Delta\nu$ is the 3 dB bandwidth, of the single tuned filter. The average output is

$$E\{z(t)\} = \int_0^\infty 2/\{1 + (2(\nu - \nu_i))^2\} \times S_{s'}(\nu)d\nu \qquad (2\text{-}33)$$

where the property that $S_{s'}(\nu)$ is real and even has

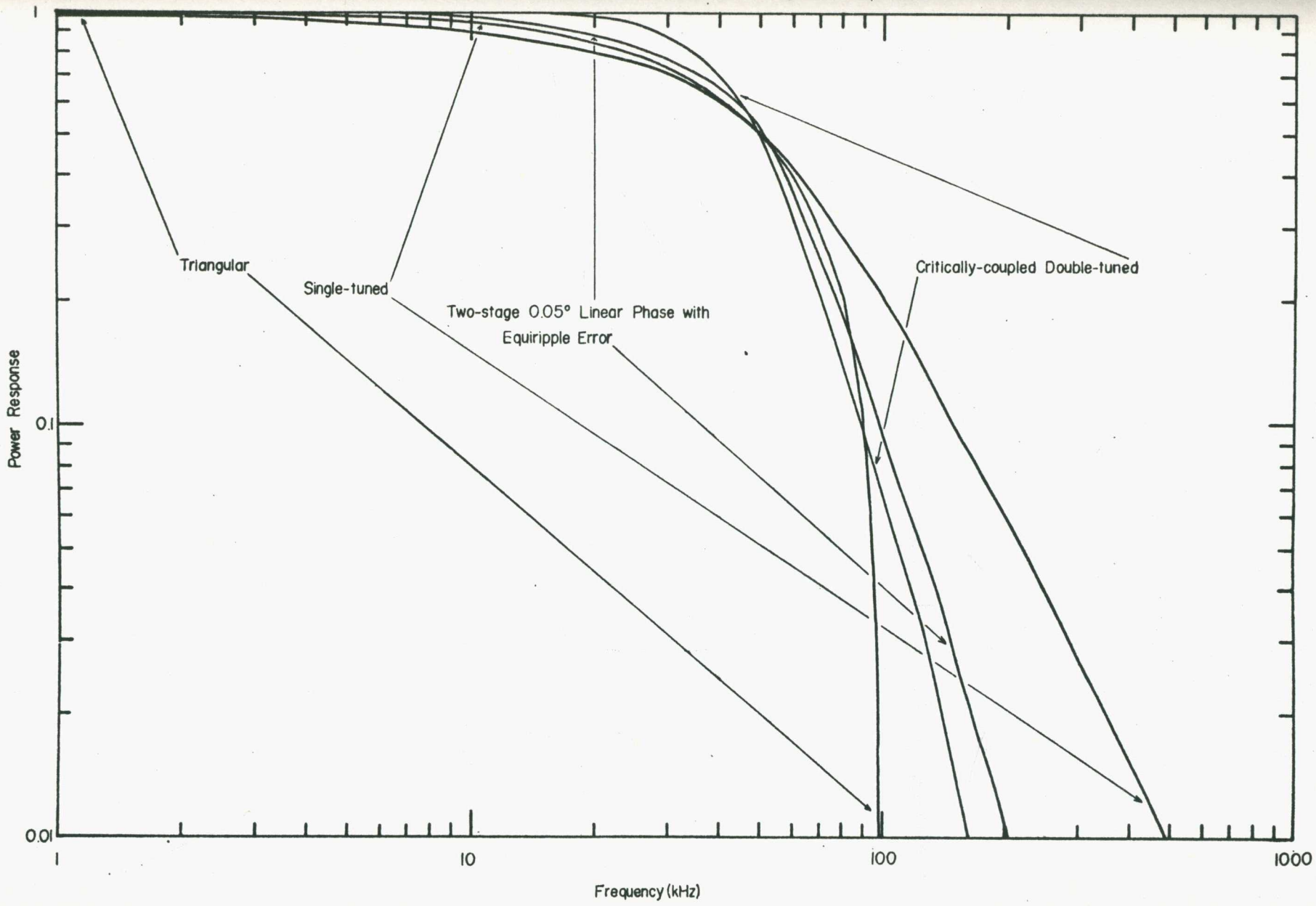

Figure 2-6 Filter Responses

been used. The response function is defined as

$$f_i(\nu) = \{2/(\pi\Delta\nu)\}/\{1 + [2(\nu - \nu_i)]^2\} \qquad (2\text{-}34)$$

This is exactly the same as that which will be obtained when the filter is implemented in both correlating channels. The centroid of the response function is ν_i.

The line receiver is to have a velocity resolution of 30 km/s, corresponding to a half power bandwidth of 140 kHz for the filter. The total velocity coverage is built up from this filter with different velocity centroids. The centroids are spaced 21 km/s, or 100 kHz, apart. The single tuned filter does not satisfy (2-30) exactly. A straight combination of these filter elements actually results in a rather unacceptable response (Figure 2-7). To optimise the final response, each individual element has to be weighted such that

$$\begin{aligned} w_0 \Sigma c_i f_i(\nu)\Delta_\nu - 1 &\simeq 0 \\ w_1 \Sigma \nu_i c_i f_i(\nu)\Delta_\nu - \nu &\simeq 0 \end{aligned} \qquad (2\text{-}35)$$

The weights c_i's minimises the ripple in the passband of the composite response. The weight w_0 brings the response to unit gain. The weight w_1 compensates for a frequency dependent error in the first moment. That the w's are different in practice can be deduced from (2-29) and (2-30). These weights can be regarded as modifiers to the channel spacing. From the zeroth moment criterion, the channel spacing is

$$\Delta\nu_0 = \Delta\nu_T/i_T \qquad (2\text{-}36)$$

where i_T is the total number of channels and $\Delta\nu_T$ is

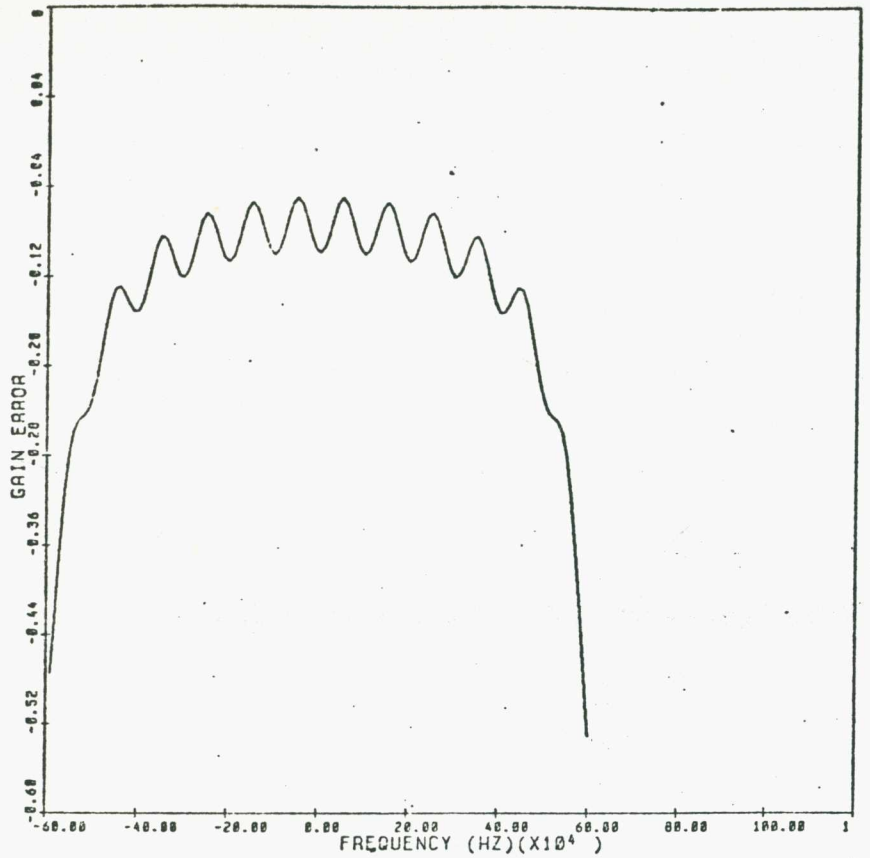

c_i's = 1

w_j's = 1

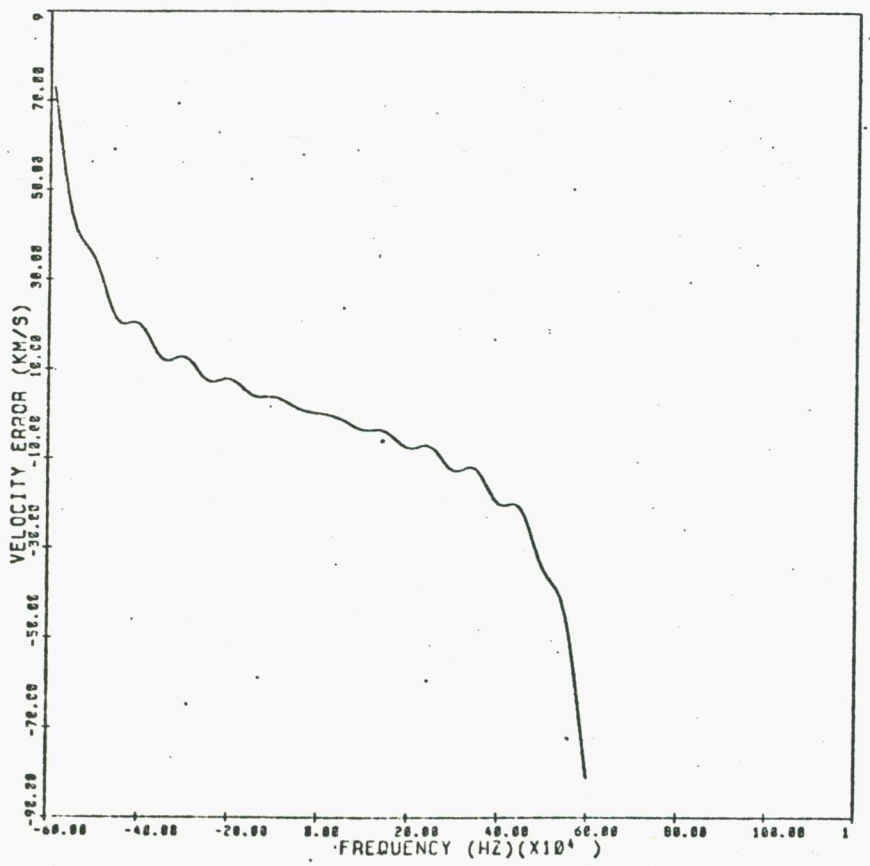

Figure 2-7 Filter Bank Responses, Natural Weighting

the total resulting bandwidth. From the first moment criterion, the channel spacing is

$$\Delta\nu_1 = \nu_j / \{\Sigma\nu_i \int f_i(\nu) f_j(\nu) d\nu\} \qquad (2\text{-}37)$$

The two values of channel spacing are thus effectively different in general.

The weights are determined by the number of elements used in the construction of the final response. An appropriately weighted twelve element bank results in a rms error of 0.019 in gain and 1.35 km/s in velocity (Firgure 2-8). The half power bandwidth of the coverage is 1.3 MHz, or 274 km/s. The coverage for reliable velocity determination is less at 232 km/s. A better estimate of the integrated brightness temperature and the average velocity field is then

$$\begin{aligned} \overline{T}'_{Bint}(\hat{\sigma}) &= w_0 \Sigma c_i T_{B_{oi}}(\hat{\sigma}) \Delta_v \\ \overline{V}'(\hat{\sigma}) &= w_1 \Sigma v_i c_i T_{B_{oi}}(\hat{\sigma}) \Delta_v / \overline{T}'_{Bint}(\hat{\sigma}) \end{aligned} \qquad (2\text{-}38)$$

The performance of the filter bank has been investigated according to the specified parameters of the individual filters. Actual parameters can be expected to differ from the specified ones. The parameter which affects the performance of the filter bank most is the actual channel spacing. Assuming that the radiation is fully covered by the bank, then if the actual spacing is less than that specified, the distribution will be overestimated and the velocity error will exhibit a positive slope. When the velocity is correct at the bank center, the latter means that the velocities are proportionally over or under estimated towards the bank edge. If the spacing is larger than

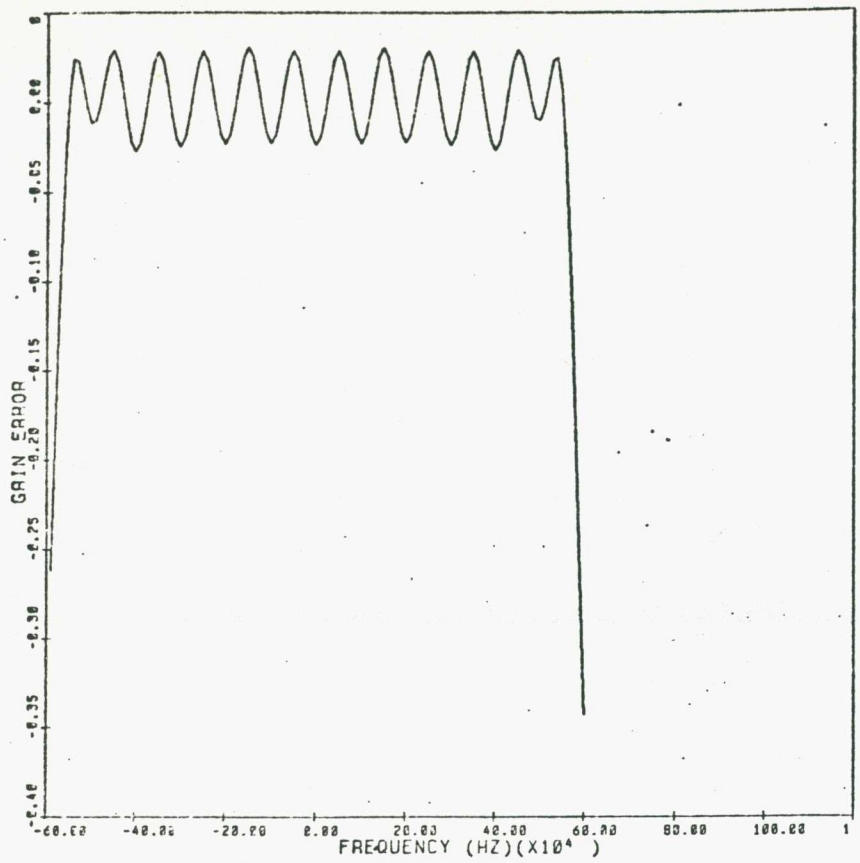

$c_1 = c_{12} = 1.45$

$c_2 = c_{11} = 1.03$

$c_3 = c_{10} = 1.02$

$c_4 = c_9 = 1$

$c_5 = c_8 = 1$

$c_6 = c_7 = 0.99$

$w_0 = 1.08$

$w_1 = 1.17$

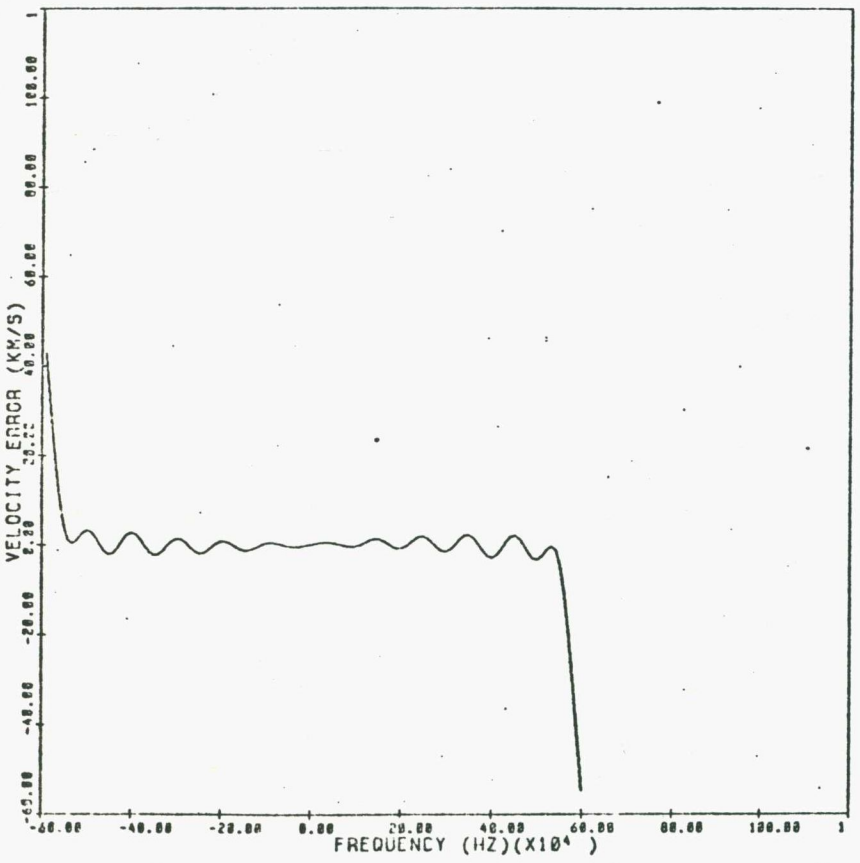

Figure 2-8 Filter Bank Responses, Optimised Weighting

that specified, the corresponding quantities will be in error in the opposite direction. For the designed filter bank, a 10% error in the spacing can result in a 10% error in the estimation of the distribution, and a 10 km/s error in the velocity estimate at the bank edge. To achieve reasonable performance, the channel spacing needs to be set to better than 1%.

2.7 Filter Design

The required filter is a single resonator with a half power bandwidth of 140 kHz centered around the IF of 30 MHz. This small percentage bandwidth, 0.5%, can best be achieved by a helical resonator (Figure 2-9). The structure resembles a quarter wavelength coaxial resonator with a single layer coil as the center conductor. This reduces the cavity length which results in a resonator of manageable size at very high frequencies. Such a resonator has a high quality factor.

Design details for a helical resonator can be found in Zverev (1967). For the line receiver, a cylindrical structure is used. To obtain a good quality factor, the wire diameter of the coil, d_o, is made to be at least five times its skin depth. The physical design of the resonator is further governed by the following,

$$\begin{aligned} &0.4 < nd_o < 0.6 \\ &d/D = 0.55 \\ &b = 8.1(10)^3\{\ln(D/d)/\{1 - (d/D)^2\}^{\frac{1}{4}}/(n\nu_i)^{\frac{1}{2}} \\ &b/d = 1.5 \end{aligned} \tag{2-39}$$

where n is the number of turns per unit length, d

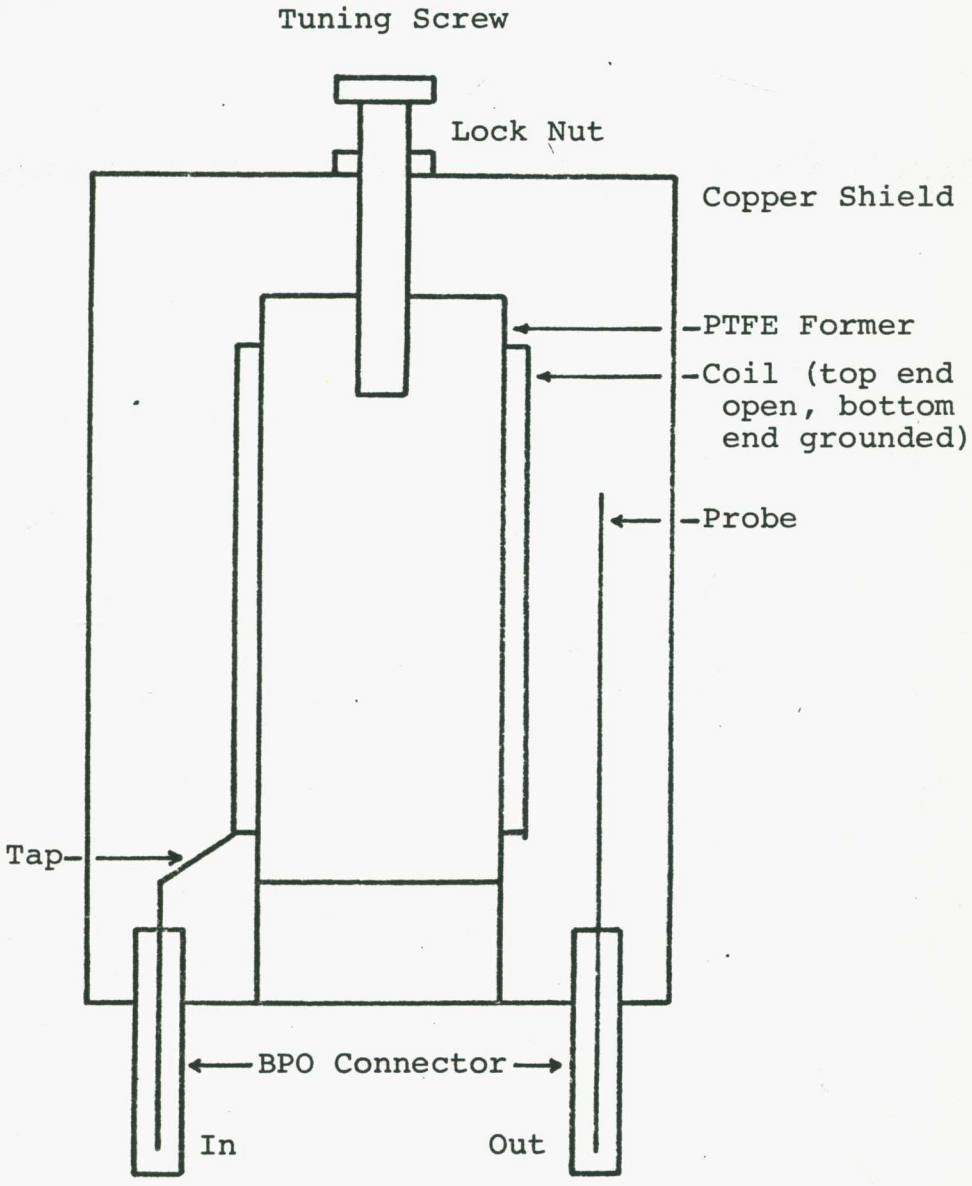

Figure 2-9 Helical Resonator

is the mean diameter of the coil, D is the inside diameter of the cavity, and b is the axial length of the coil. All dimensions are in meters. The characteristic impedance of the resonator is

$$Z_o = 183nd\{(1 - (d/D)^2)\ln(D/d)\}^{\frac{1}{2}} \qquad (2\text{-}40)$$

For an air filled cavity, the quality factor is mainly determined by conductor loss. When the conductor is copper, the unloaded quality factor of the resonator is

$$Q_u = 8.66D\sqrt{\nu_i} \times \{d/D - (d/D)^3\}/\{1.5 + (d/D)^3\} \qquad (2\text{-}41)$$

The present resonator is made out of a length of copper tubing 0.11 m long with a diameter of 0.076 m. This gives a Q_u of 830, which can be compared with the minimum required quality factor of 214. A length of polytetrafluoroethylene (PTFE) tubing is used to support the coil. This material has a dissipation factor of 0.0008 at 30 MHz. It is chosen so that the quality factor will not be much degraded. The characteristic impedance is 621 Ω. Signal is fed into the resonator via a tap matched to 70 Ω. The output coupling is via a probe, the length of which is adjusted to provide the required bandwidth when loaded by 70 Ω. The resonant frequency is adjusted by varying the depth of penetration of the tuning screw down the axis of the coil.

2.8 Dynamic Range

To fully utilise the dynamic range of the original

continuum receiver, an IF amplifier is placed before the filters. Its function is twofold. Firstly, it compensates for the insertion loss of the filters. Secondly, it compensates for the reduction in the average output level due to the reduction in receiver bandwidth.

The average output of a correlation receiver is given by (2-19). When the signal spectral density is constant over the band of interest,

$$o_s = 2KS_{s'}(\nu_i)H_1(\nu_i)H_2(\nu_i)W \qquad (2\text{-}42)$$

where W is an equivalent bandwidth defined as

$$W = \int H_1(\nu)H_2^*(\nu)d\nu/\{2H_1(\nu_i)H_2^*(\nu_i)\} \qquad (2\text{-}43)$$

To maintain the average output level, the power gain bandwidth product has to be held constant. A reduction in bandwidth should be compensated by a corresponding increase in gain.

In the line receiver, the equivalent bandwidth of a frequency channel is $(\pi/2)\Delta\nu$. The bandwidth is thus reduced from 6 MHz to 220 kHz. The gain should be increased 27 times. If this gain is to be absorbed by one of the two correlating inputs only, the required power gain for that input is 29 dB.

The gain is provided by an IF amplifier built around a linear integrated circuit, the 733 differential video amplifier (Figure 2-10). A 70 Ω two way splitter feeds the amplified signal to the two filters. The required gain of 29 dB is actually not achievable due to saturation of the later IF stages. It is instead set at 20 dB. The loss in dynamic range after correlation is 4.5 dB.

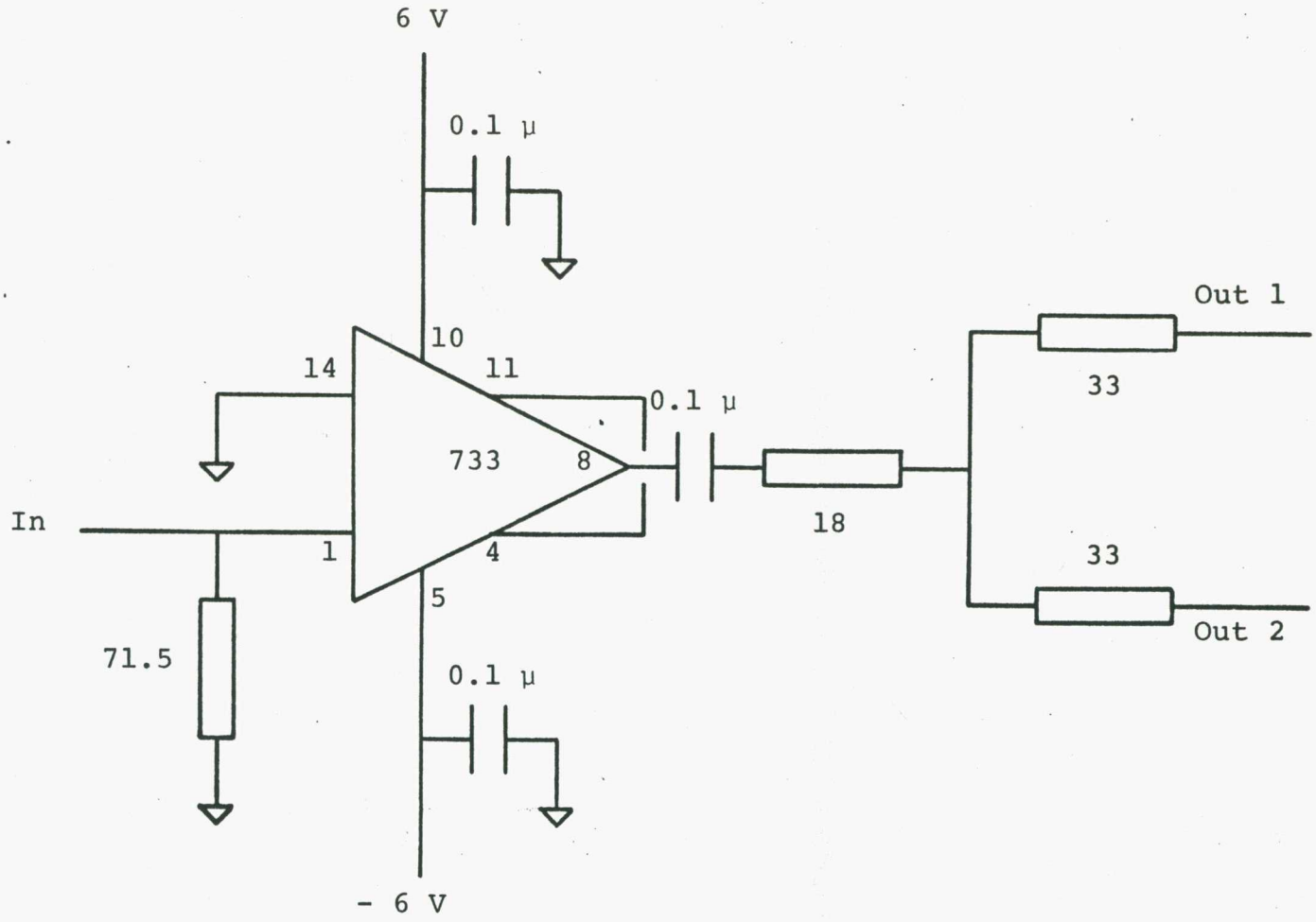

Figure 2-10 Filter IF Amplifier

2.9 Noise

The Fleurs receiver uses IF pilot signals to stop the fringes of the received radiation from the synthesis center. They degrade the noise performance of the receiver. The nature of this noise is investigated in terms of the line receiver and subsequent design minimises its contribution.

The mean square value of the output noise is

$$E\{o_n^2(t)\} = \int S_o'(\nu)d\nu \qquad (2\text{-}44)$$

The output bandwidth is determined by the averaging process. Let its equivalent bandwidth be W_L, then

$$E\{o_n^2(t)\} = 2W_L S_o'(0) \qquad (2\text{-}45)$$

From (2-21), when $|H_3(0)|^2$ is unity, $S_o'(0)$ is the same as $S_z'(0)$, and

$$S_o'(0) = S_{n_1}(\nu) * S_{n_2}(\nu) + S_{n_1}(\nu) * S_{p_2}(\nu) + S_{p_1}(\nu) * S_{n_2}(\nu)|_{\nu = 0} \qquad (2\text{-}46)$$

Over the bandwidth of interest, n'(t) can be regarded as having a flat spectral distribution. The noise spectral densities at the inputs to the correlator are then determined by the individual channel transfer function. If V_{n_1} and V_{n_2} are their rms values, their spectral densities will be

$$\begin{aligned} S_{n_1}(\nu) &= (V_{n_1}^2/2)\{f_i(-\nu) + f_i(\nu)\} \\ S_{n_2}(\nu) &= \{V_{n_2}^2/(2W_c)\}\{u(\nu + \nu_p + W_c/2) - \\ &\quad u(\nu + \nu_p - W_c/2) + u(\nu - \nu_p + W_c/2) - \\ &\quad u(\nu + \nu_p - W_c/2)\} \end{aligned} \qquad (2\text{-}47)$$

where W_c is the 6 MHz bandwidth of the small antennas, ν_p is the 30 MHz pilot frequency, and u(*) is the step function. Similarly, if V_{p_1} and V_{p_2} are the

respective rms values of the pilots, their spectral densities are

$$S_*(\nu) = (V_*^2/2)\{\delta(\nu + \nu_p) + \delta(\nu - \nu_p)\} \qquad (2\text{-}48)$$

where * can be p_1 or p_2, and $\delta(\cdot)$ is the impulse function. The convolutions in (2-46) are then

$$S_{n_1}(\nu) * S_{n_2}(\nu)|_{\nu = 0} = \{V_{n_1}^2 V_{n_2}^2/(2\pi W_c)\} \times \{\tan^{-1}(2/\Delta\nu \times (\delta\nu + W_c/2)) - \tan^{-1}(2/\Delta\nu \times (\delta\nu - W_c/2))\}$$

$$S_{n_1}(\nu) * S_{p_2}(\nu)|_{\nu = 0} = \{V_{n_1}^2 V_{p_2}^2/(\pi\Delta\nu)\}/\{1 + (2\delta\nu/\Delta\nu)^2\}$$

$$S_{p_1}(\nu) * S_{n_2}(\nu)|_{\nu = 0} = V_{p_1}^2 V_{n_2}^2/(2W_c) \qquad (2\text{-}49)$$

where $\delta\nu$ is the difference frequency of ν_p and ν_i. When $V_{n_1} = \gamma V_{n_2} = \gamma V_n$ and $V_{p_1} = V_{p_2} = \kappa V_n$, the mean square value of the output noise becomes

$$E\{o_n^2(t)\} = V_n^4 W_L/W_c \times \{k_1\gamma^2/(\pi W_c) + 2k_2\gamma^2\kappa^2/(\pi\Delta\nu) + \kappa^2/W_c\} \qquad (2\text{-}50)$$

where k_1 and k_2 encompasses the terms containing $\delta\nu$. The degradation in receiver sensitivity is

$$D_p = \{1 + \kappa^2/k_1 \times (2k_2 W_c/\Delta\nu + \pi/\gamma^2)\}^{\frac{1}{2}} \qquad (2\text{-}51)$$

The Fleurs spectral line receiver is designed to acheive a small D_p. The predetermined parameters are $\kappa = 0.2$, $W_c = 6$ MHz, and $\Delta\nu = 140$ kHz. The parameter γ is selected from a consideration of receiver dynamic range, and is set to be 3. The only parameters left are k_1 and k_2, which are functions of $\delta\nu$. From a noise performance viewpoint, $\delta\nu$ should be made as large as possible (Figure 2-11). Tracking requirements however dictate a small $\delta\nu$. A value of 300 kHz is selected. Under these conditions, the degradation in

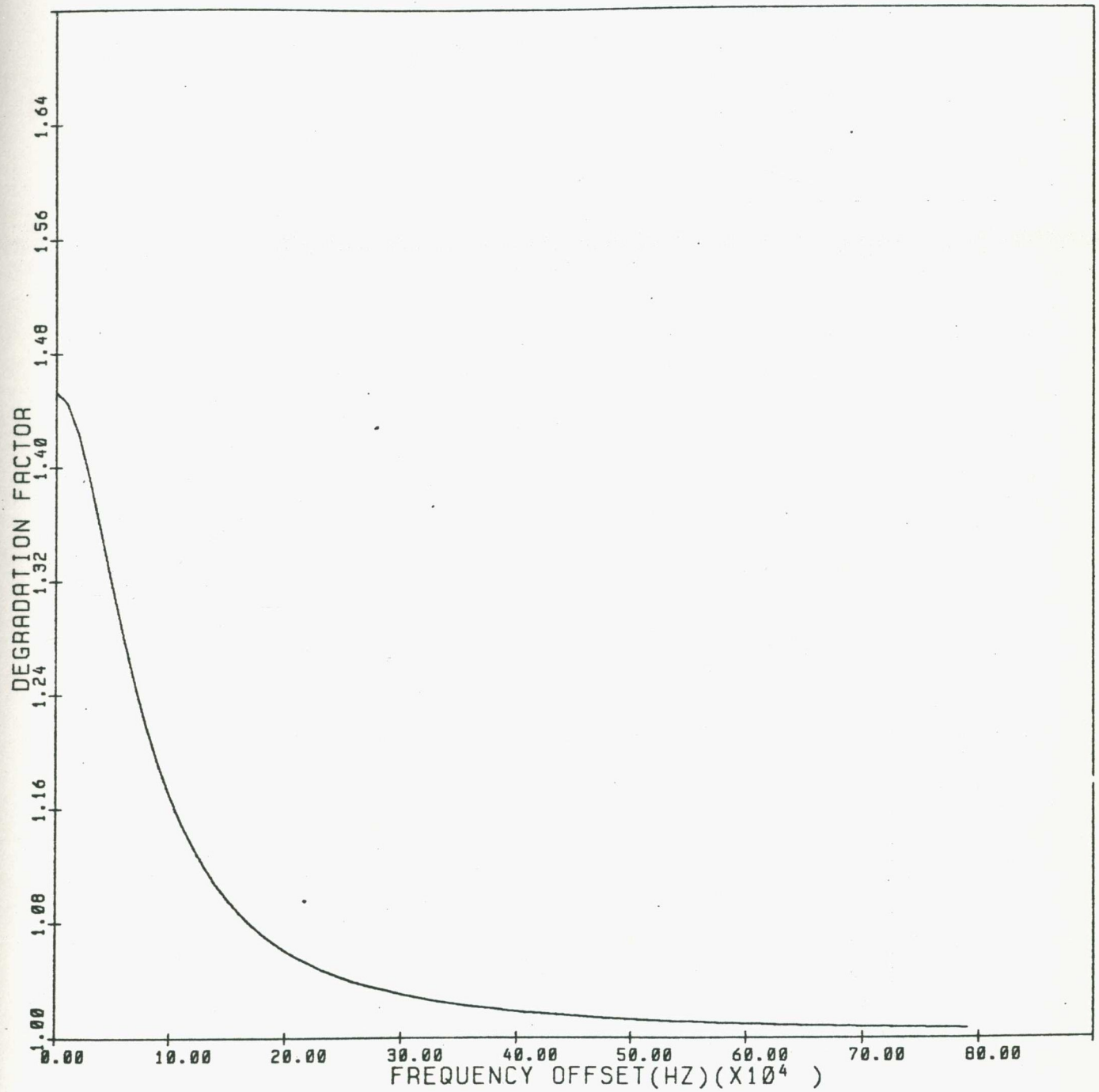

Figure 2-11 Sensitivity Degradation Due to the Pilot

sensitivity due to the pilots is 1.03.

The two filters are arranged symmetrically on either side of the pilot frequency (Figure 2-12). They are thus 600 kHz apart. Six observations in steps of 100 kHz are required to obtain a total bandwidth of 1.3 MHz. This arrangement is best suited for groups of 12 frequency channels.

2.10 Tracking

The FST tracks a source of radiation across the sky through three mechanisms. One, each antenna is mechanically driven to follow the source. This maximises the source illumination on the antenna. Pairs of these antennas provide the baselines for the synthesis telescope. The telescope itself is driven electronically such that radiation from the synthesis center produces constant receiver outputs. This is performed in two parts at the IF of 30 MHz. Two, a system of pilot signals tracks the receiver phase. Three, a system of cables tracks the signal delay between the two correlating channels.

The electronic tracking mechanism will be investigated in terms of the line receiver. The signal flow is as depicted in Figure 2-13. Constant phase components can be calibrated out and are not shown. The pilots contain phase tracking information which is applied to the signals during correlation. Signal in one input is derotated with respect to the signal in the other input such that they are both in phase. The amount of derotation is determined by the phase difference

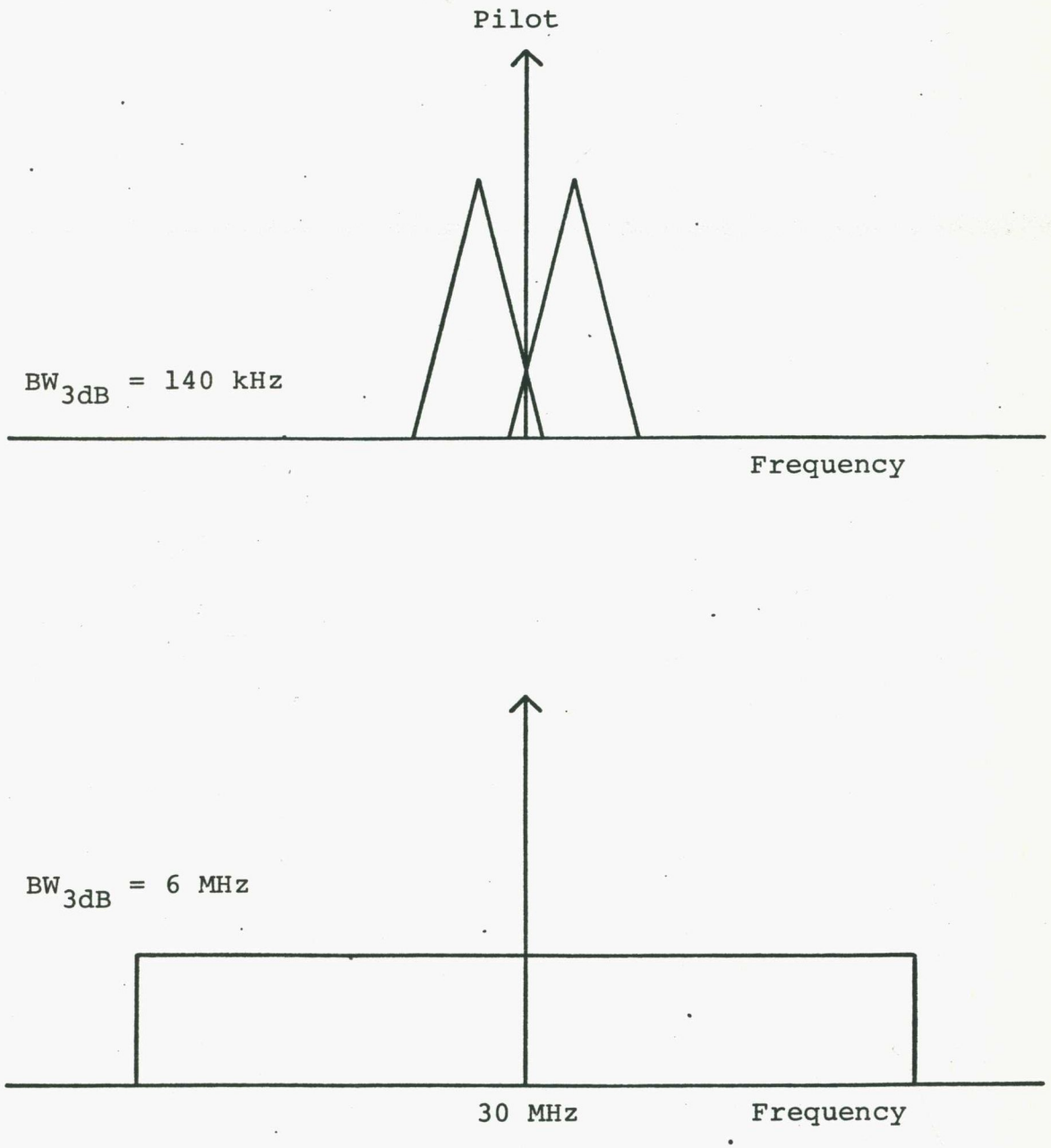

Figure 2-12 Frequency Response of the Correlating Channels

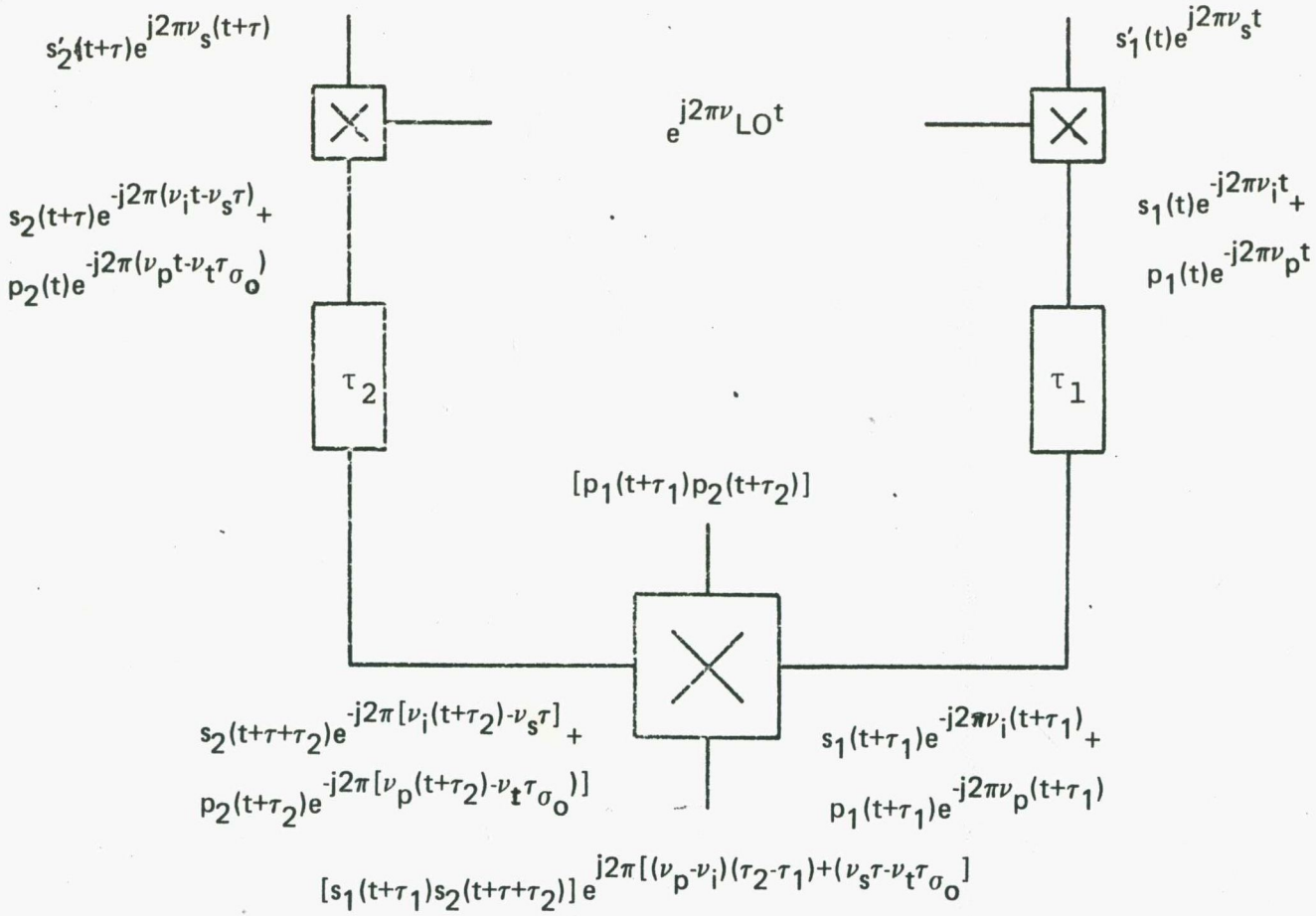

Figure 2-13 Signal Flow Diagram

between the two correlating pilots. Referring to Figure 2-13, the signal in input 2 will be derotated by

$$\psi_t = 2\pi\{\nu_p \times (\tau_2 - \tau_1) - \nu_t\tau_{\sigma_o}\} \qquad (2\text{-}52)$$

where ν_p and ν_t are respectively the frequencies of the pilots and of the observation. The pilots then produce an output of zero phase after multiplication. The signals however produce a multiplier output with a phase

$$\psi = 2\pi\{(\nu_p - \nu_i)(\tau_2 - \tau_1) + \nu_s\tau - \nu_t\tau_{\sigma_o}\} \qquad (2\text{-}53)$$

where ν_s is the signal frequency. The signals come from the lower sideband of the mixing process (Figure 2-14) and

$$\nu_p - \nu_i = \nu_s - \nu_t \qquad (2\text{-}54)$$

When the radiation is from the synthesis center, the phase of the receiver output becomes

$$\psi = 2\pi(\nu_s - \nu_t)(\tau_{\sigma_o} + \tau_2 - \tau_1) \qquad (2\text{-}55)$$

If the delay tracking is continuous, the phase will be zero. In practice, the delay is tracked in discrete steps and the output is phase modulated by an error when $\nu_s \neq \nu_t$.

The delay tracking is required because of the finite receiver bandwidth. It has been designed to maximise the signal correlation of the original receiver. The line receiver has an inherent imbalance in the delay between the two correlating channels. The signal correlation improves for too low a delay setting, and degrades for too high a delay setting. The output contains a ripple with a frequency determined by the change of a delay unit. The change in correlation

Figure 2-14 Relationship Between the RF and IF

is due to changes in the shape of the receiver response. With delay errors $\delta\tau$, the response is (Figure 2-15)

$$\tilde{H}_1(\nu) = 1/\{1 + (2/\Delta\nu \times (\nu - \nu_i))^2\}^{\frac{1}{2}} \times \cos\{\tan^{-1}(2/\Delta\nu \times (\nu - \nu_i)) - 2\pi(\nu - \nu_i)\delta\tau\} \quad (2\text{-}56)$$

The effect of a delay error is most noticeable at the wings of the receiver response. The general shape of the response is maintained and there is no change in the centroid frequency.

2.11 Synthesis Beam Error Due to Imperfect Delay Tracking

Two characteristics can be observed about the measurements made by a correlation receiver with discrete delay tracking. The measurements are both phase modulated and amplitude modulated. This is similar to what may occur in a communications system, though in that situation the information is purposely modulated. In the present case, the modulations are actually detrimental to the system performance. Brouw (1971) has investigated their effects on the synthesis beam for an EW array. An analysis more applicable to the FST will now be developed.

It will be assumed that the radiation comes from the synthesis center. The result can be extended by applying the shifting property of the Fourier transform. The measured quantity is

$$b(r_x, r_y', \nu) = S_a(1 + \delta A)e^{j\delta\psi} \quad (2\text{-}57)$$

where δA and $\delta\psi$ are respectively the amplitude and the phase errors. The time difference between the radiation arriving at the two antennas of an interferometer

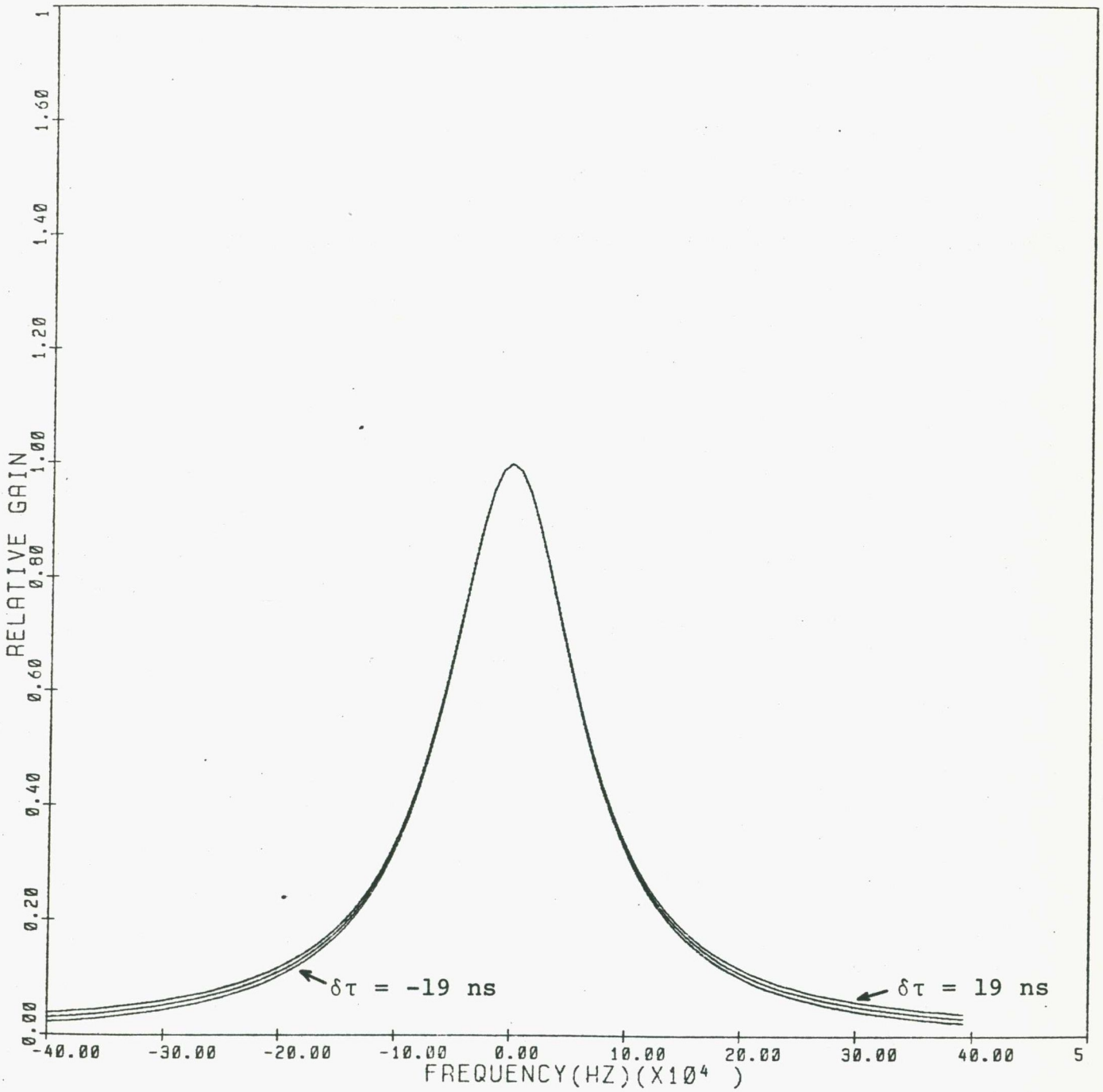

Figure 2-15 Effect of Delay Error on Receiver Response

is

$$\tau_{\sigma_o} \simeq r'_y/c \times \cos(\delta_{\sigma_o}) \qquad (2\text{-}58)$$

This is tracked such that the allowable maximum delay error is $\delta\tau_M$ (Figure 2-16). The error follows a sawtooth waveform and can be Fourier expanded as

$$\delta\tau = (2\delta\tau_M/\pi) \sum_{k=1}^{\infty} \{(-1)^{k+1}/k\} \sin(k\pi r'_y/r'_{y_M}) \qquad (2\text{-}59)$$

where $r'_{y_M} \simeq c\delta\tau_M/\cos(\delta_{\sigma_o})$.

The phase error is

$$\delta\psi = 2\pi\delta\nu\delta\tau \qquad (2\text{-}60)$$

The variation in amplitude has a similar period in r'_y. The form of the variation depends on the receiver and can be represented in general by the Fourier series,

$$\delta A = \sum_{i=0}^{\infty} a_i \sin(i\pi r'_y/r'_{y_M} + \phi_i) \qquad (2\text{-}61)$$

The exponential term in (2-57) can be seen to be an infinite product of exponential terms, each of which is a periodic function in r'_y of frequency $k/(2r'_{y_M})$. These can also be Fourier expanded. Equation (2-57) now becomes

$$b(r_x, r'_y, \nu) = S_a\{1 + \sum_{i=0}^{\infty} a_i \sin(i\pi r'_y/r'_{y_M} + \phi_i)\} \prod_{k=1}^{\infty} \sum_{n=0}^{\infty} J_n\{(2\delta\tau_M/\pi)\{(-1)^{k+1}/k\}\} e^{jnk\pi r'_y/r'_{y_M}} \qquad (2\text{-}62)$$

In the sky domain, spurious responses can be expected to exist at the synthesis center and at regular intervals along the m axis, the interval being $\{2(\nu/c)r'_{y_M}\}^{-1}$.

When $\delta\psi << 1$, (2-57) can be approximated by

$$b(r_x, r'_y, \nu) \simeq S_a(1 + \delta A + j\delta\psi) \qquad (2\text{-}63)$$

Three distinct components can now be distinguished. The first gives rise to a beam expected from a perfect

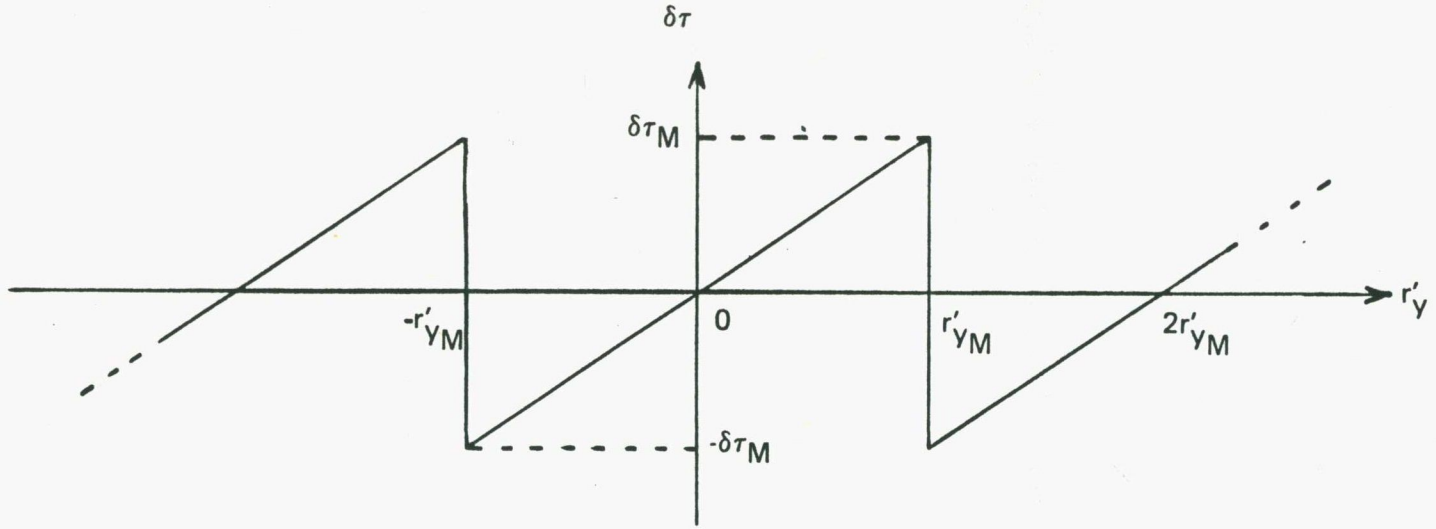

Figure 2-16 Delay Error

instrument. The last two give rise to error beams. To simplify further analysis, it will be assumed that the aperture is a rectangle bounded by $-r_{x2} < r_x \leq r_{x2}$ and $-r'_{y2} < r'_y \leq r'_{y2}$. For an Earth rotational synthesis telescope, measurements are performed on only half of the aperture, the illumination on the other half is obtained via the assumed Hermitian property of the aperture distribution. Specifically, an EW array covers the positive r_x half plane and a NS array covers the positive r'_y half plane.

The error beam as a result of phase modulation is

$$\delta P_{\psi}(l,m,\nu) \simeq 4\pi\delta\nu(\nu/c)^2 \int\int \delta\tau \sin\{2\pi(\nu/c)(lr_x + mr'_y)\} dr_x dr'_y \qquad (2\text{-}64)$$

The result is the same for both the EW and NS cases,

$$P_{\psi W,S}(l,m,\nu) \simeq 2\delta\nu\delta\tau_M\{4(\nu/c)^2 r_{x2} r'_{y2}\}\sin(x)/x \times \sum_{k=1}^{\infty} \{(-1)^{k+1}/k\}\{\sin(y_{k-})/y_{k-} - \sin(y_{k+})/y_{k+}\} \qquad (2\text{-}65)$$

where $x = 2\pi(\nu/c)lr_{x2}$ and $y_{k\pm} = \pi(\nu/c)\{k/\{(\nu/c)r'_{y_M}\} \pm 2m\}r'_{y2}$. The error beam consists of responses which are even in both l and m. At 1420 MHz, these responses occur at $m \simeq \pm 0.019k\cos(\delta_{\sigma_o})$, or $1.09k\cot(\delta_{\sigma_o})$ degrees, from the synthesis center in declination. The relative intensities at these positions as compared with the field center intensity are given by the aperture area normalised values. with the FST, $\delta\tau_M$ is 19 ns. The two frequency channels of the line receiver are arranged to give a $\delta\nu$ of ± 300 kHz. The relative intensity for the kth component is $\pm 0.011(-1)^{k+1}/k$. The absolute value

of the first pair of maxima is 1.1% of the maximum of the true response.

The error beam as a result of amplitude modulation is

$$\delta P_A(l,m,\nu) \simeq 2(\nu/c)^2 \iint \delta A \cos\{2\pi(\nu/c)(lr_x + mr'_y)\} dr_x dr'_y \qquad (2\text{-}66)$$

The result is not the same for the EW and the NS cases. In the EW case, the error beam is

$$\delta P_{AW}(l,m,\nu) \simeq \tfrac{1}{2}\{4(\nu/c)^2 r_{x2} r'_{y2}\} \sum_{i=0}^{\infty} a_i \{\sin(x)/x \times \{\sin(y_{i-})/y_{i-} + \sin(y_{i+})/y_{i+}\}\sin(\phi_i) - \{1 - \cos(x)\}/x \times \{\sin(y_{i-})/y_{i-} - \sin(y_{i+})/y_{i+}\} \cos(\phi_i)\} \qquad (2\text{-}67)$$

In the NS case, the error beam is

$$\delta P_{AS}(l,m,\nu) \simeq \tfrac{1}{2}\{4(\nu/c)^2 r_{x2} r'_{y2}\} \sum_{i=0}^{\infty} a_i \sin(x)/x \times [\{\sin(y_{i-})/y_{i-} + \sin(y_{i+})/y_{i+}\}\sin(\phi_i) + \{\{1 - \cos(y_{i-})\}/y_{i-} + \{1 - \cos(y_{i+})\}/y_{i+}\} \cos(\phi_i)] \qquad (2\text{-}68)$$

The coefficients a_i can be determined when the amplitude variation is known. For the present spectral line receiver, the determination of the coefficients is rather involved. However, some qualitative comments can be made. As noted in the previous section, over each delay setting, the amplitude variation is monotonic. This results in a series dominated by the sine components. Letting $\phi_i = 0$, the EW error beam results in responses which are odd in l and even in m, while the NS error beam results in responses which are even in l and odd in m. The position of these responses is the same as that of the phase modulated case.

Of the two types of errors, only the phase error can be easily corrected. The amplitude error has a range which depends on the radiation structures. Any attempt to remove this error will at best be an estimate.

Correction of the amplitude error can best be achieved in the map domain. For a point radiation structure, the range of the error is a fixed proportion of the radiated intensity. A synthesised beam can be generated with this error incorporated. A map enhancement technique known as CLEAN can then remove the error from a radiation field.

2.12 Sensitivity of the Fleurs Spectral Line Receiver

The point source sensitivity of a synthesis telescope is given by (1-54). An estimate of the sensitivity of the line receiver can be made from the present sensitivity of the continuum receiver. The main difference between the two cases is the receiver bandwidth which is (Tiuri 1964)

$$\Delta\nu_r = \{\int H_1(\nu)H_2^*(\nu)d\nu\}^2 / \int |H_1(\nu)|^2 |H_2(\nu)|^2 d\nu \qquad (2\text{-}69)$$

This is $(\pi/2)\Delta\nu$ for the line receiver. It can be compared with the case when the correlating channels are identical. When both channels are bandlimited by single tuned filters, the receiver bandwidth is twice as wide. One consequence of using filters in only one channel is to degrade the receiver sensitivity by a factor of $\sqrt{2}$.

The noise level on a Fleurs continuum map synthesised

from 64 spacings over 8 hours is, with a baseline proportional Gaussian weighting, 7 mJy. The receiver bandwidth is reduced from 6 MHz to 220 kHz and the number of spacings is reduced to 32. The noise level on a corresponding line map is then 50 mJy. The minimum detectable brightness temperature is given by (1-55). For a map of the pole synthesised by an EW array, T_{Bmin} is 3.2 K. The estimated upper limit on the noise level for a line map synthesised over 16 hours by both the EW and NS arrays is 2.3 K.

2.13 Sensitivity Improvement

The sensitivity of the FST is rather restrictive for HI work on external galaxies. Their HI brightness is rather low. With a maximum angular resolution of 1.3' arc, the maximum brightness temperature that can be expected is 30 K. Considering only galaxies which are fully covered by the 1.2^{o} primary beam of the FST, four galaxies in the southern hemisphere can be expected to have a HI brightness approaching that maximum. They are N55, N300, N3109, and N6822. The sample includes three irregular galaxies (N55, N3109, and N6822) and one Sc spiral galaxy (N300). Improving the receiver sensitivity can widen this list to include other galaxy types.

Sensitivity can be improved by increasing the time spent on a galaxy. It can be brought to below 1 K with six 16 hour observations. For six frequency settings, this adds up to 576 hours per galaxy. Calibration requirements will make this figure even

higher.

This time can be reduced by increasing the number of simultaneous frequency channels. It also improves the relative stability between the channels. A digital backend now being implemented has enough correlators to provide 8 simultaneous frequency channels for 32 spacings. It uses 2 bit quantisation with incomplete products, degrading the sensitivity by 1.15. The 1 K level can be achieved in 224 hours. It has 16 channels over 2 frequency settings instead of 12 channels over 6 frequency channels, thus increasing the coverage by 33%.

A $\sqrt{2}$ improvement in sensitivity is gained by providing filters in both correlating channels. The system noise temperature can be improved by controlling the feed pattern to minimise response spillover and by incorporating low noise preamplifiers on the antennas. The present system temperature of 170 K can be lowered to 80 K, an improvement of 2.1. Better feed design can also increase the aperture efficencies of the antennas. The present figures are 50% for the 13.7 m antenna and 45% for the 5.5 m antennas. An upgrade to 60% should be possible, an improvement of 1.6. If these improvements are realised, the sensitivity will become 0.55 K per channel per 16 hour observation.

2.14 Comparison with other Instruments

Most HI maps of external galaxies have been produced by the Westerbork Radio Synthesis Telescope (WRST).

Two others are the Owens Valley Radio Observatory (OVRO) and the Cambridge Half Mile Telescope. The important characteristics of these synthesis telescopes are listed in Table 2-1. The characteristics of the FST HI instrument are also listed. Of the four, only the FST is so situated as to enable galaxies in the southern celestial sphere to be sampled.

2.15 References

Allen, R. J., J. P. Hamaker, and K. J. Wellington. "The 80-channel Filter Spectrometer for the SRT", Netherlands Foundation for Radio Astronomy, Internal Technical Report 115, 1973.

Bosma, A. "The Distribution and Kinematics of Neutral Hydrogen in Spiral Galaxies of Various Morphological Types". Ph. D. Thesis, The University of Groningen, 1978.

Brouw, W. N. "Data Processing for the Westerbork Synthesis Radio Telescope". Ph. D. Thesis, The University of Leiden, 1971.

Frater, R. H. "The FST Receiver System", Proc. IREE, vol. 34, 309-313, 1973.

O'Sullivan, J. D. "The Development and Use of an Aperture Synthesis Radio Telescope for Polarimetry". Ph. D. Thesis, The University of Sydney, 1974.

Rogstad, D. H. and G. S. Shostak. "Aperture Synthesis Study of Neutral Hydrogen in the Galaxy M101: I. Observations", Astron. & Astrophs., vol. 13, 99-107, 1971.

Tiuri, M. E. "Radio Astronomy Receivers", IEEE Trans. Antennas & Propagation, vol. AP-12, 930-938, 1964.

Zverev, A. I. "Handbook of Filter Synthesis". John Wiley & Sons, Inc., 1967.

Table 2-1 Characteristics of Four Synthesis Telescopes

	FST	Cambridge	OVRO	WSRT
Latitude (degrees)	-34	52	37	53
Number of interferometers	32	1	1	20
Geometrical area/interferometer (m^2)	125	127	1179	982
Velocity resolution (km/s)	30	39	10.5	27
Angular resolution ('')	78	47	120	24
System Temperature (°K)	170	250	75	140

CHAPTER III NEUTRAL HYDROGEN DATA PROCESSING

3.1 A Neutral Hydrogen Observation Program

With the available two channel spectral line receiver, n/2 observations are required to measure n points of the neutral hydrogen spectrum. As these observations are observed at different frequencies, appropriate calibrations are required at these frequencies. A typical observation program will use six frequency settings. A galaxy can be mapped within three weeks.

An observation program can be divided into three main stages, preparation, data collection, and data processing. To prepare the FST for HI observation, two important pieces of information are required. They are the position of the galaxy and its systemic velocity. These are produced by the programs listed in Table 3-1. The position of the galaxy, normally specified for a particular epoch, is precessed to the date of the observation. The systemic velocity of the galaxy is adjusted to produce the current relative velocity between the galaxy and the observatory.

At the observatory, the frequency synthesiser is set to the appropriate local oscillator frequency and the narrowband filters are inserted into the IF return of the large antenna. The generation of tracking information and data collection are controlled by an online General Automation Naked Mini Alpha computer. The observation control software, originally written for continuum work, was adapted by C. K. Kwong for HI work. The observation frequency, the position of

Table 3-1 Preparation Software

Software	Function	Origin
PRSRC	Precession	Fleurs
OPTY	Generation of local oscillator frequency for spectral line observations	CSIRO

the galaxy, the array configuration, and the start hour angle are parameters required by the software. The receiver system automatically configured itself in the HI mode.

Data is collected on a floppy disk as 12 bit words. These are arranged in 30 s blocks, each block containing the data for 64 complex channels. An 8 hour observation accrues 122.88 kwords of data. Each data block is preceded by a header, which contains identifying information about the block.

At the end of an observing session, the recorded data is converted to have an 8 bit word length and transferred to a DEC (Digital Equipment Corporation) tape. The 8 bit word length is required by the present data processing software.

The DEC tape is transported to the Faculty of Engineering Computing Center at the University for processing. This is devided into two stages. In the first stage, the data is conditioned and transformed to produce a map. All operations are performed in the data domain. In the second stage, the map is further treated to extract the required information. Operations are performed in the map domain.

Data from each frequency channel is processed individually. The maximum map size that can be produced at present is 256 x 256 points. The storage requirement is over 128 kbytes, where a byte is 8 bits long. Twelve channels require 1.6 Mbytes of storage.

The first stage of processing is performed

on a PDP11/10 computer. Standard Fleurs software in assembly language is available to process the individual channel data. Because of the storage requirement, map processing is performed on a more powerful computer, the PDP11/45. Special HI software is developed in the FORTRAN language on this computer.

3.2 The Observation Frequency

Given the systemic velocity of the galaxy under observation, the observation frequency can be derived. The Fleurs line receiver makes measurements at two separate frequencies simultaneously. At the IF, one channel is 300 kHz below 30 MHz, and the other channel is 300 kHz above 30 MHz. Because of the nature of lower sideband frequency mixing, the relative position of the two channels is reversed at the IF. If the observation frequency is centered at the systemic velocity of the galaxy, the low IF channel measures the HI approaching (referenced to the systemic velocity) the telescope, and the high IF channel measures the HI receding (referenced to the systemic velocity) from the telescope.

The local oscillator frequency of the FST is determined by the setting of the frequency synthesiser. This is set at half the required frequency. For an observation requiring 6 frequency settings, the synthesiser is set at (Figure 3-1)

$$\nu_{syn} = \nu_{sys} + n \times 50(10)^3 \qquad (3\text{-}1)$$

with n = -2, -1, 0, 1, 2, and 3. The frequency ν_{sys} is calculated by OPTY. It is half the local oscillator

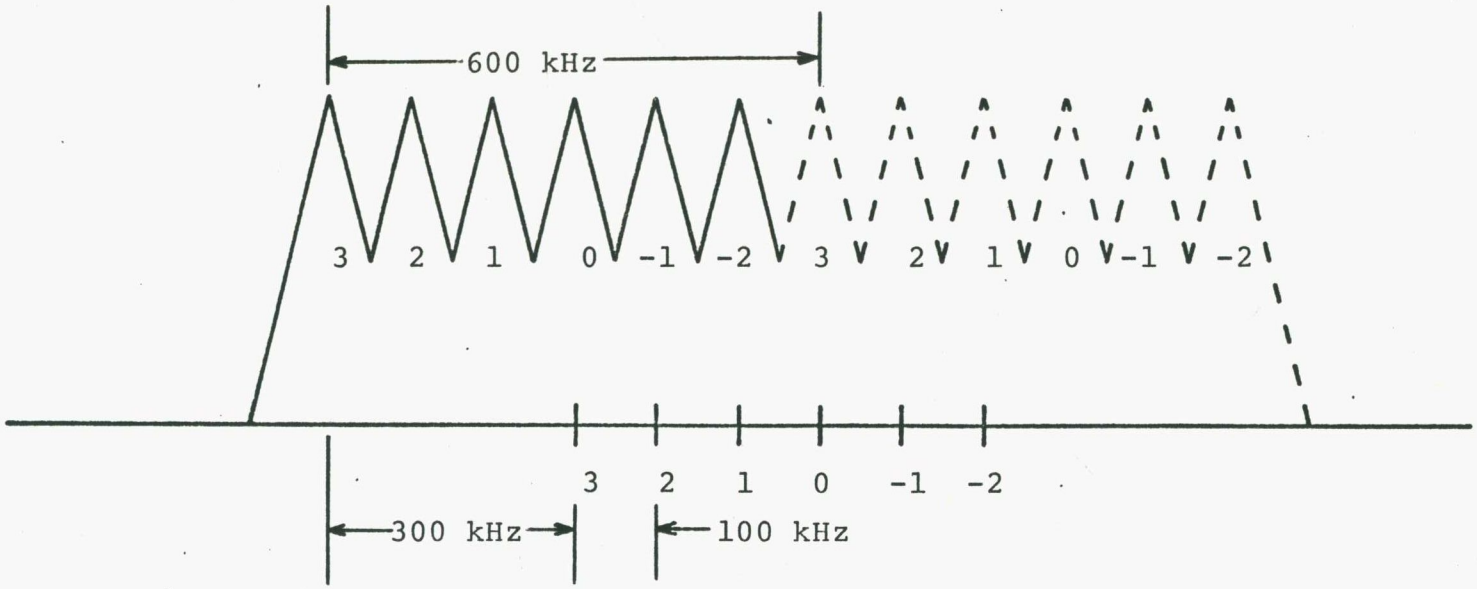

Figure 3-1 Synthesised Total Bandwidth

frequency required for an observation at the systemic velocity.

The relative velocity between the galaxy under observation and the telescope is a function of time. The main component of variation comes from the rotation of the Earth. This is superimposed on a slower variation due to the Earth's orbital motion around the Sun.

The Earth is an ellipsoid with an equatorial radius, R_e, of 6378 km, and a polar radius, R_p, of 6357 km. The component of the rotational velocity of the Earth towards the galaxy is (Figure 3-2)

$$v_r = 2\pi\Omega R_e R_p \{1/(R_p^2 + R_e^2 \tan^2(\theta))\}^{\frac{1}{2}} \sin(h_{\sigma_o}) \cos(\delta) \qquad (3\text{-}2)$$

Over an 8 hour observation at the position of the FST, the variation is $\pm 0.34\cos(\delta)$ km/s with respect to the value at transit, or a frequency variation of $\pm 1.5\cos(\delta)$ kHz. This is less than the expected rms error in velocity that can be achieved by the filter bank and is deemed tolerable. The synthesiser frequency is set to be correct for the galaxy at transit and maintained throughout the observation.

3.3 Processing in the Data Domain

The purpose of this stage is to process the data collected at the observatory to produce a map of the galaxy and the associated synthesised beam pattern (Figure 3-3). The software is described in Table 3-2.

The recorded data are in 30 s blocks and are phase switched by 180° every minute. The first task

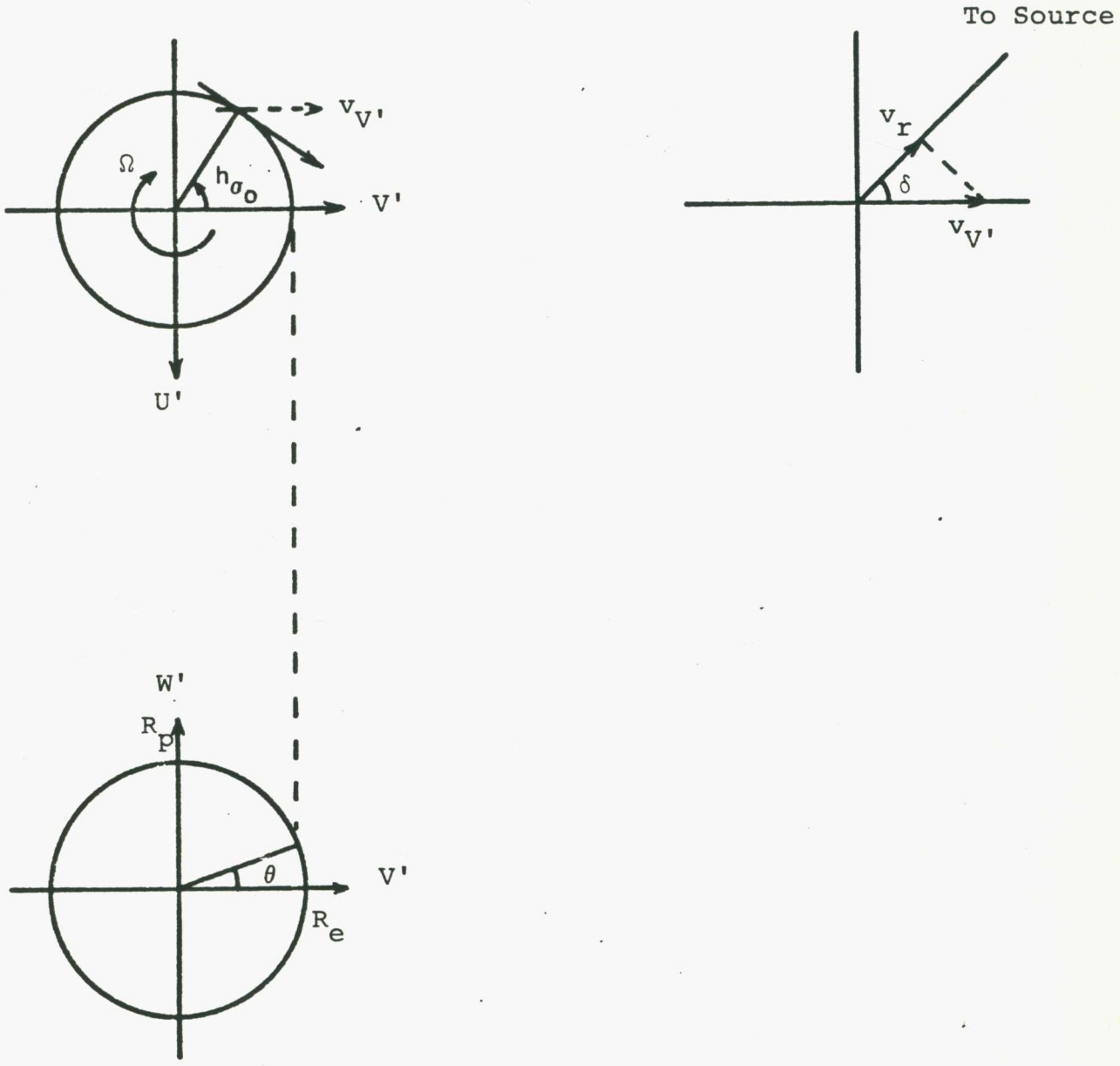

Figure 3-2 Component of Earth's Rotational Velocity Towards the Source

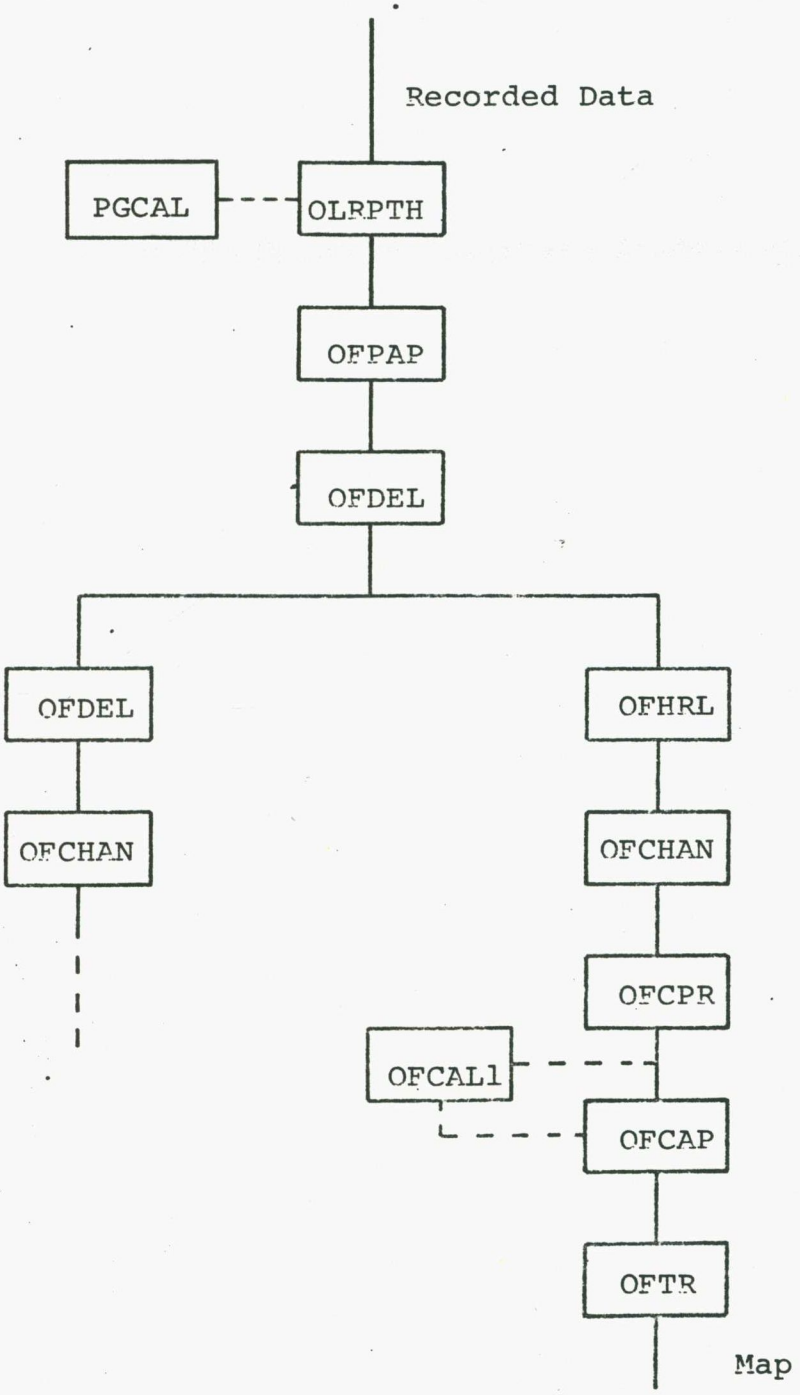

Figure 3-3 Data Processing

Table 3-2 Data Processing Software

Software	Function	Origin
PGCAL	Determination of cosine and sine gain imbalance	Fleurs
OLRPTH	Data check and demodulation	Fleurs modified
OFPAP	Plot of data	Fleurs
OFDEL	Deletion of data	Fleurs
OFHRL	Placement of correlator channels 32 to 63 in words 0 to 31	Author
OFCHAN	Change of information in the data header block	Fleurs
OFCPR	Precession of data	Fleurs
OFCAL1	Evaluation of calibration parameters	Fleurs
OFCAP	Correction of data	Fleurs
OFTR	Transformation of data into map	Fleurs

is to demodulate the data. This is one of the functions of the OLRPTH software. A sample of the printout is shown in Figure 3-4. The software gets information on each data block from the associated header. The header does not contain the frequency information at present and the frequency is entered manually. The data are combined to give 1 minute samples. The demodulation scheme is depicted in Figure 3-5. The format of the processed data is shown in Figure 3-6.

The demodulated data are plotted out for further examination. Suspicious data are deleted. The data are then grouped into two different files, one file containing the low IF channels and one file containing the high IF channels. The file containing the low IF channels is obtained by deleting the high IF channels. The file containing the high IF channels is obtained by swapping the low and high IF channels and then deleting the low IF channels. This is performed by the OFHRL software (Figure 3-7). A consistent file format is thus realised for both files. Data are put in words 0 to 31, arranged in increasing spacing number. A parallel stream of processing can now be performed on the two files.

The signal frequencies in the two files are different from the frequency of observation, ν_t. If a map is produced at ν_t, errors as discussed in 2.3 can be expected. At 1420 MHz, the error in position ($\delta\nu << \nu_t$) is 1.27" arc per degree field per MHz frequency difference. For frequency differences of $\pm$300 kHz,

```
$RU OLRPTH
PRINT ON: #



ONLINE FLEURS       21-MAY-80  11:49:56

NAME= NGC 300
FREQ= 1419.437
SMALL DISH(N/E)=
TEST= S
CHECKS=
PRINT PHASES= N
C/S CORR.= N

DUPLICATE=   #

INPUT:  #DK:E30HA.5S
20:55:30      START TIME
00111100.01101000.00000010.00000001.
00000000.00000000.00001000.00000000.
22:03:30  W  WRONG DEC
22:03:30  W  WRONG RA
22:03:30  W  WRONG DEC
22:03:30  W  PHASE SW. ERROR
22:03:30  W  BLOCKS MISSING
00:37:30  W  WRONG RA
00:37:30  W  WRONG DEC
00:37:30  W  PHASE SW. ERROR
00:37:30  W  BLOCKS MISSING
00:51:30  W  WRONG RA
00:51:30  W  WRONG DEC
00:51:30  W  PHASE SW. ERROR
00:51:30  W  BLOCKS MISSING
02:00:30  W  WRONG DEC
02:00:30  W  WRONG RA
02:00:30  W  BLOCKS MISSING
04:02:30  W  WRONG DEC
04:02:30  W  WRONG RA
04:02:30  W  TIME ERROR
04:02:30  W  PHASE SW. ERROR
04:02:30  W  BLOCKS MISSING
04:28:30  W  WRONG DEC
04:28:30  W  WRONG RA
04:28:30  W  BLOCKS MISSING

   .0 % DELAY ERRORS

INPUT:  #


480 MINUTES


DESCR.=
AVERAGES=
CHANNELS=


STORE: #DK:E30HA.DOA
```

Figure 3-4 Data Check and Demodulation

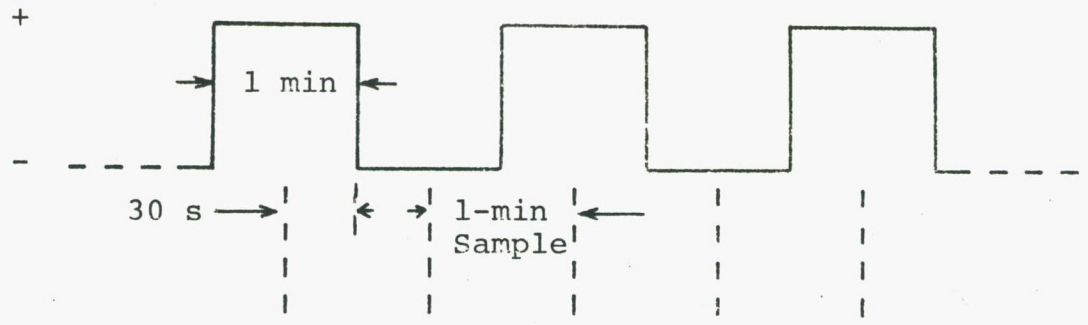

Figure 3-5 Phase Switching and Demodulation

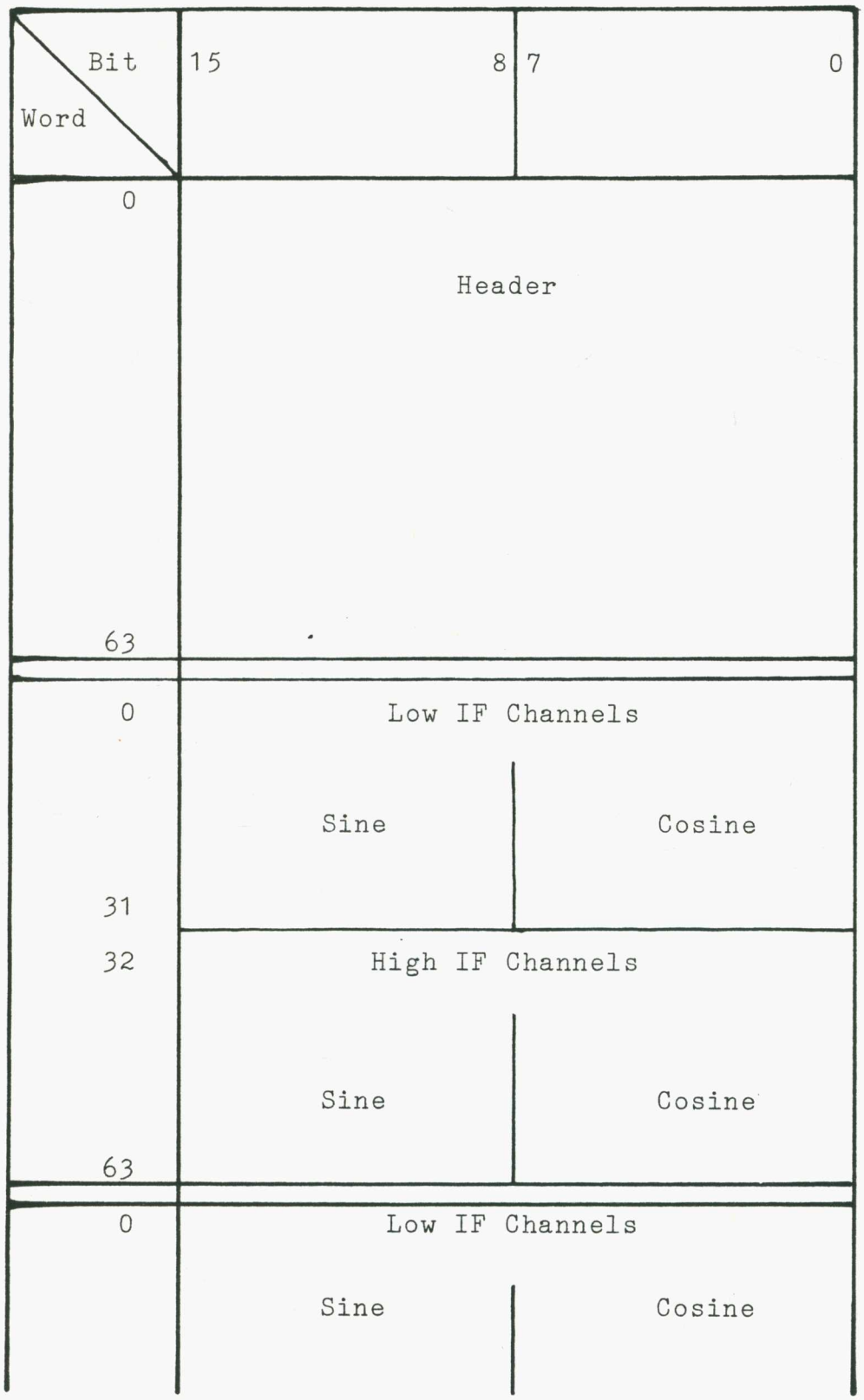

Figure 3-6 Format of Processed Data

```
$RU OFHRL

PRINT ON: #



REPLACE CHANNELS      21-MAY-80   11:54:53


LOAD: #DK:E30HA.D0A
NGC 300 : 480 MINUTES


DESCR.= Y


DESCRIPTION:

NAME          NGC 300
RA (DATE)           13.5031 DEG
DEC(DATE)         -.37.8037 DEG
FREQUENCY         1419.4369 MHZ
OBS. DATE         2814
START-TIME        - 46.1250 DEG
END  -TIME          73.6249 DEG
START-HA          - 59.6282 DEG
INCREMENT            0.2500 DEG
END  -HA            60.1218 DEG
LENGTH             480
X-START              0
GAIN          04,04,04,04,04,04,04,04
ROTATION             0.0000 DEG
OFFSET-RA            0.0000 DEG
OFFSET-DEC           0.0000 DEG
RED. DATE        10142
PANEL SW.           63
SWITCHES      SID-OBS-EW -30 - DC- PC-CI -OFF-
              NPR-NCS-ADN- PS-ADN- CP- DL-NSG-
              INT-ON -OFF-OFF-OFF-OFF-NRM-NRM-
              MPM-OFF-OFF-OFF-OFF-OFF-OFF-OFF-
              LOW-LOW-LOW-LOW-OFF-OFF-OFF-OFF-
              TRS-DMS-PNS-DPS-DLS-  S-X2S-X1S-
              PMS-PGS-DLS-TLO-PAS-SWS-CCS-DLS-
              APM-ADL-ADL-ABD-NGS- LO- SD- LD-


AVERAGES=
CHANNELS=


STORE: #DK:E30HAL.D1A
```

Figure 3-7 Creation of File for High IF Channels

the error is $\pm$0.02%, which at 0.6 degrees from the synthesis center corresponds to an error of $\pm$0.46" arc. The maximum error that can exist between two points is twice that amount. The error is insignificant when compared with the 1.3' angular resolution of the HI instrument. For higher resolution, this can be important. For the same conditions, the error in intensity is 0.05%. It will be noted that the errors increase as the frequency difference increases, and can be significant for wide filter banks. The frequency of the low IF channels is changed to ν_t + 300 kHz. The frequency of the high IF channels is changed to ν_t - 300 kHz.

The data are precessed to a standard epoch of 1950. This enables observations performed at different times to be combined and compared. Deviations from the assumed parameters of the instrument are corrected. These includes imbalance in the cosine and sine channel gains, the stability of the receiver gain and phase, and errors in the baseline lengths and orientations.

The data are now in a form suitable for the generation of the synthesised beam pattern and the map. The transform is performed with a baseline proportional Gaussian weighting with a weight of 0.25 at the 32nd spacing. The number of points required to specify the map is governed by the sampling theorem. The requirement is roughly 4 points per beam.

The beam pattern is the response of the telescope to a point source at the synthesis center. It is obtained by forcing the cosine data to a constant

and the sine data to zero. When the acquired data are perfectly corrected, this will be the synthesised pattern used during the observation, neglecting any position dependent effect. In practice, the correction will not be perfect, and the actual pattern is different. It is important to have the telescope well calibrated to minimise the error in the synthesised pattern. Otherwise the map cannot be interpreted properly.

The transformation from the data domain to the map domain is by the fast Fourier transform algorighm. The algorithm requires the inputs to be arranged on a rectangular grid. For an Earth rotational synthesis telescope, the samples are on concentric arcs. They are convolved onto the aperture plane and then resampled on a rectangular grid, the resampling interval being determined by the size of the map. To provide a sharp definition of the map boundary, the convolution function needs to be a two dimensional sinc function. Such a convolution process demands a huge amount of computing time (Brouw 1971). A Gaussian convolving function is used instead. The drawback is that aliasing occurs at the edge of the map (Figure 3-8). Direct transform hardware is being developed in this School which does not possess this aliasing effect (Frater and Skellern 1978).

The measurement technique used in the FST produces grating rings and sidelobes on the map. This is inherent in a finite discrete sampling system. The FST samples the aperture distribution in steps of 12.192 m along a radial line every one minute. Grating response occurs at a distance of 1^{o} from the radiation field.

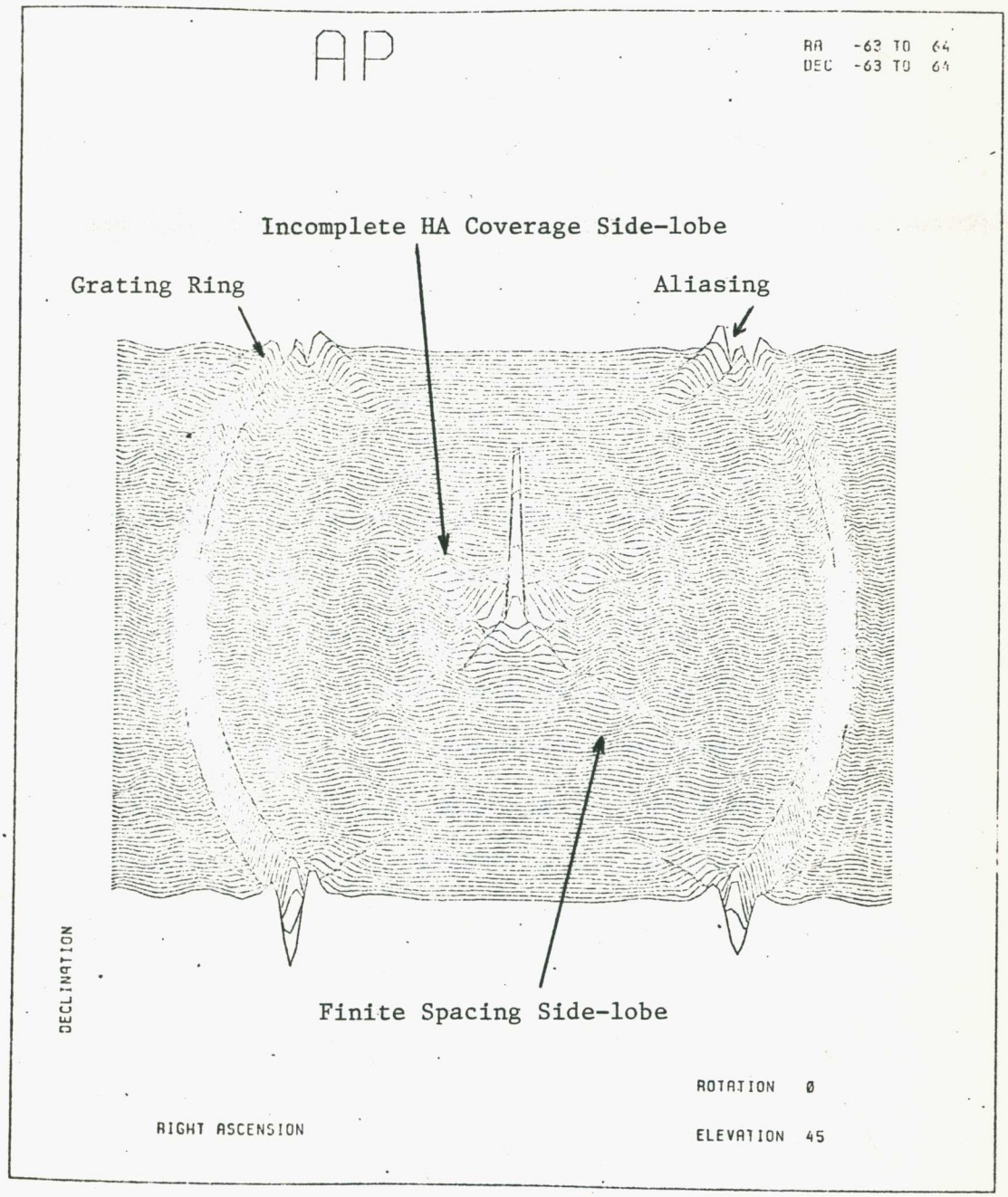

Figure 3-8 A Synthesised Beam Pattern

The finite number of spacings and the incomplete hour angle coverage give rise to the sidelobes. These types of confusion can partially be removed by map enhancement techniques.

A more drastic deficiency of the FST is that it does not measure the innermost part of the aperture distribution. The minimum spacing is 18.288 m and radiation structures wider than 40' arc cannot be properly measured. The incomplete coverage in hour angle at certain declinations (Christiansen 1973) means that structures with certain orientations are not properly measured.

3.4 System Calibration

The data obtained by an instrument cannot be properly interpreted unless the characteristics of the instrument is known. In the case of a synthesis telescope, an exact knowledge of the synthesised beam used to observe a radiation field is of paramount importance. Two main areas which affect the beam is the accuracy to which the baselines of the telescope are known and the stability of the response of the receiver system. Information can be obtained from observation of point sources.

A point source at the synthesis center has a constant visibility function with zero phase. Any departure from these two criteria in an actual measurement can be used to obtain the calibration parameters which are required to correct this departure. Given a knowledge

of the functional dependence of the departure on the hour angle and the declination, the calibration parameters can be obtained by performing a least squares fit on the data (O'Sullivan and Brouw 1973).

Baseline errors result in error in the phase of the measurements (Appendix A). The errors can be separated into three terms, $\cos(\delta_{\sigma_o})\cos(h_r - h_{\sigma_o})$, $\cos(\delta_{\sigma_o})\sin(h_r - h_{\sigma_o})$, and $\sin(\delta_{\sigma_o})$. Point sources at different declinations are observed over the full hour angle coverage of the telescope, which for the FST is $\pm 60^o$ nominal. The accuracy of the $\sin(\delta_{\sigma_o})$ dependence relies on the number of strong point sources available over the declination range. When it is necessary to correct an observation performed at one declination δ_s by baseline parameters obtained at another declination δ_c, the expected error is a constant phase offset proportional to $\sin(\delta_s) - \sin(\delta_c)$ (Figure 3-9),

$$\Delta\psi_\delta = 2\pi\nu/c \times r\{\Delta r/r \times \sin(\delta_r) + \Delta\delta_r \cos(\delta_r) \times \{\sin(\delta_s) - \sin(\delta_c)\} \qquad (3\text{-}3)$$

The main contributions to baseline errors are the inaccuracies in the distance vector between the phase center of two antennas and the center frequency of the receiver. Apparent baseline errors can also result from position errors in the observed point source, or an error in time.

The baseline parameter is a function of frequency. In a HI program, the radiation field is observed over several frequencies. Normally, the baseline parameters are obtained at one frequency only. Errors are introduced

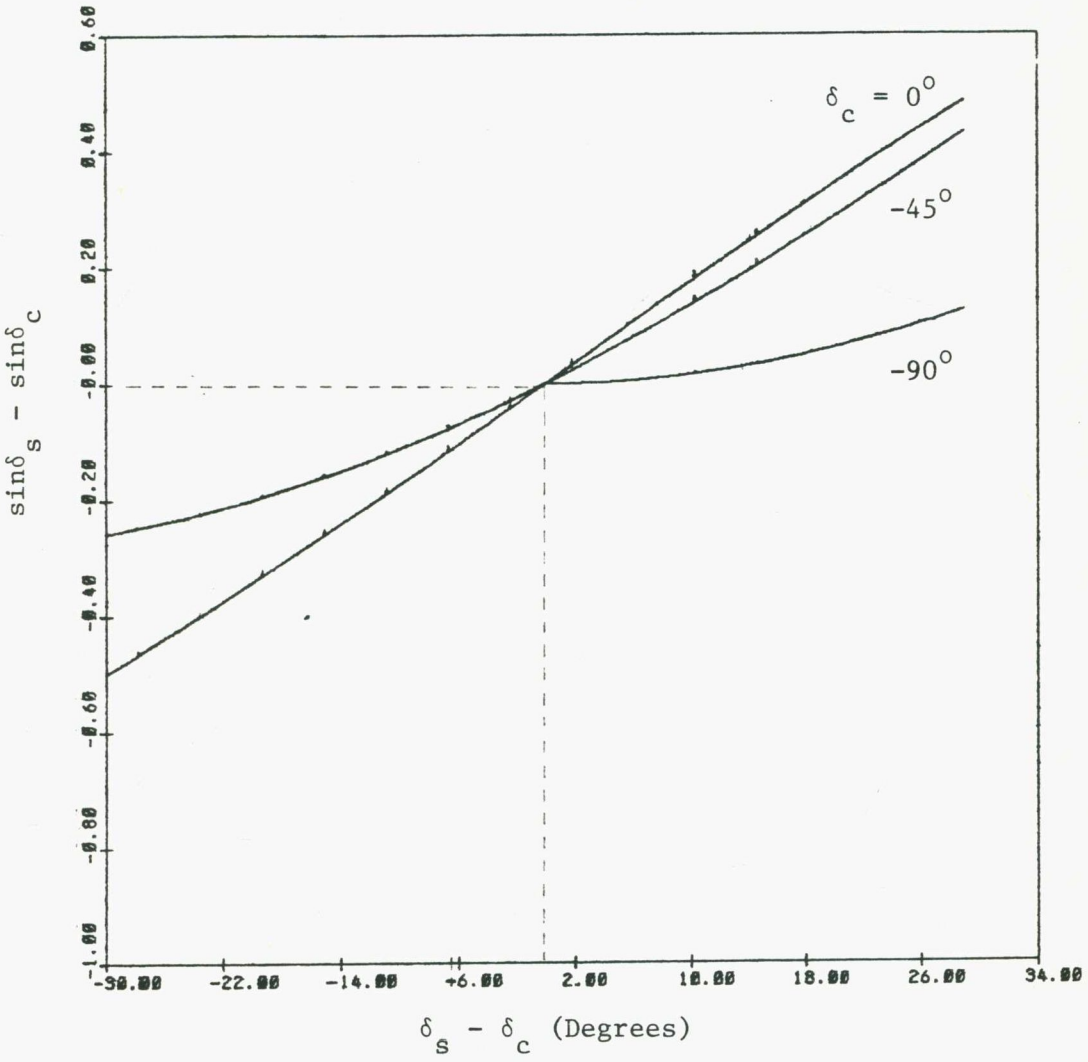

Figure 3-9 Error from an Uncalibrated $\sin(\delta_{\sigma_s})$ Baseline Error Component

when these parameters are used to correct the data obtained at another frequency. The errors can be eliminated by frequency scaling. For a synthesised beam 1.3' wide, the effect of the errors is insignificant.

The baseline parameters possess long term stability. With the FST, they are obtained at the start of each observing session which can last a few months.

The receiver system is calibrated by measuring the gain and phase. The stability of the receiver determines how often this has to be performed. The Fleurs line receiver has two frequency channels, and the total frequency coverage is built up from several local oscillator settings. It is necessary to know the characteristics of the receiver as a function of frequency. As the signal frequency at the IF is fixed, the frequency response is determined by the front end. The constancy of the response depends not only on the stability of the response shape of the amplifiers and multipliers at the front end, but is also affected by any path length difference resulting from unequal cable lengths. The latter effect is to produce a changing phase slope as a function of temperature. Calibration requires that the gain and phase of the receiver be measured at each frequency at which an observation is to be made. The stability of the receiver demands that the calibration observation be performed within a few days of the HI observation. The best result will be obtained by calibrating just before

or after each HI observation. The frequency bandwidth used is normally smaller than the available bandwidth, and it can be expected that the gain response is flat and the phase response possesses a linear slope (Figure 3-10).

A gain and phase calibration usually lasts two hours. The noise level is 0.6 Jy per spacing. When the calibrator has a flux density less than 6 Jy, longer calibration time is required to improve the output S/N.

3.5 Cosine and Sine Gain Imbalance

The synthesised beam is modified by the relative gain between the cosine and the sine channels of a correlator. The aperture distribution is

$$b(\vec{r},\nu) = \int B(\hat{o},\nu)P(\hat{o},\nu)\{\cos(2\pi\nu/c \times \vec{r}\cdot\hat{o}) + j\sin(2\pi\nu/c \times \vec{r}\cdot\hat{o})\}d\hat{o} \qquad (3\text{-}4)$$

When the sine gain is ε times the cosine gain, and there is a phase offset Ψ, the distribution becomes

$$b_{cs}(\vec{r},\nu) = \int B(\hat{o},\nu)P(\hat{o},\nu)\{\cos(2\pi\nu/c \times \vec{r}\cdot\hat{o} + \Psi) + j\varepsilon\sin(2\pi\nu/c \times \vec{r}\cdot\hat{o} + \Psi)\}d\hat{o} \qquad (3\text{-}5)$$

If there are no baseline errors, a calibration in gain and phase gives a correcting factor

$$F_c = \{\cos(\Psi) - j\varepsilon\sin(\Psi)\}/\{\cos^2(\Psi) + \varepsilon^2\sin^2(\Psi)\} \qquad (3\text{-}6)$$

The corrected distribution is

$$b_{csc}(\vec{r},\nu) = b(\vec{r},\nu) + [\![(\varepsilon^2 - 1)\cos(\Psi)\sin(\Psi)/\{\cos^2(\Psi) + \varepsilon^2\sin^2(\Psi)\} + j\{\varepsilon/\{\cos^2(\Psi) + \varepsilon^2\sin^2(\Psi)\} - 1\}]\!] \int B(\hat{o},\nu)P(\hat{o},\nu)\sin(2\pi\nu/c \times \vec{r}\cdot\hat{o})d\hat{o} \qquad (3\text{-}7)$$

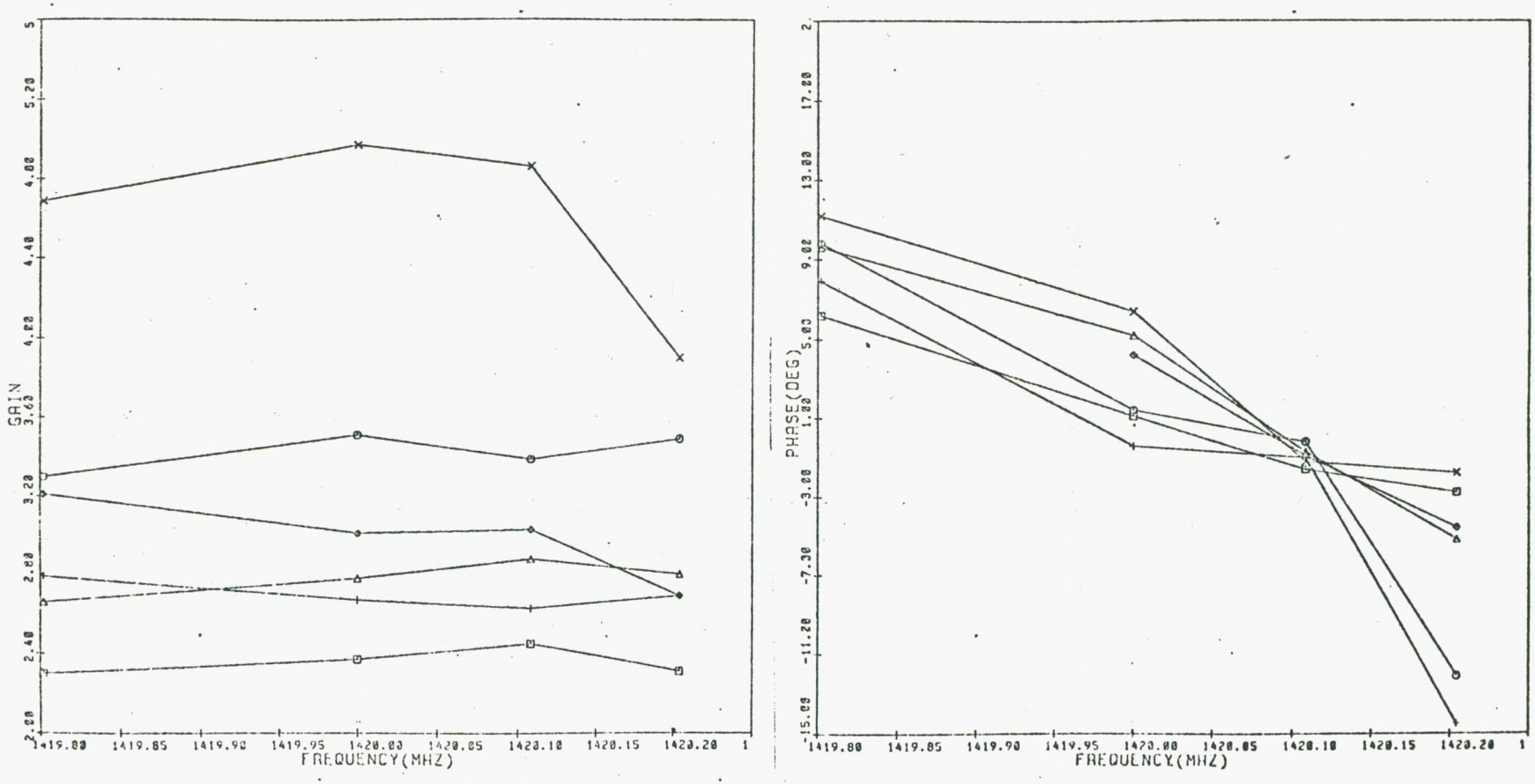

Figure 3-10 Frequency Response of Selected Channels

The data to be transformed consist of the data expected from a perfect instrument and an error. The error vanishes for radiation from the synthesis center.

The effect of the error in the sky domain can be evaluated by considering a point source away from the synthesis center. Besides the true component at $\hat{o}$, two error components are produced at $\hat{o}$ and $-\hat{o}$ (Figure 3-11). The errors have equal and opposite intensities at the two positions. The real part of the square bracketed term in (3-7) produces a sine pattern. The imaginery part of the term produces a cosine pattern. It has been assumed that all data have the same cosine and sine gain imbalance. When ε is random, the effect is less prominent.

In the FST, ε is evaluated by feeding an IF signal through the receiver. Two measurements are taken, one for the IF signal, and the other for the same IF signal with a 90^{o} phase shift. The imbalance can be determined from these two measurements for each spacing.

3.6 Processing in the Map Domain

After Fourier transformation, a set of maps and the associated beam patterns are obtained. In a HI experiment, the channel maps can be regarded as a cubic set with the sky coordinates l, m, and a velocity coordinate v. It is required to extract from this set information about the HI under study.

The map software can be divided into three main groups, enhancement, analysis, and display (Table 3-3).

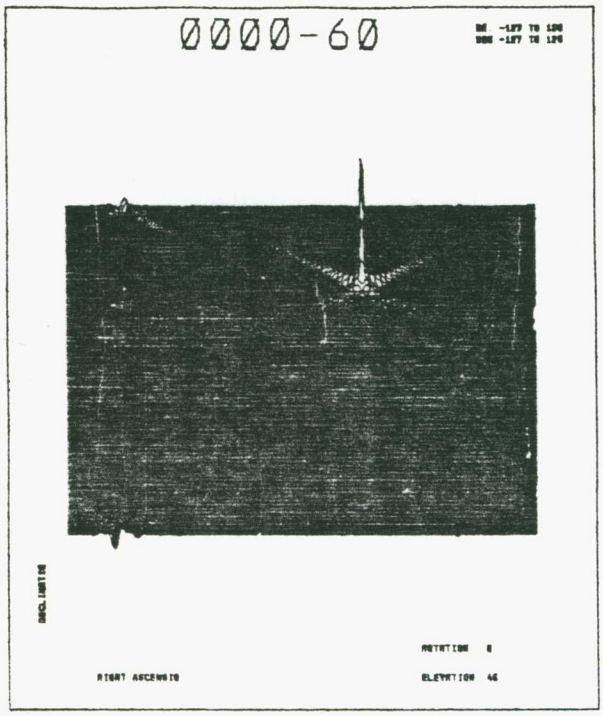

$\varepsilon = 1$

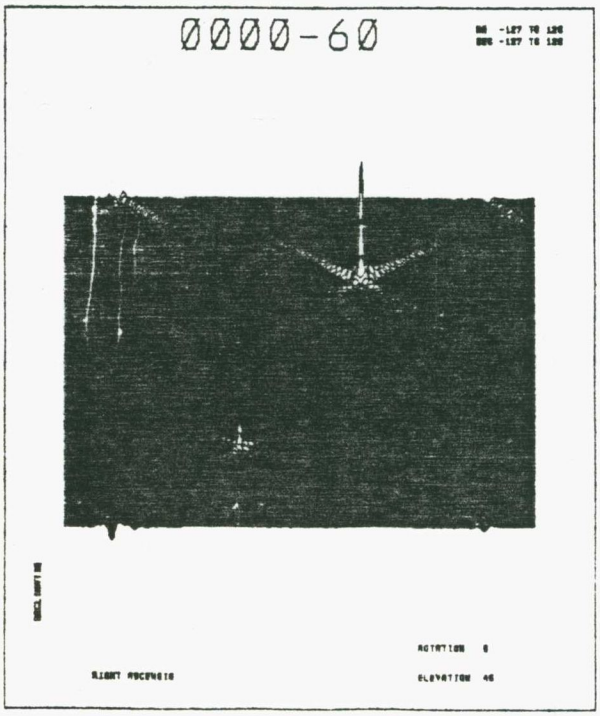

$\varepsilon = 0.5$

$\Psi = -45^{\circ}$

Figure 3-11 Effect of Cosine and Sine Gain Imbalance on the Response of the FST to an Offcenter Point Source

Table 3-3 Map Processing Software

Software	Function	Origin
MFCLN1	Enhancement by CLEAN	Fleurs
CLN	Enhancement by hardware CLEAN	C. F. Chen
VPSMTH	Enhancement of spectrum by smoothing	Author
MFMASK	Reduction of map size	Author
VPMNP	Analysis by the window method	Author
DATMNP	Data overwrite at particular map points	Author
HIDIST	Addition of HI maps to produce a distribution map	Author
VELFLD	Evaluation of the velocity field	Author
MASTAT	Evaluation of map statistics	Author
MFPBC	Correction of the primary beam effect	Author
MFCONT	Plot of map in contours	Fleurs
MFPLOT	Plot of map in 3 dimensional profiles	Fleurs
MAPLOT	Display of map data	L. Simons
IPPLOT	Plot of spectrum	Author

Underlined software resides on PDP11/10
Remaining software resides on PDP11/45

A raw map obtained by aperture synthesis techniques has the information confused by sampling artifacts. There are also systematic errors and noise. Enhancement techniques are used to minimise these effects. Analysis techniques are developed to extract the various forms of information about the HI field from the enhanced maps. Display software is developed to provide visual aids to both the enhancement and analysis processes.

3.7 Map Enhancement

Cutting the data cube along a plane normal to the velocity axis gives a channel map. Various methods have been proposed to enhance the image on these individual cuts. The method used for the Fleurs maps is the procedure CLEAN (Högbom 1974). The method attempts to remove map confusion due to sampling artifacts.

When the information gathered about an object is incomplete, it is possible to estimate the missing information given some a priori knowledge about the object. In radio astronomy, the information came from a region of the sky. Known parameters consist of the position, the boundary, the nature of the radiation (positive for a source or negative for a sink), and the shape of the sampling function (the synthesised beam pattern). The CLEAN process breaks the selected radiation field into a set of point components. The components are obtained through a process of deconvolution using the sampling function. Errors in the sampling function will affect the accuracy of the process.

The characteristics of the measuring instrument need to be known accurately to minimise any errors that may be introduced into the sampling function. To properly remove sampling artifacts on a map, it is necessary to know the sampling function over a region at least twice each linear dimension of the region of interest. The radiation field is reconstructed by reinserting the point components and convolved with a mathematical function with the same central response as the original sampling function but with no sidelobes or grating rings.

Two schemes are available at Fleurs to perform CLEAN. One is by using a standard Fleurs software. The other is by using a hardware orientated CLEAN machine designed by C. F. Chen of this School. Similar principles are used in both schemes but the hardware can perform the operation much faster.

The region to be cleaned is selected to include all HI radiation in the channel maps. It will be assumed that there is no interference from radiation outside the region. If there is, it has to be removed first. The flux is known to be positive and only positive point components are removed from the selected region. When the residue level on the map reaches a level of five times the noise level, noise contribution becomes important and both positive and negative components are removed. The process is stopped when the mean level within the region becomes zero. The criterion of zero mean is chosen from a consideration of a

map with Gaussian noise characteristics. The criterion is affected by systematic errors in the original map and inherent errors in a process with finite accuracy. The cleaned map is reconstructed by using a Gaussian beam pattern having the same half power beamwidths in l and m as the original pattern.

Beam patterns produced by the fast Fourier transform algorithm can possess aliasing at the edge of its field. In this case, the field of the pattern needs to be increased such that any aliasing is always outside the region of the map to be cleaned.

The information content in a cleaned map is different from the information content in the raw map. They are produced by two different beam patterns. When the CLEAN process is complete, a new brightness temperature scale can be defined for the cleaned map. For a Gaussian rebuilt pattern, with half widths of ΔL and ΔM, the solid angle is $1.13\Delta L\Delta M$ (Kraus 1966), and using (1-46) and (1-48),

$$T_B(l,m,\nu) \simeq (c/\nu)^2/(2k \times 1.13\Delta L\Delta M) \times S_a(l,m,\nu)/P_n(l,m,\nu) \qquad (3\text{-}8)$$

A cleaned region normally occupies only a portion of the total map field. When the region surrounding it is of no interest, it can be extracted and put into a smaller file, thus relaxing the storage requirement.

3.8 Spectrum Processing

The set of cleaned maps contains the total flux from a region of the sky. The flux is contributed by two mechanisms. One is spectral line radiation,

and the other is continuum radiation.

Line radiation is limited in frequency width. It exists at a single frequency but spread out by Doppler broadening. Continuum radiation exists over the whole electromagnetic spectrum. Its intensity varies very slowly with frequency. Over the limited frequency range where HI can be detected within a galaxy, it can be regarded as essentially constant with frequency. Making this qualification, methods can be devised to separate the two types of radiation.

One method to separate out the continuum is to study the measured spectrum at each sampled location in the sky. The spectrum contains the HI radiation of interest and a constant level contributed by the continuum. When measurement includes spectral points beyond the range of the line spectrum, the constant can be determined and subtracted, leaving only the HI contribution. An offshoot of this is that errors that are common to all maps will also be subtracted. The errors, however, will appear in the continuum map thus obtained.

The window method (Bosma 1978) is used to separate the HI radiation from the continuum radiation. A run-time printout of the software is shown in Figure 3-12. The software accepts a set of cleaned maps, arranged in sequence as a function of decreasing frequency, or, as is more appropriate in HI studies, arranged in sequence as a function of increasing recession velocity. The outputs are a set of maps which contain only HI radiation,

```
MCR>RUN DK3:VPMNP$
INPUT=DC2:E30HFU.CAC
OUTPUT=DC3:E30HFU.CCC
INPUT=DC2:E30HEU.CAB
OUTPUT=DC3:E30HEU.CCB
INPUT=DC2:E30HDU.CAB
OUTPUT=DC3:E30HDU.CCB
INPUT=DC2:E30HCU.CAC
OUTPUT=DC3:E30HCU.CCC
INPUT=DC2:E30HBU.CAC
OUTPUT=DC3:E30HBU.CCC
INPUT=DC2:E30HAU.CAC
OUTPUT=DC3:E30HAU.CCC
INPUT=DC2:E30HFL.CAC
OUTPUT=DC3:E30HFL.CCC
INPUT=DC2:E30HEL.CAB
OUTPUT=DC3:E30HEL.CCB
INPUT=DC2:E30HDL.CAB
OUTPUT=DC3:E30HDL.CCB
INPUT=DC2:E30HCL.CAC
OUTPUT=DC3:E30HCL.CCC
INPUT=DC2:E30HBL.CAC
OUTPUT=DC3:E30HBL.CCC
INPUT=DC2:E30HAL.CAC
OUTPUT=DC3:E30HAL.CCC
CONTINUUM MAP FILE=DC3:E30C.CCB
WEIGHTS=1,1,1,1,1,1,1,1,1,1,1,1
LEVEL= .1
CUTOFF FACTOR=1
RANGE L=-31,32
RANGE M=-31,32
BASELINE NOT WELL DETERMINED!    L=    8   M=   -2
BASELINE NOT WELL DETERMINED!    L=    5   M=    4
BASELINE NOT WELL DETERMINED!    L=   -4   M=    8
BASELINE NOT WELL DETERMINED!    L=   -4   M=    9
VPMNP  --  STOP
```

Figure 3-12 Spectrum Processing

and a map of the continuum.

The baseline of the spectrum is determined at each map point within a specified region. The windowing process is governed by a convergence level, which can be specified. It is normally taken as the average noise level on the cleaned maps, σ_N. The process starts by calculating the mean value of the points in the spectrum. The maximum of the spectrum is then obtained, and the mean of the remaining points, numbered n_c, is calculated. The baseline is deemed well determined when the absolute change in the mean value is at most σ_N/n_c. If the convergence level is not reached, the window is widened to include the next adjacent highest value of the spectrum. The mean of the points outside the window is again obtained and compared with the previous mean to test for convergence. The process continues until the convergence level is reached. The previously used window contains the HI radiation. The mean of the points outside the window provide an estimate of the continuum. The HI spectrum is obtained by subtracting the continuum from the points inside the window and setting to zero the points outside the window (Figure 3-13).

There are times when the baseline of a spectrum does not converge. They are detected and their location identified. The problematic spectra are plotted and a visual process can be used to extract the baselines. The HI spectra can then be obtained and inserted into the appropriate map locations (Figure 3-14).

To evaluate the performance of the window method,

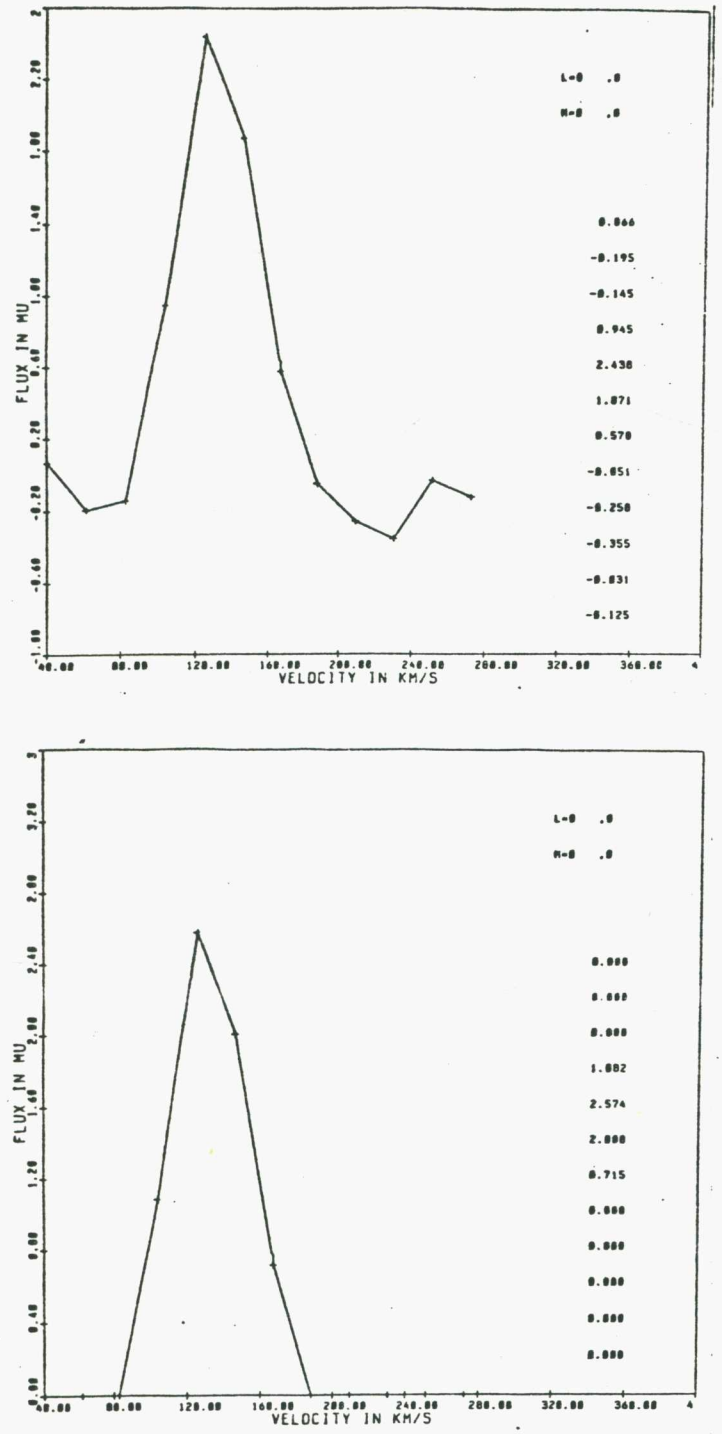

Figure 3-13 . Sample Spectrum Before and After the Windowing Process

```
MCR>RUN DK3:DATMNP↓
# FILES=12
INPUT=DC4:E30HFU.CCC
INPUT=DC4:E30HEU.CCB
INPUT=DC4:E30HDU.CCB
INPUT=DC4:E30HCU.CCC
INPUT=DC4:E30HBU.CCC
INPUT=DC4:E30HAU.CCC
INPUT=DC4:E30HFL.CCC
INPUT=DC4:E30HEL.CCB
INPUT=DC4:E30HDL.CCB
INPUT=DC4:E30HCL.CCC
INPUT=DC4:E30HBL.CCC
INPUT=DC4:E30HAL.CCC
L=8
M=-2
DATA=.442,.598,1.645,.61,.145,0,0,0,0,0,0,0
TYPE 1 TO CONTINUE OR 0 TO STOP:0
DATMNP  --  STOP
```

Figure 3-14 Manual Map Data Overwrite

it is applied to simulated spectra. A spectrum is generated by adding Gaussian noise to an arbitrary spectrum which is known. The noise is derived from a sequence of random numbers with a Gaussian distribution. The numbers are obtained from a uniformly distributed sequence governed by (Digital Equipment Corporation 1975)

$$U_{j+1} = (2^{16} + 3)U_j \bmod(2^{32}) \qquad (3\text{-}9)$$

The Gaussian distributed sequence is then generated as (Zelen and Severo 1965)

$$\begin{aligned} X_j &= \{-2\ln(U_j)\}^{\frac{1}{2}}\cos(2\pi U_{j+1}) \\ X_{j+1} &= \{-2\ln(U_j)\}^{\frac{1}{2}}\sin(2\pi U_{j+1}) \end{aligned} \qquad (3\text{-}10)$$

where j is an odd integer. The numbers have a mean of zero and a variance of unity. The standard deviation, σ_N, is one.

With σ_N as the convergence level, it is found that the original noiseless spectrum cannot be reliably retrieved when the maximum value of the spectrum is below $3\sigma_N$. Under this condition, the process sometimes produce spurious peaks in the spectrum. These effects are minimised by specifying a cutoff level. The present software accepts a cutoff factor, and the cutoff level is determined by multiplying σ_N by the factor. Spectra with S/N less than the cutoff level is supressed.

The windowing process is governed by σ_N. This is obtained by calculating the standard deviation of a background map from which all radiation has been cleaned out. The accuracy that can be expected depends on the number of points included in the statistical calculation (Figure 3-15). The accuracy is also dependent

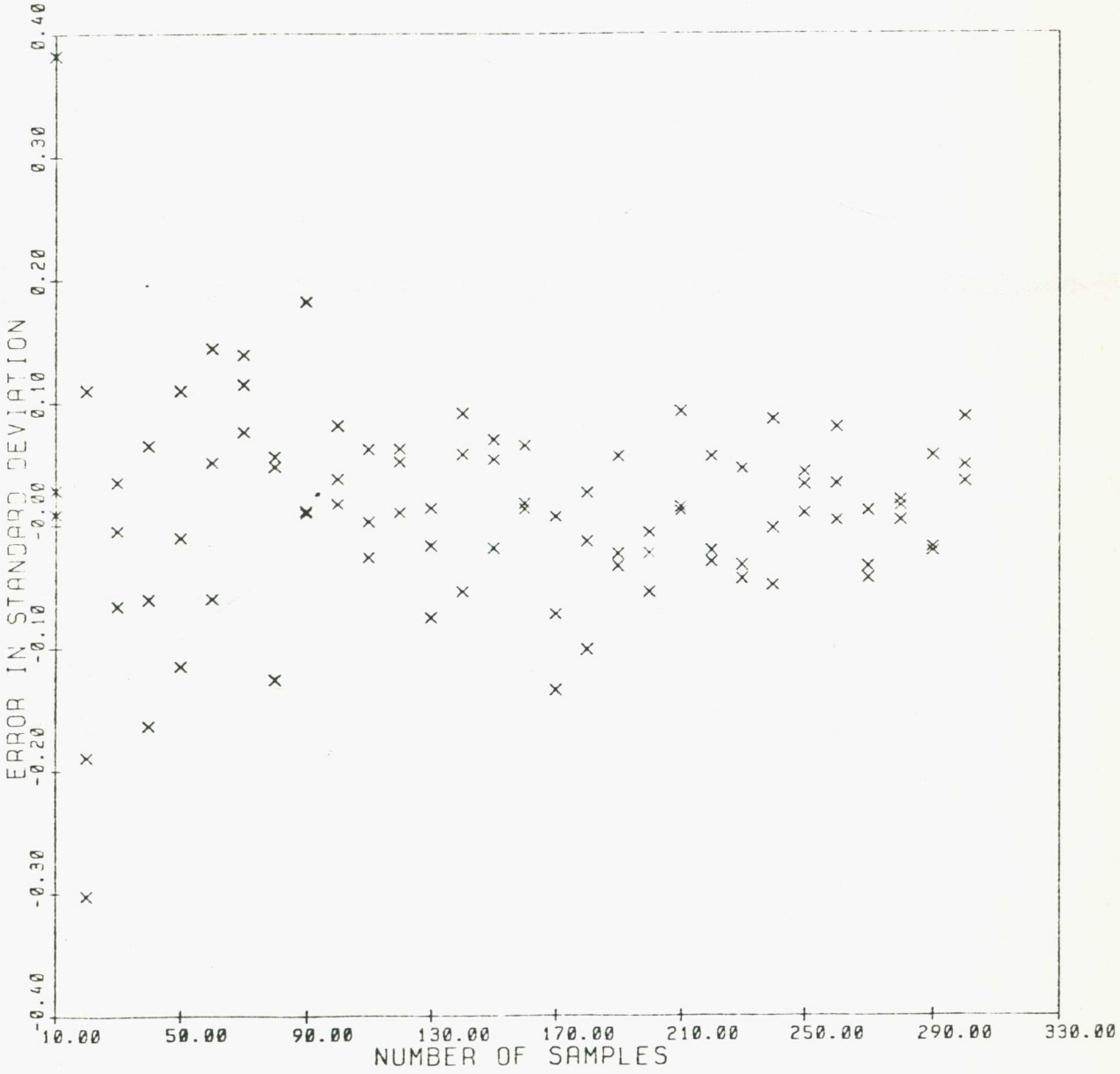

Figure 3-15 Effect of Sample Numbers on the Spread in Standard Deviation (Noise)

upon the amount of uncleaned residue radiation that still exists on the background map. Furthermore, maps produced by the fast Fourier transform have a non-uniform noise distribution. The noise level is higher at the edge of a map. The significance of this diminishes if the region under study is concentrated around the synthesis center. An overestimate of 30% in noise will cause some suppression of signal at the $3\sigma_N$ level.

The windowing process results in partial suppression of the low level signal. Where a reduction in velocity resolution can be tolerated, the S/N of the spectrum can be improved by smoothing. The result of a $\frac{1}{2}$-$\frac{1}{4}$-$\frac{1}{2}$ running sum smoothing of a spectrum is shown in Figure 3-16.

The spectrum processing software is seen to extract HI information from a background of continuum and noise. The task is achieved by substracting the continuum and optimising the bandwidth at each map point. By optimising the bandwidth, there is a S/N improvement on information derived from a combination of the HI maps. However, since the spectrum width varies over the map, the S/N varies accordingly.

The brightness temperature on the continuum map is

$$T_{Bc}(\hat{o}) = \sum_{i \varepsilon n_c} T_{B_{oi}}(\hat{o})/n_c \qquad (3\text{-}11)$$

The standard error is (Figure 3-17),

$$\sigma_c = \sigma_N/\sqrt{n_c} \qquad (3\text{-}12)$$

The narrower a particular spectrum, the better the continuum can be determined at that map point.

The brightness temperature on a HI map is

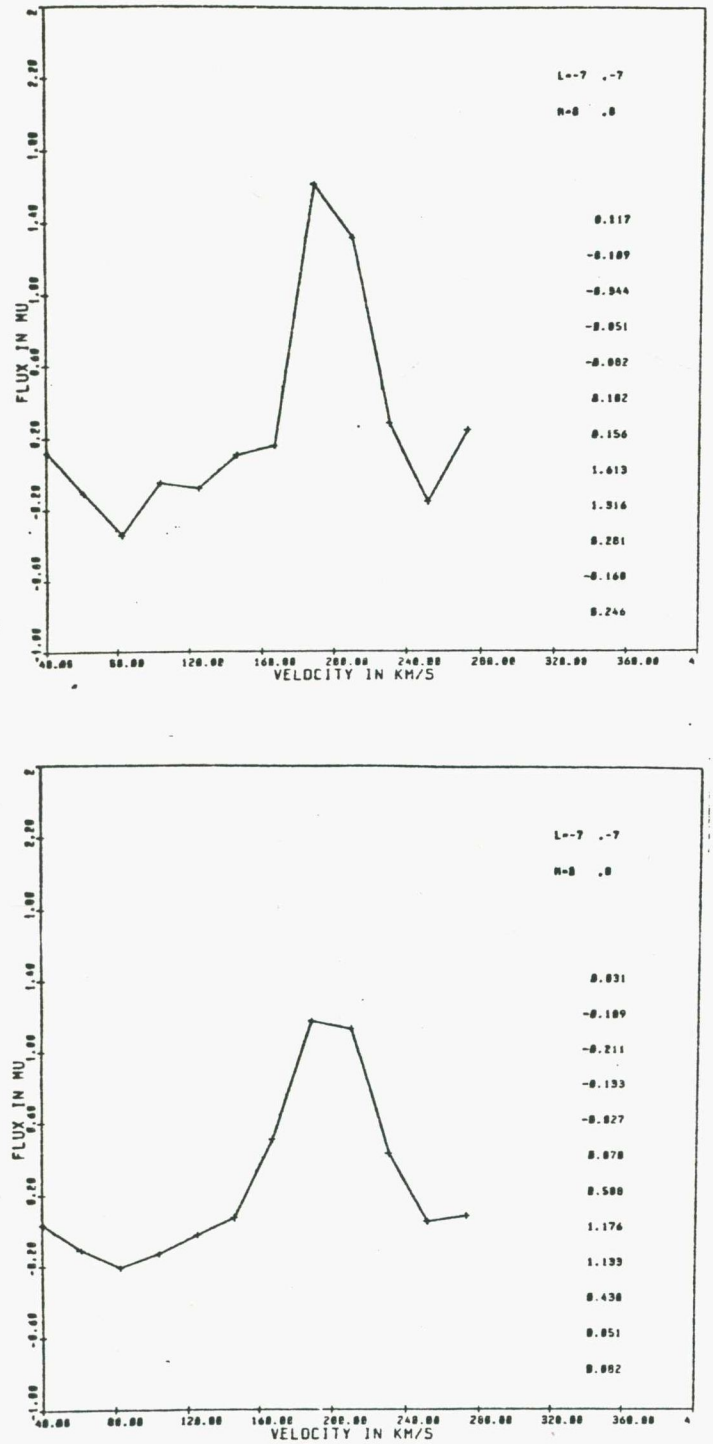

Figure 3-16 Sample Spectrum Before and After Smoothing

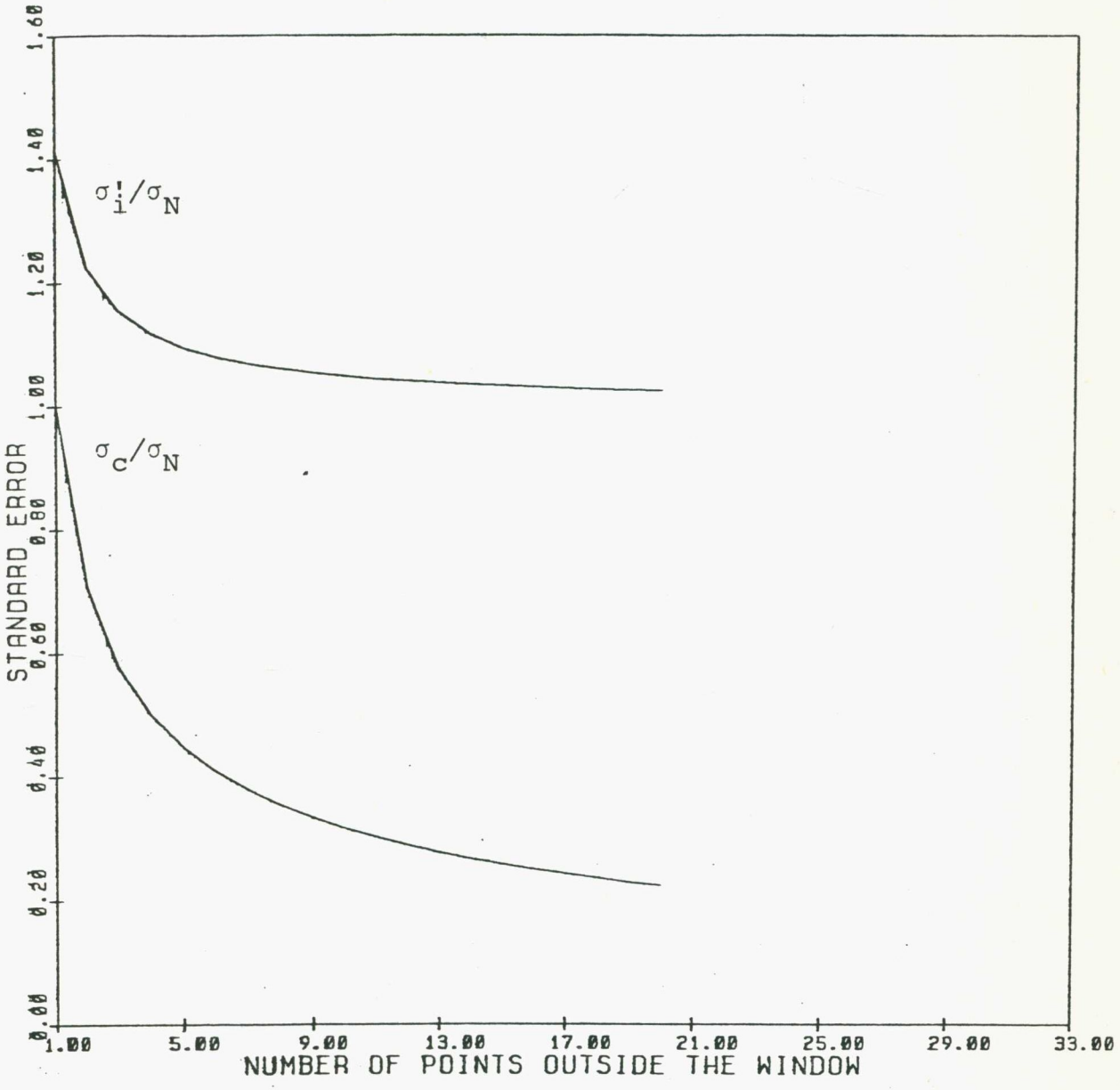

Figure 3-17 Normalised Noise Level on the Continuum and HI Maps Produced by the Window Method

$$T'_{B_i}(\hat{\sigma}) = T_{B_{oi}}(\hat{\sigma}) - T_{Bc}(\hat{\sigma}) \qquad (3\text{-}13)$$

The standard error is (Figure 3-17),

$$\sigma'_i = (1 + 1/n_c)^{\frac{1}{2}}\sigma_N \qquad (3\text{-}14)$$

A narrow spectrum is better determined than a wide spectrum. The noise level on the HI map is higher than the noise level on the original map. It approaches σ_N when n_c becomes large, in other words, making the measurement window larger than the spectrum width. The increase in noise can be limited to below 10% by making $n_c \geq 5$.

3.9 Distribution of Neutral Hydrogen

The HI distribution can be estimated from the first equation in (2-38). It is obtained by combining appropriately weighted HI maps. A run-time printout of the software is shown in Figure 3-18.

The software accepts the set of HI maps. The user can specify individual weights for the maps and a common weight for all maps. The weighted maps are added together to produce the HI distribution map which is stored.

The integrated brightness temperature is

$$\overline{T}'_{Bint}(\hat{\sigma}) = w_0 \sum_{i\varepsilon n_1} c_i T'_{B_i}(\hat{\sigma})\Delta_v \qquad (3\text{-}15)$$

where n_1 consists of the points on the spectrum with HI radiation. The noise on $T'_{B_i}(\hat{\sigma})$ consists of noise due to $T_{B_{oi}}(\hat{\sigma})$ (uncorrelated between maps) and noise due to $T_{Bc}(\hat{\sigma})$ (correlated between maps). Equation (3-15) can be rewritten as

$$\overline{T}'_{Bint}(\hat{\sigma}) = w_0\{\sum_{i\varepsilon n_1} c_i T_{B_{oi}}(\hat{\sigma}) - (\sum_{i\varepsilon n_1} c_i)T_{Bc}(\hat{\sigma})\}\Delta_v \qquad (3\text{-}16)$$

The standard error is,

```
MCR>RUN DK3:HIDIST$
NUMBER OF INPUTS=12
INPUT=DC2:C30HFU.PGA
INPUT=DC2:C30HEU.PGA
INPUT=DC2:C30HDU.PGA
INPUT=DC2:C30HCU.PGA
INPUT=DC2:C30HBU.PGA
INPUT=DC2:C30HAU.PGA
INPUT=DC2:C30HFL.PGA
INPUT=DC2:C30HEL.PGA
INPUT=DC2:C30HDL.PGA
INPUT=DC2:C30HCL.PGA
INPUT=DC2:C30HBL.PGA
INPUT=DC2:C30HAL.PGA
OUTPUT=DK2:C30HID.PGA
WEIGHTS=1.45,1.03,1.02,1,1..99,.99,1,1,.02,1.03,1.45
SCALE=1.00
HIDIST  --  STOP
```

Figure 3-18 Addition of Maps

$$\sigma'_{int} = w_0\{\sum_{i\varepsilon n_1} c_i^2 + (\sum_{i\varepsilon n_1} c_i)^2/n_c\}^{\frac{1}{2}}\Delta_v\sigma_N \qquad (3\text{-}17)$$

When $w_0 = c_i = 1$, the equation simplifies to (Figure 3-19)

$$\sigma'_{int} = \{n_1(1 + n_1/n_c)\}^{\frac{1}{2}}\Delta_v\sigma_N \qquad (3\text{-}18)$$

The S/N will be high when all the HI flux is within a small velocity range.

3.10 Velocity Field

The average velocity field over a galaxy is estimated from the second equation in (2-38). A run-time printout of the software is shown in Figure 3-20.

The software accepts the set of HI maps, the distribution map, and the appropriate weights. The user also specifies the lowest velocity encountered in the HI maps. The software assumes a velocity spacing of 21.1 km/s, as is pertinent for the Fleurs HI receiver.

The velocity field is

$$\overline{V}'(\hat{o}) = w_1 \sum_{i\varepsilon n_1} v_i c_i T'_{B_i}(\hat{o})\Delta_v/\overline{T}'_{Bint}(\hat{o}) \qquad (3\text{-}19)$$

The standard error is

$$\sigma'_v = \{\sum_{i\varepsilon n_1} (w_1 v_i - w_0\overline{V}'(\hat{o}))^2 c_i^2 + (w_1 \sum_{i\varepsilon n_1} v_i c_i - w_0\overline{V}'(\hat{o}) \sum_{i\varepsilon n_1} c_i)^2/n_c\}^{\frac{1}{2}}\Delta_v/\overline{T}'_{Bint}(\hat{o}) \times \sigma_N \qquad (3\text{-}20)$$

The noise on the estimated velocity is small if the signal is strong and n_c is large.

3.11 Primary Beam Correction

The primary beam of a synthesis telescope modifies the actual brightness distribution over a region of the sky. A map produced from corrected measurements represent $B(\hat{o})P_n(\hat{o})$. Multiplication by $1/P_n(\hat{o})$ then corrects the primary beam effect.

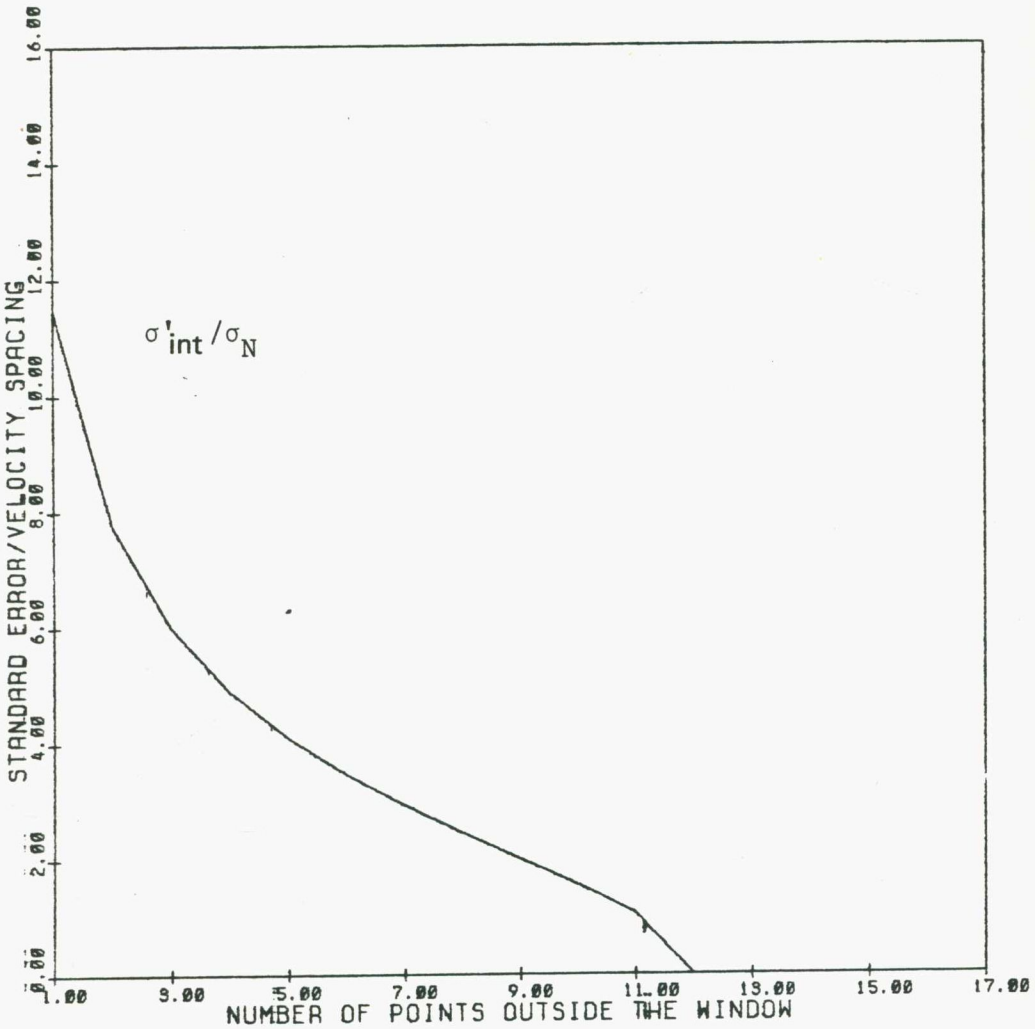

Figure 3-19 Noise on a Integrated Map

```
RUN DK3:VELFLD$
NUMBER OF INPUTS=12
INPUT=DC4:C30HFU.PGA
INPUT=DC4:C30HEU.PGA
INPUT=DC4:C30HDU.PGA
INPUT=DC4:C30HCU.PGA
INPUT=DC4:C30HBU.PGA
INPUT=DC4:C30HAU.PGA
INPUT=DC4:C30HFL.PGA
INPUT=DC4:C30HEL.PGA
INPUT=DC4:C30HDL.PGA
INPUT=DC4:C30HCL.PGA
INPUT=DC4:C30HBL.PGA
INPUT=DC4:C30HAL.PGA
HI DISTRIBUTION MAP FILE=DC4:C30HID.PGA
VELOCITY FIELD FILE=DK2:C30HIV.PGA
WEIGHTS=1.45,1.03,1.02,1,1,.99,.99,1,1,1.02,1.03,1.45
LOWEST VELOCITY IN KM/S= 40.5
SCALE= 1.17
VELFLD  --  STOP
```

Figure 3-20 Estimation of the Velocity Field

The correction for the FST primary beam as given by D. S. Retallack (1978) is (Figure 3-21)

$$P_n^{-1}(\alpha,\delta) = \exp\{(\alpha - \alpha_{\sigma_o})^2\cos^2(\delta)/0.697 + (\delta - \delta_{\sigma_o})^2/0.555\} \quad (3\text{-}21)$$

The correction factor is valid within 0.6^o from the synthesis center. The required correction is less than 10% within 13' of the center.

A run-time printout of the software is shown in Figure 3-22. The corrected map is identified by a bit in its header to prevent inadvertent multiple corrections.

3.12 Map Display

Maps in a HI experiment occupies a three dimensional space. Two displays are implemented. One displays the map variation in l and m. One displays the spectrum in v.

Standard Fleurs software is available for map display. Hard copies of the maps can be obtained. A visual display has recently been developed by C. F. Chen of this School.

Two programs residing on the PDP11/10 contour plots and 3 dimensional profile plots of maps on an INFOMAX electrostatic plotter. Quality plots are produced on a Gould electrostatic plotter, driven by the PDP11/45. The software, MAPLOT, was originally implemented by L. Simons in 1977. Since then, it has been debugged and modified by the author. The software can produce contour plots and 3 dimensional profile plots. It can also produce the profile of a cut across a part of a

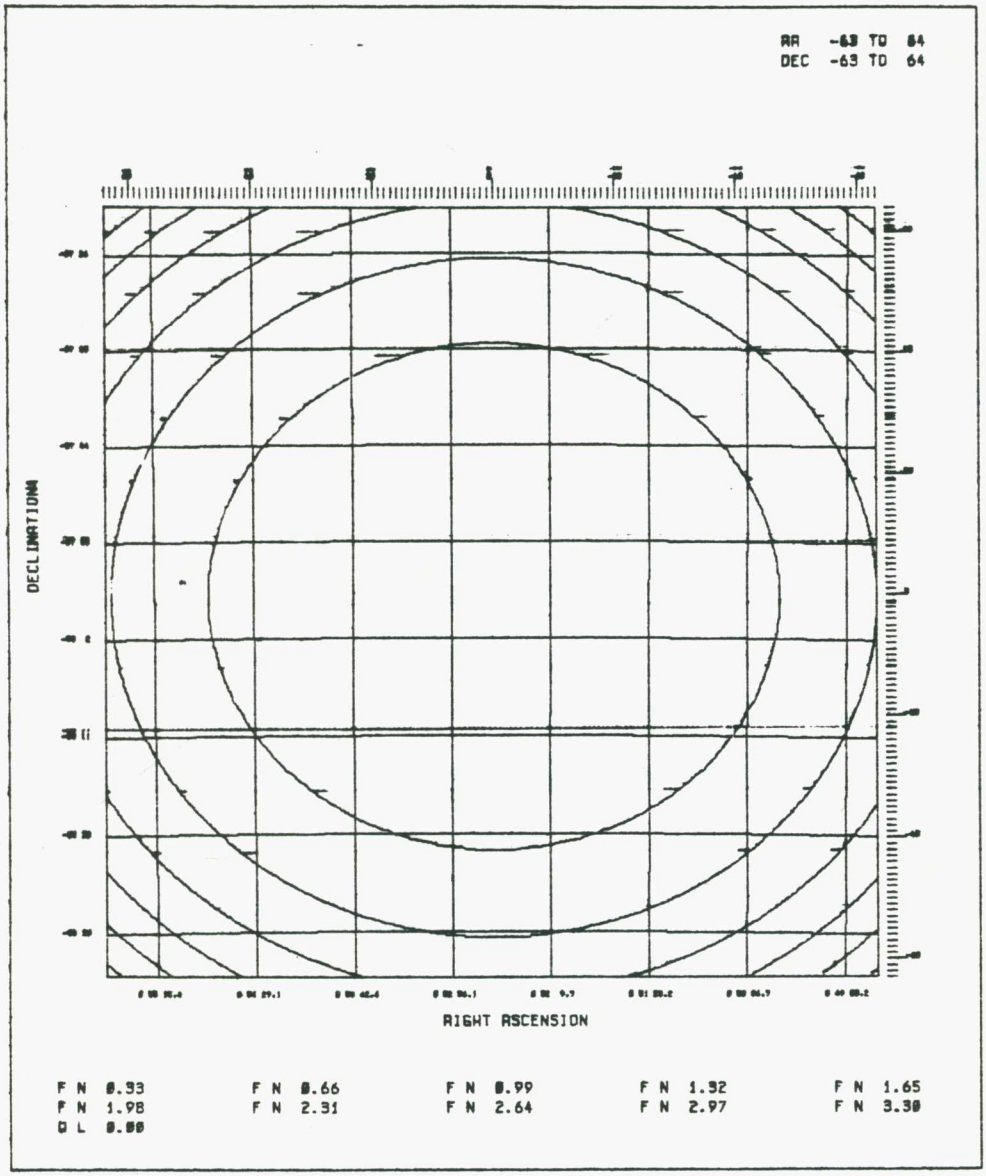

Figure 3-21 Primary Beam Correction Pattern

```
 RU MFPBC

PRINT ON: #



PRIMARY BEAM PATTERN CORRECTION      29-DEC-80  20:43:38

LOAD: #DK:E30HEU.UNI
MAP:       NSC 300


MAX/MIN= Y

MAXIMUM:     1.00  AT (L,M): -127,-127
MINIMUM:     1.00  AT (L,M): -127,-127

MAX/MIN=
```

maximum and minimum intensities on the corrected map

```
DESCR.= 
```

description of map

```
_IBT=

STORE: #DK:E30HEU.PBC


END      29-DEC-80  21:48:27
```

Figure 3-22 Primary Beam Correction of a Map

4

map.

A run-time printout of the software which displays the spectrum is shown in Figure 3-23. The software accepts the lowest velocity encountered, the set of HI maps, and appropriate weights. The velocity spacing is set at 21.1 km/s. The display can be either the spectrum at a single map point (spectrum at a particular l and m), or an integrated spectrum (spectrum over a specified map region). The display also includes the values of the individual points on the spectrum. This is especially useful when a manual analysis of a spectrum is warranted.

3.13 References

Bosma, A. "The Distribution and Kinematics of Neutral Hydrogen in Spiral Galaxies of Various Morphological Types". Ph. D. Thesis, The University of Groningen, 1978.

Brouw, W. N. "Data Processing for the Westerbork Synthesis Radio Telescope". Ph. D. Thesis, The University of Leiden, 1971.

Christiansen, W. N. "The Fleurs Synthesis Telescope", Proc. IREE, vol. 34, 302-308, 1973.

Digital Equipment Corporation. "Fortran IV-Plus User's Guide". 1975.

Frater, R. H. and D. J. Skellern. "Direct Transform Hardware Processing of Rotational Synthesis Data - I", Astron. & Astrophs., vol. 68, 391-396, 1978.

Högbom, J. A. "Aperture Synthesis with a Non-regular Distribution of Interferometer Baselines", Astron. & Astrophs., suppl. 15, 417-426, 1974.

Kraus, J. D. "Radio Astronomy". McGraw-Hill Book Company, 1966.

O'Sullivan, J. D. and W. N. Brouw. "Phase and Gain Calibration of the FST", Proc. IREE, vol. 34, 347-352, 1973.

Retallack, D. S. Unpublished Work. 1978.

```
    RUN DK3:[PPLOT]$
LOWEST VELOCITY IN KM/S= 40.5
INPUT=DC4:C30HFU.PGA
INPUT=DC4:C30HEU.PGA
INPUT=DC4:C30HDU.PGA
INPUT=DC4:C30HCU.PGA
INPUT=DC4:C30HBU.PGA
INPUT=DC4:C30HAU.PGA
INPUT=DC4:C30HFL.PGA
INPUT=DC4:C30HEL.PGA
INPUT=DC4:C30HDL.PGA
INPUT=DC4:C30HCL.PGA
INPUT=DC4:C30HBL.PGA
INPUT=DC4:C30HAL.PGA
WEIGHTS=1,1,1,1,1,1,1,1,1,1,1,1
SCALE=1
RANGE L=-4,-4
RANGE M=17,17
TYPE 1 TO CONTINUE OR 0 TO STOP:1
RANGE L=-4,14
RANGE M=7,17
TYPE 1 TO CONTINUE OR 0 TO STOP:0
IPPLOT  --  STOP
```

Figure 3-23 Plot of Spectra

Zelen, M. and N. C. Severo. "Probability Functions", Handbook of Mathematical Functions, M. Abramowitz and I. A. Stegun, ed. U. S. Government Printing Office, 1965.

CHAPTER IV NEUTRAL HYDROGEN STUDY OF THE GALAXY N300

4.1 Radiation of Neutral Hydrogen

For almost two decades since Jansky, radio astronomers measured the continuum radiation from the sky. It was realised that important information would be obtained if a radio counterpart of the optical spectral line could be measured. In 1945, H. C. van de Hulst of the Leiden Observatory made the necessary calculations and suggested that a search be made of the neutral hydrogen line at around 1420 MHz. The line was detected in 1951 by different investigators at Harvard, Leiden, and Sydney.

The neutral hydrogen atom can undergo a hyperfine transition at its ground state (Figure 4-1). The energy gap between the two levels is 5.9 μeV. The upper level, 1, has the magnetic dipole moments, or spins, of the electron and the proton in parallel. The level splits into a triplet under the influence of a magnetic field. The lower level, 0, has the respective spins antiparallel. The transition frequency has been measured accurately in the laboratory to be 1420.405752 MHz (Kerr 1968).

The intensity of the transition depends on the relative population of the two levels, as governed by the Boltzmann equation,

$$n_1/n_0 = g_1/g_0 \times e^{-h\nu/(kT_S)} \qquad (4\text{-}1)$$

where the g's are the statistical weights and h is Planck's constant. For the hyperfine transition, g_1/g_0 is three. The spin temperature, T_S, can be seen as a measure of the relative population of the two levels.

To interprete the observational data, it is

Principal Quantum Number = 1

Orbital Angular Momentum Quantum Number = 0

In a magnetic field, the higher sublevel splits into a triplet, corresponding to magnetic quantum numbers 1, 0, and -1.

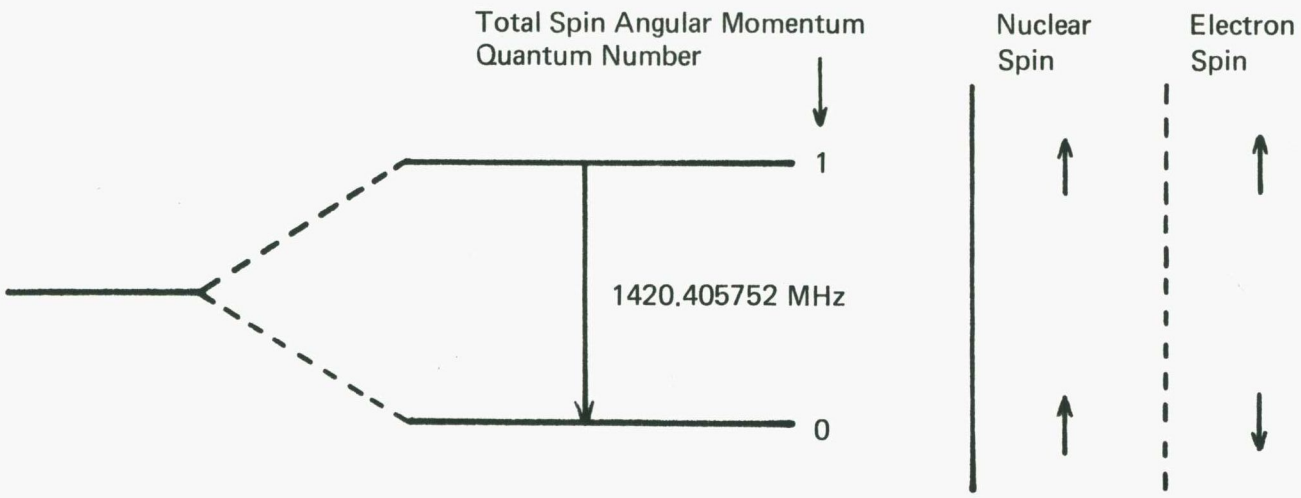

Figure 4-1 Radiation Mechanism of Neutral Hydrogen

necessary to know what is being measured. In an observational system, there is the source, the transmission medium, and the receiver. The source radiates at T_o, and the radiation travels through the medium to arrive at the receiver as T_B. When the medium (HI) is at T_S and is characterised by an absorption coefficient K, the equation of radiative transfer gives

$$dT_B/dR = K(-T_B + T_S) \qquad (4\text{-}2)$$

where R is the distance measure along the line joining the source and the receiver. This is a Leibnitz equation and has a solution

$$T_B = T_o e^{-\tau_m} + e^{-\tau_m} \int T_S e^{\tau_m} dR \qquad (4\text{-}3)$$

where $\tau_m = \int K dR$ is the optical depth of the medium. In the simple case where T_S is constant along R, the Fredhelm's integral equation can be evaluated to give

$$T_B = T_o e^{-\tau_m} + T_S(1 - e^{-\tau_m}) \qquad (4\text{-}4)$$

The unknowns are T_o, T_S, and τ_m. A problem in radio astronomy is to separate the three quantities.

Unless τ_m is known, experiments measuring HI emission normally assumes the HI to be optically thin ($\tau_m << 1$), and

$$T_B \simeq T_o + \tau_m T_S \qquad (4\text{-}5)$$

The first term is a constant and can be extracted leaving

$$T_B \simeq \tau_m T_S \qquad (4\text{-}6)$$

The equation gives the radiation contribution from HI. The radiation is velocity dependent due to τ_m. The optical depth for HI is (Spitzer 1968)

$$\tau_m(v) \simeq c^3/(32\pi\nu^2) \times h/(kT_S) \times g_1/g_0 \times A_{10} N_t P(v) \qquad (4\text{-}7)$$

where $A_{10} = 2.868(10)^{-15}$ /s is the HI coefficient of downward spontaneous emission, N_t is the HI column density, and P(v) is the probability function of the HI distribution in velocity.

Combining (4-6) and (4-7), and integrating over v (km/s) at each point in the map, the HI column density distribution (atoms/cm^2) is found to be

$$N_t(\hat{o}) \simeq 1.823(10)^{18} \int T_B(\hat{o},v)dv \qquad (4\text{-}8)$$

The HI mass surface density distribution (kg/cm^2) is obtained by multiplying (4-8) by the atomic mass of hydrogen,

$$\sigma_{M_H}(\hat{o}) \simeq 3(10)^{-9} \int T_B(\hat{o},v)dv \qquad (4\text{-}9)$$

The HI mass (solar units) over an area is

$$M_H \simeq 1.43(10)^{10} R^2 \int\int T_B(\hat{o},v)d\hat{o}dv \qquad (4\text{-}10)$$

R (Mpc) being the distance of the HI from the telescope.

4.2 Neutral Hydrogen Study of N300

The Fleurs HI receiver was used to map N300, a galaxy in the Sculptor group. The galaxy is spiral of type Sc and has a Holmberg size of 27' × 21'. Integrated spectra have been obtained by Epstein (1964), and Whiteoak and Gardner (1977). Shobbrook and Robinson (1967) have mapped the HI with a 13.5' beam. They derived a systemic heliocentric velocity of 145 km/s. Recently, Rogstad, Crutcher, and Chu (1979) have obtained a HI map of the galaxy by aperture synthesis with a 2' × 3' (EW × NS) beam.

The galaxy has a high HI brightness and was chosen for an initial observation with the new Fleurs instrument. The angular resolution achieved was 1.3' × 3.1',

resulting in a galaxy to beam size ratio of about 15. The adopted distance of the galaxy is 2.5 Mpc, giving a linear scale of around 730 pc to 1'. Table 4-1 gives the main optical parameters of the galaxy.

The galaxy was observed with both the EW array and the NS array of the FST. The generally low visibility accentuates some interference problems in the telescope (to be discussed in Chapter V). This is especially true for the NS observations. The following analysis was based on the EW data. The resulting gap in the synthesised aperture means that features aligned in the right ascension direction will not be properly measured. Six local oscillator settings were used giving 12 channel maps ranging from 40.5 km/s to 272.6 km/s in steps of 21.2 km/s. The velocity is heliocentric. The EW observations were performed in September 1979.

4.3 System Performance

The performance of the Fleurs HI receiver is evaluated by the observation of an unresolved source, 0521-36. Its 1950 position is $\alpha = 5^h\ 21^m\ 12.95^s$ and $\delta = -36^\circ\ 30'\ 16''$. The 21 cm radio size is $16'' \times <28''$ (Frater et al. 1976). The source was observed over 8 hours by the EW array. The position of the source was the synthesis center. The noise level was 98 mJy.

It is generally noted from the data that the amplitude of the measurements changes at transit (Figure 4-2). The change can be as large as 30% as borne out by correlator channel number 10. There is, on the average, a drop in amplitude after transit. In the map domain,

Table 4-1 Adopted Parameters of N300

Type	Sc	
Position (1950)	$\alpha = 52^m\ 36^s$	$\delta = -37°\ 58'$
Distance	2.5 Mpc	
Holmberg size	27' x 21'	
Luminosity	3.6×10^9 solar units	
Major-axis position angle	109°	
Inclination	42.5°	

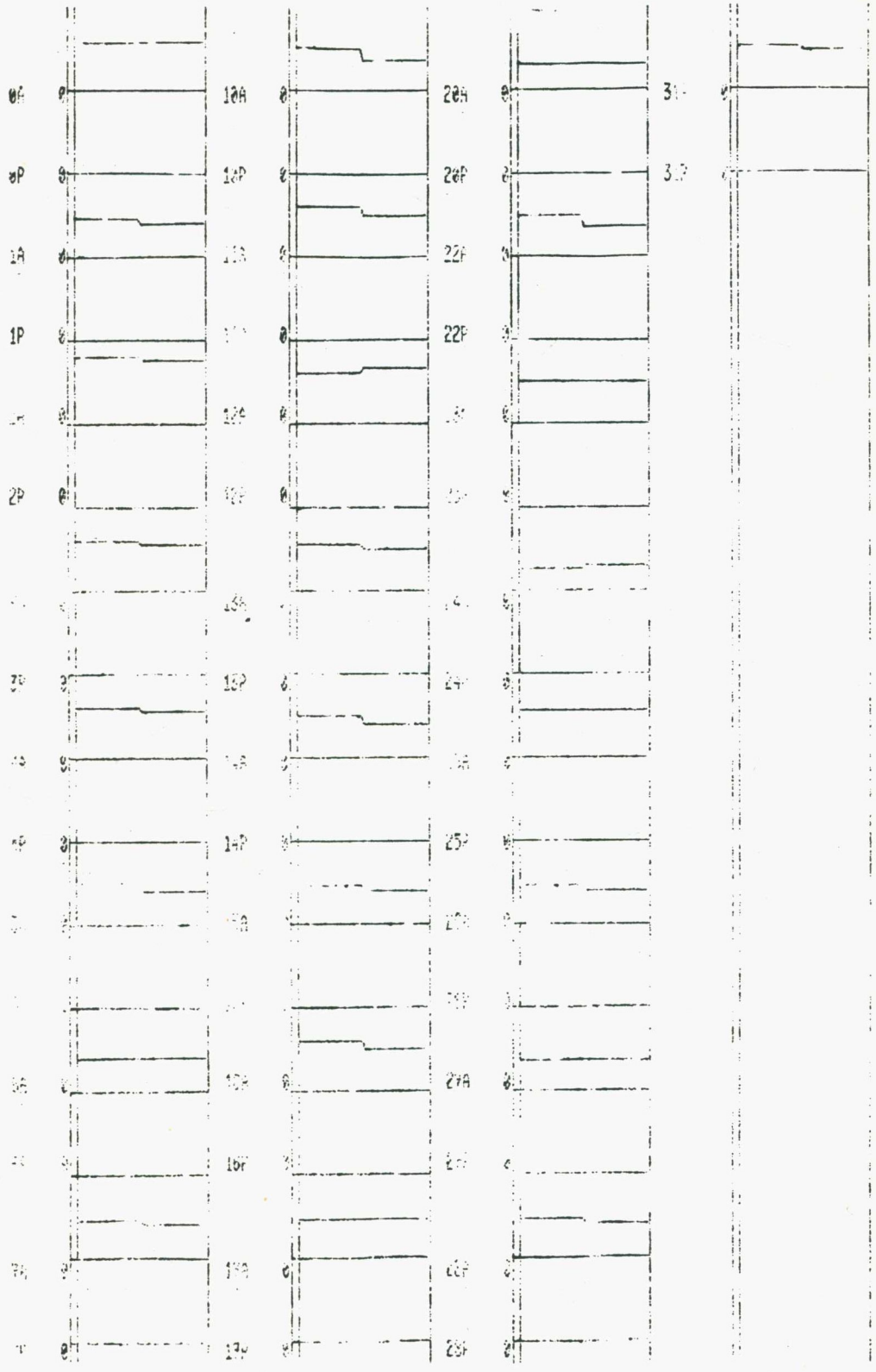

Figure 4-2 Plot of Data Showing the Change in Amplitude at Transit

the effect transforms to a beam with a higher gain towards the southwest (SW) and northeast (NE) quarters (Figure 4-3). The error is less than 7%. The error can be eliminated by breaking the measurement into before and after transit segments. The segments are individually amplitude calibrated. The two segment maps are then combined. The residue map shows improvement over the untreated case (Figure 4-3).

As discussed in 2.11, imperfect delay tracking produces an error beam. At the declination of 0521-36, the first order spurious responses are expected to occur along the m axis at $\pm 1.47^{\circ}$ from the synthesis center. The responses can be located on the $3.6^{\circ} \times 3.6^{\circ}$ map (Figure 4-4). They are odd in l, suggesting a main contribution from the measurement being amplitude modulated. The peak spurious intensity is less that 6% of the main response. The spurious response proper has minimal effect on a source within the Fleurs field of view of $1.2^{\circ} \times 1.2^{\circ}$. However, the associated first grating ring is troublesome for extended sources larger than $30' \times 30'$.

4.4 Calibration

Two calibrators were used for the observation of N300. They were 0521-36 and 1934-63. The calibrator 0521-36 has a favourable declination, differing from that of N300 by 1.4°. Its flux density is 17.5 Jy. A good baseline calibration can be achieved without having to observe a series of calibrators at different declinations. The calibrator was observed over a period

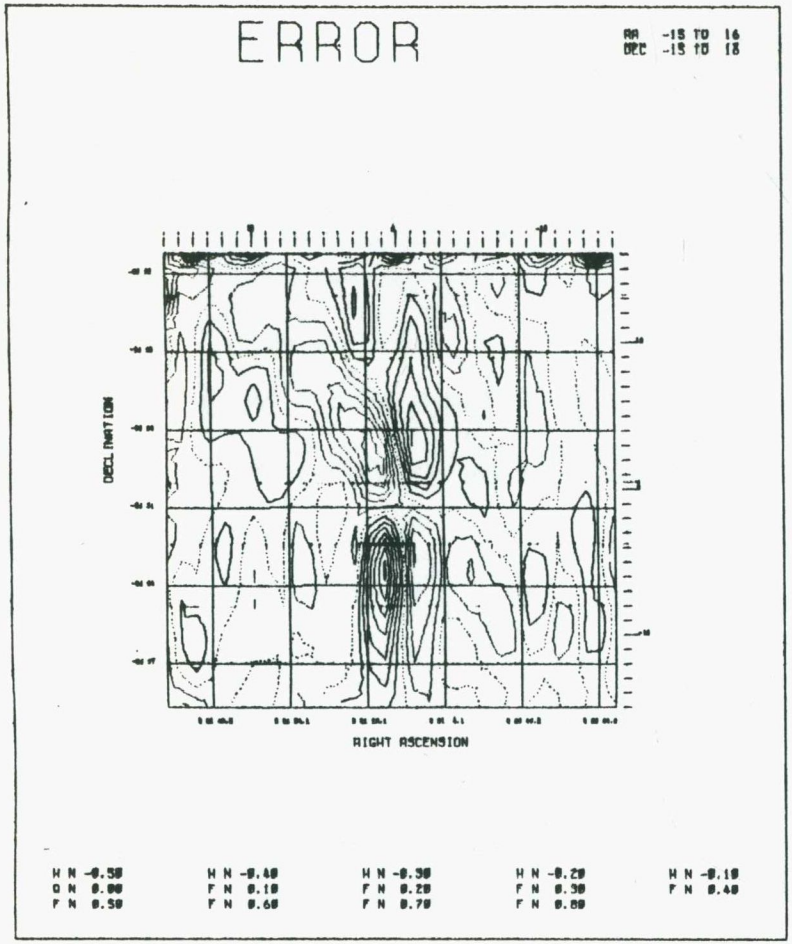

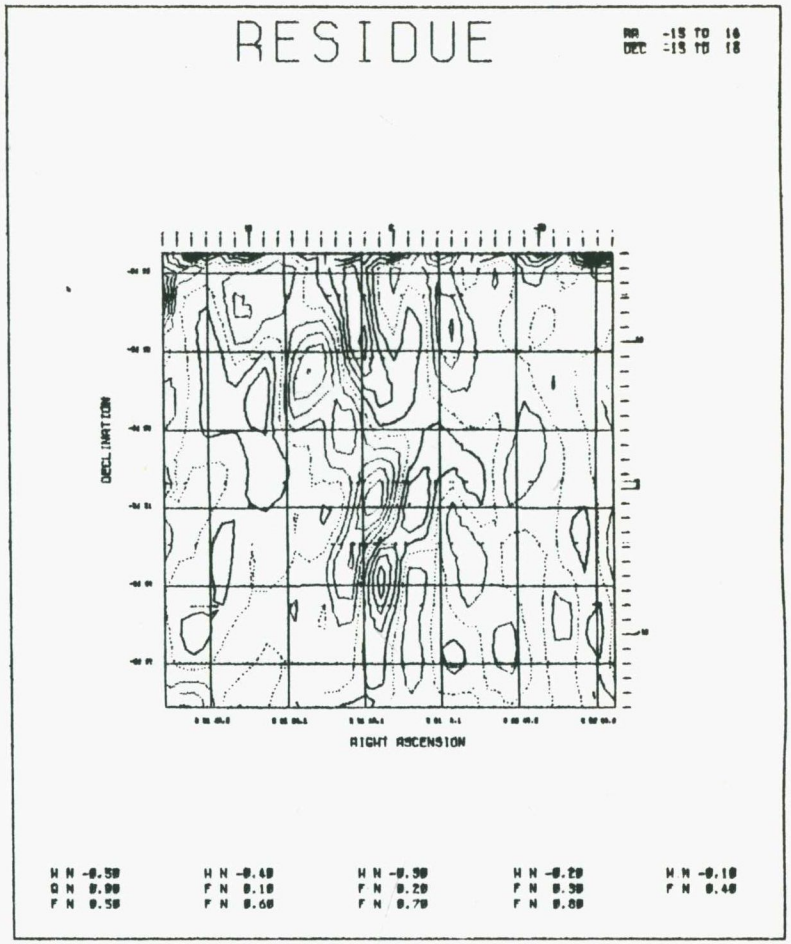

Figure 4-3 Map Response After Subtraction of the Point Source at the Synthesis Center

Sighting
Angle = 45°

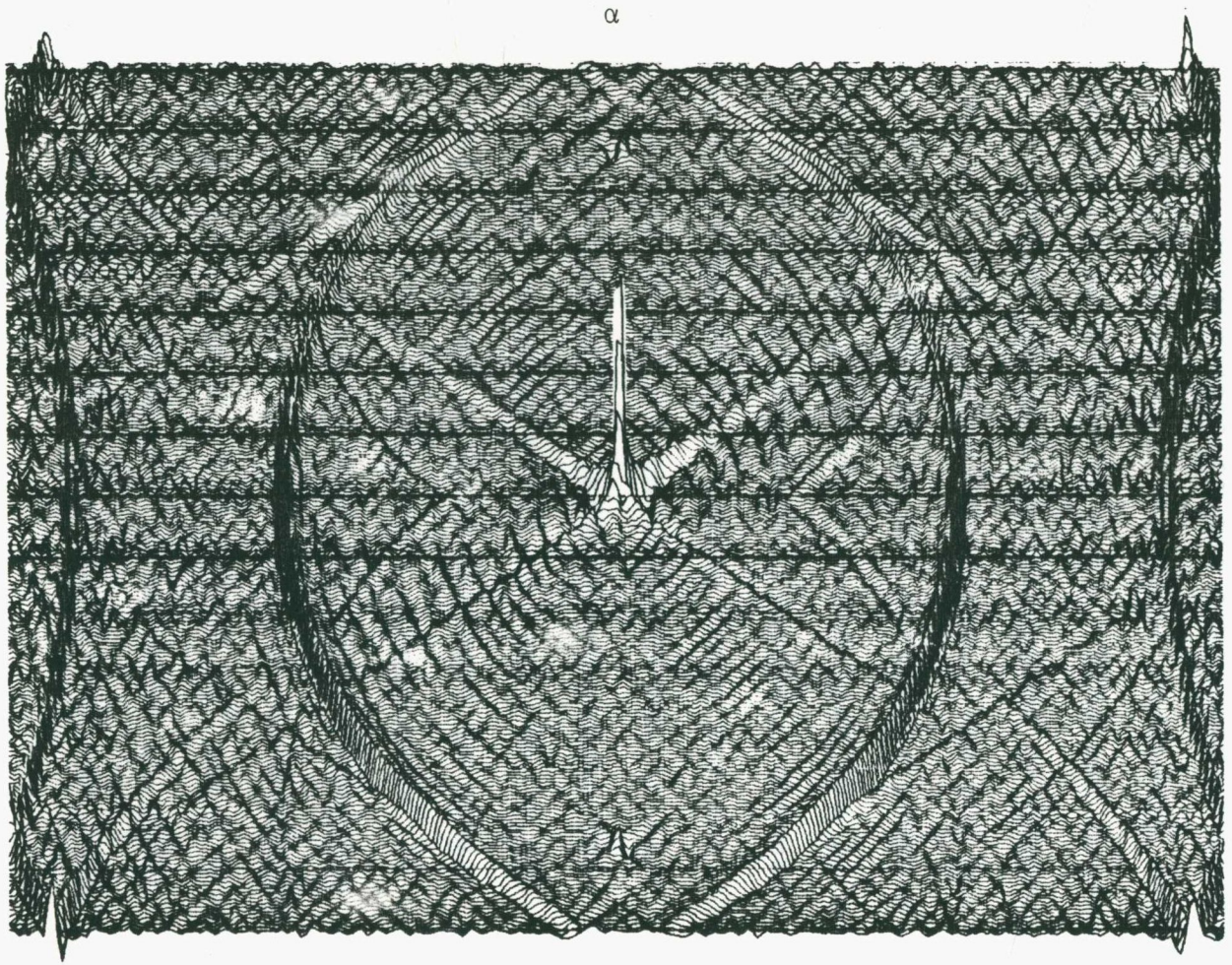

Figure 4-4 Three Dimensional Profile Plot of 0521-36

of 8 hours at a frequency of 1419.808 MHz. This frequency corresponds to the fifth of the six frequencies at which N300 was observed. One set of baseline parameters was obtained for each of the two frequency channels. Cross calibration (measurement of one frequency channel corrected by baseline parameters of the other frequency channel) performance is good (Figure 4-5). This can be expected as the parameters are mainly determined by errors in the assumed layout of the telescope. The 600 kHz separation between the two channels is not enough to produce significant differences in the parameters. The baseline parameters were applied to the respective frequency channels for all observations. The frequency range for the complete set of observations is from 1419.437 MHz to 1419.904 MHz. The frequency correction factors are ranges from 0.99974 to 1.0001, or a maximum error of less than 0.03%.

The calibrator 1934-63 was used to obtain the amplitude and phase calibration parameters. It was favoured over 0521-36 because it can be observed over a time when the Sun's interference is less prominent. The 1950 position is $\alpha = 19^h\ 34^m\ 47.57^s$ and $\delta = -63^o\ 49'\ 37.7"$. The 21 cm radio size is <15" (Frater et al. 1976). Its flux density is 16.4 Jy. Amplitude and phase calibrations were performed at each of the six frequencies used in the observation of N300. Each calibration observation was over a minimum of two hours spaced within two days of the HI observation. Typically, for each interferometer, the amplitude error is less than 4% and the phase error is less than 5^o.

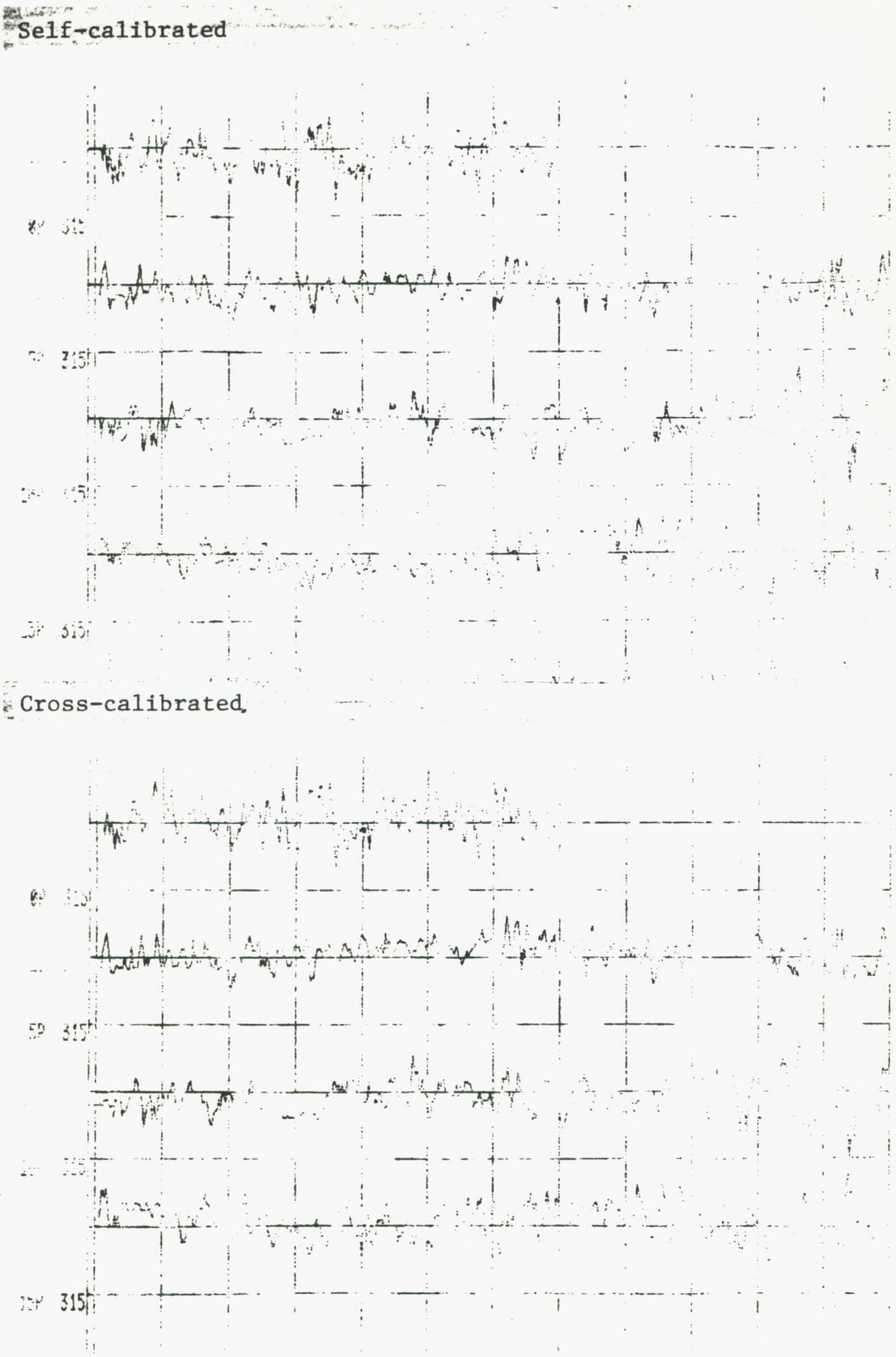

Vertical Scale = 45°/division

Figure 4-5 Sample Phase Plots of Data After Self Calibration and After Cross Calibration

4.5 Data Processing

Six 8 hour observations of N300 were made, resulting in 12 channel maps. Each map was produced with a Gaussian grading which tapers to 0.25 at the 396.24 m spacing. A map contains 256 × 256 points and covers a region $2.4^{\circ} \times 2.4^{\circ}$. This gives better than two points per beam in the narrower direction. The noise on the map is 2.3 K. Maps with noticeable radiation were enhanced by the procedure CLEAN. The beam patterns used are shown in Figure 4-6.

The maps contain HI and continuum radiation. The two types of radiation were separated by the window method. Neutral hydrogen radiation with a S/N less than three was discarded. The continuum map contains the continuum radiation, plus any undesirable responses which may be common to all maps. The HI maps were combined to give a map of the HI column density. This distribution map is corrected for the primary beam pattern. The velocity field over the galaxy was also obtained.

No attempts have been made to fill in the missing hole in the aperture and features greater than 40' are not properly measured.

4.6 Continuum Radiation

The $1.2^{\circ} \times 1.2^{\circ}$ map of 21 cm continuum radiation shows that N300 has a low continuum brightness (Figure 4-7). The map has not been corrected for the primary beam pattern. The contour interval is 2 K. The noise on the map varies. On the average it is 1.1 K. There

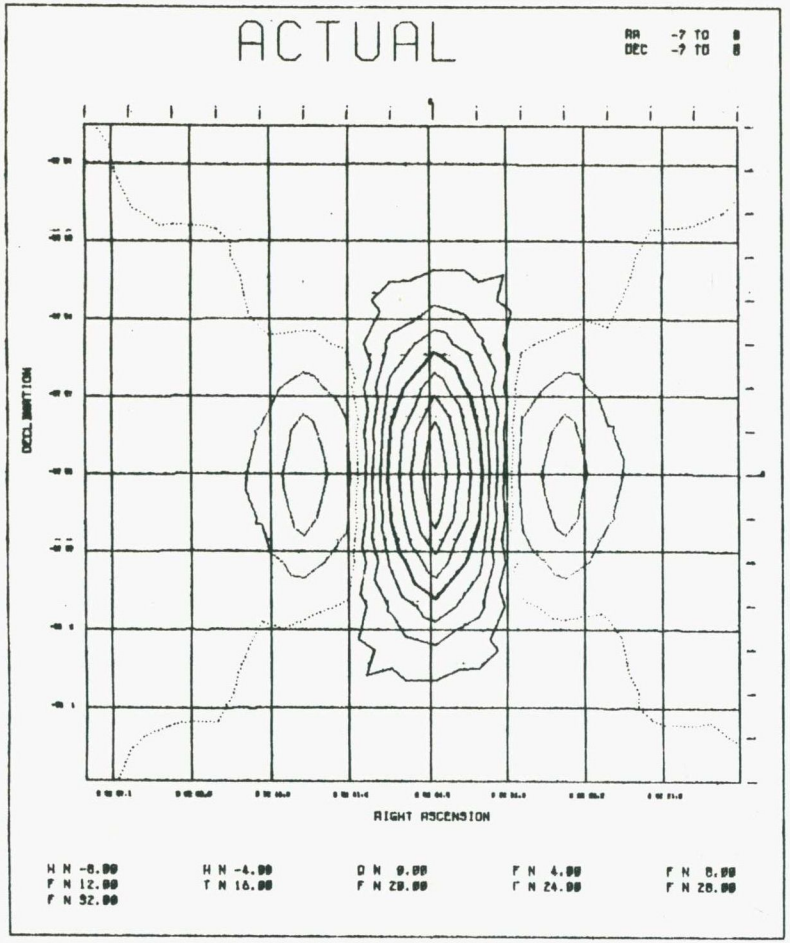

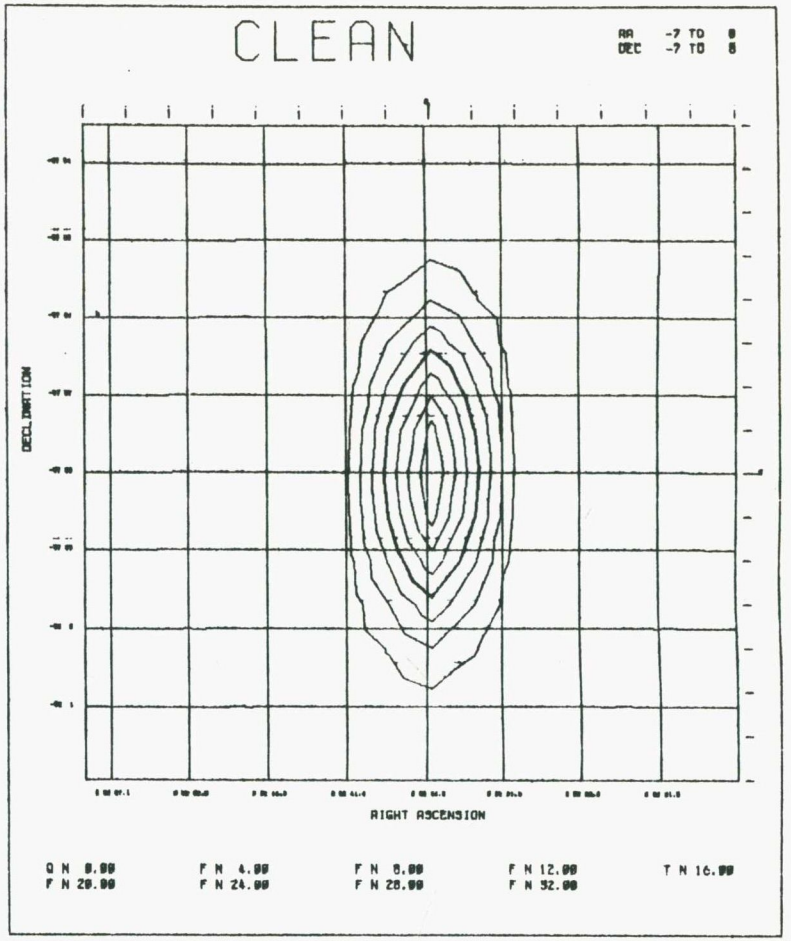

Figure 4-6 The Actual Synthesised Beam and the Clean Beam

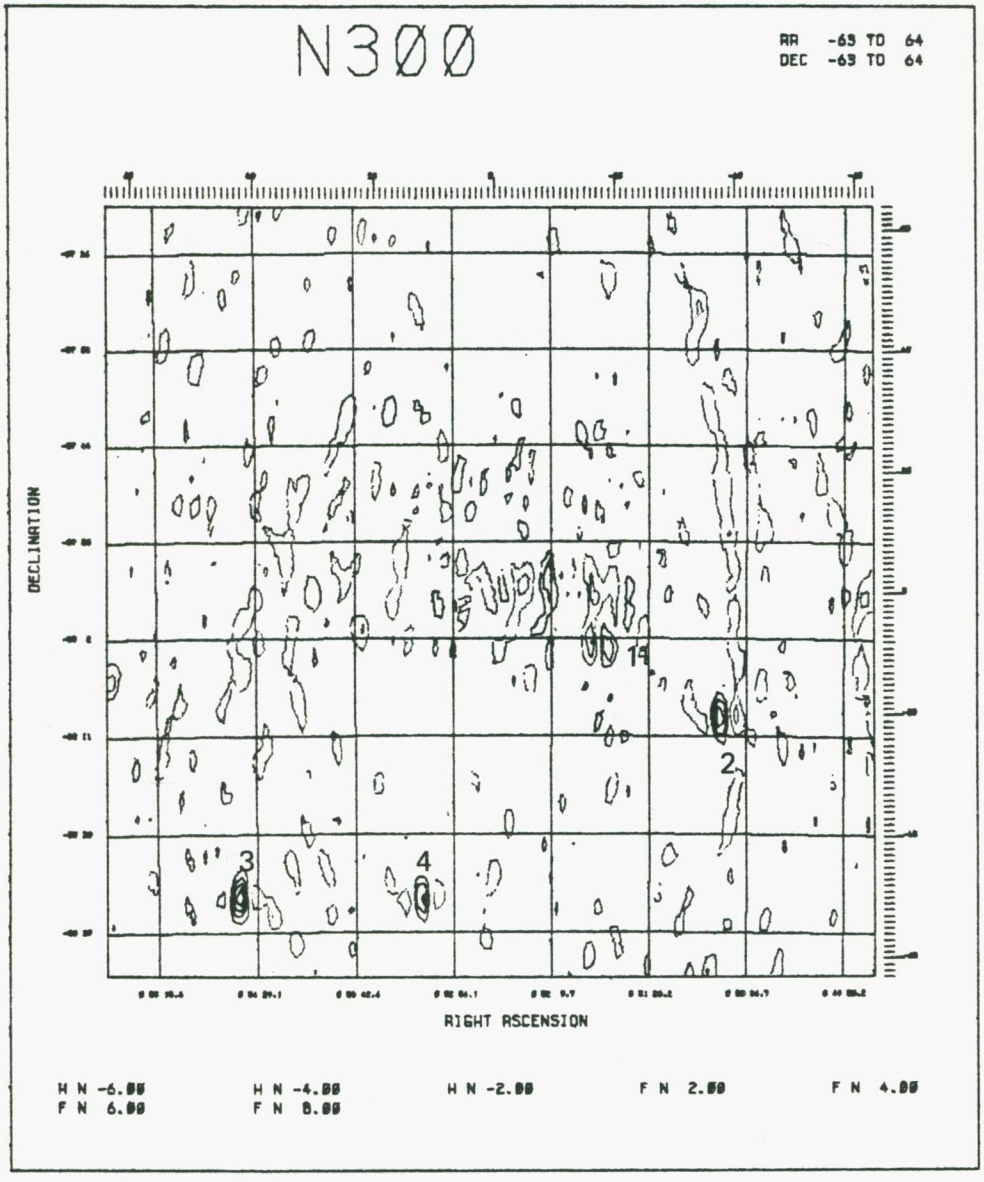

Figure 4-7 21 cm Continuum Radiation

is a negative mean over the map, pointing to the fact that the cleaning process may be incomplete.

There are four resolved continuum sources, none of which appears to be associated with N300. Of the three sources detected by Rogstad, Crutcher, and Chu (1979), only one (source 1 on the map) can be identified. This is attributed to the lower sensitivity of the FST. The positions and flux densities of the four sources were obtained by fitting them with the synthesised beam. The flux densities were further corrected for the primary beam. The parameters are listed in Table 4-2.

4.7 Distribution of Neutral Hydrogen

The 40' × 40' HI maps of N300 show that three of the maps contain little HI (Figure 4-8). These are the 40.5 km/s, 251.5 km/s, and 272.6 km/s maps. The identifying velocity is located above each map. The maps have not been corrected for the primary beam pattern. The average noise is 2.6 K. The contour interval is 6 K. Brightness temperature as high as 30 K was detected.

The primary beam corrected distribution map (Figure 4-9) has an average noise level of $7.2(10)^{20}$ atoms/cm^2. The contour unit is $3.6(10)^{19}$ atoms/cm^2 and the contour interval is 20 units. The crosses on the map refer to star positions.

The extent of the HI distribution is roughly 28' × 24' (20 kpc × 18 kpc) at the noise level. A low level extended component found in observations with better S/N has not been detected. The position angle of the major axis of the distribution is 110°.

Table 4-2 Detected Point Sources Around N300

Source number	α (1950)	δ (1950)	Flux density (Jy)
1	51^m43^s	-38°02′35″	0.14
2	50^m47^s	-38°10′14″	0.25
3	54^m36^s	-38°24′57″	0.44
4	53^m12^s	-38°25′25″	0.25

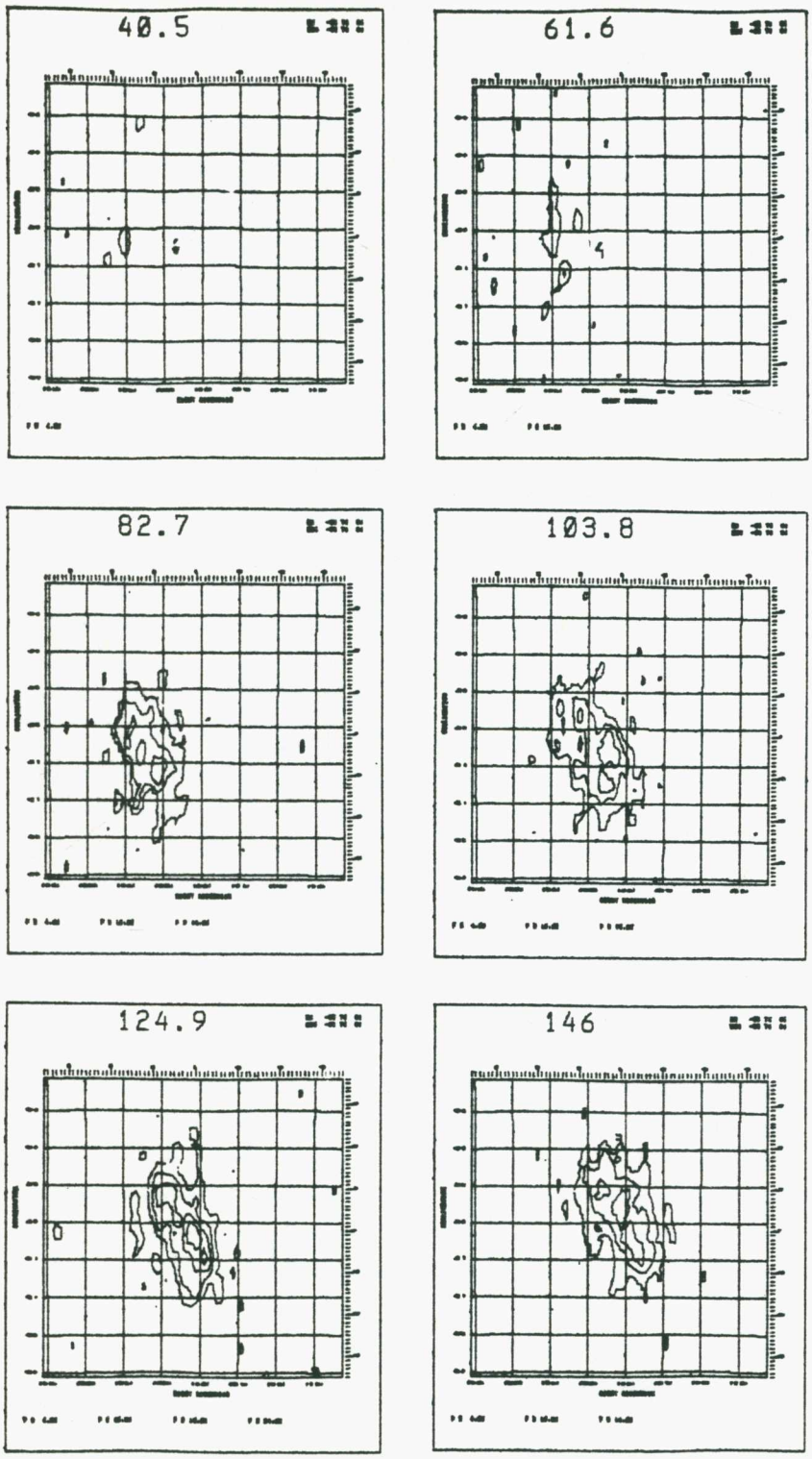

Figure 4-8 N300 - HI Maps

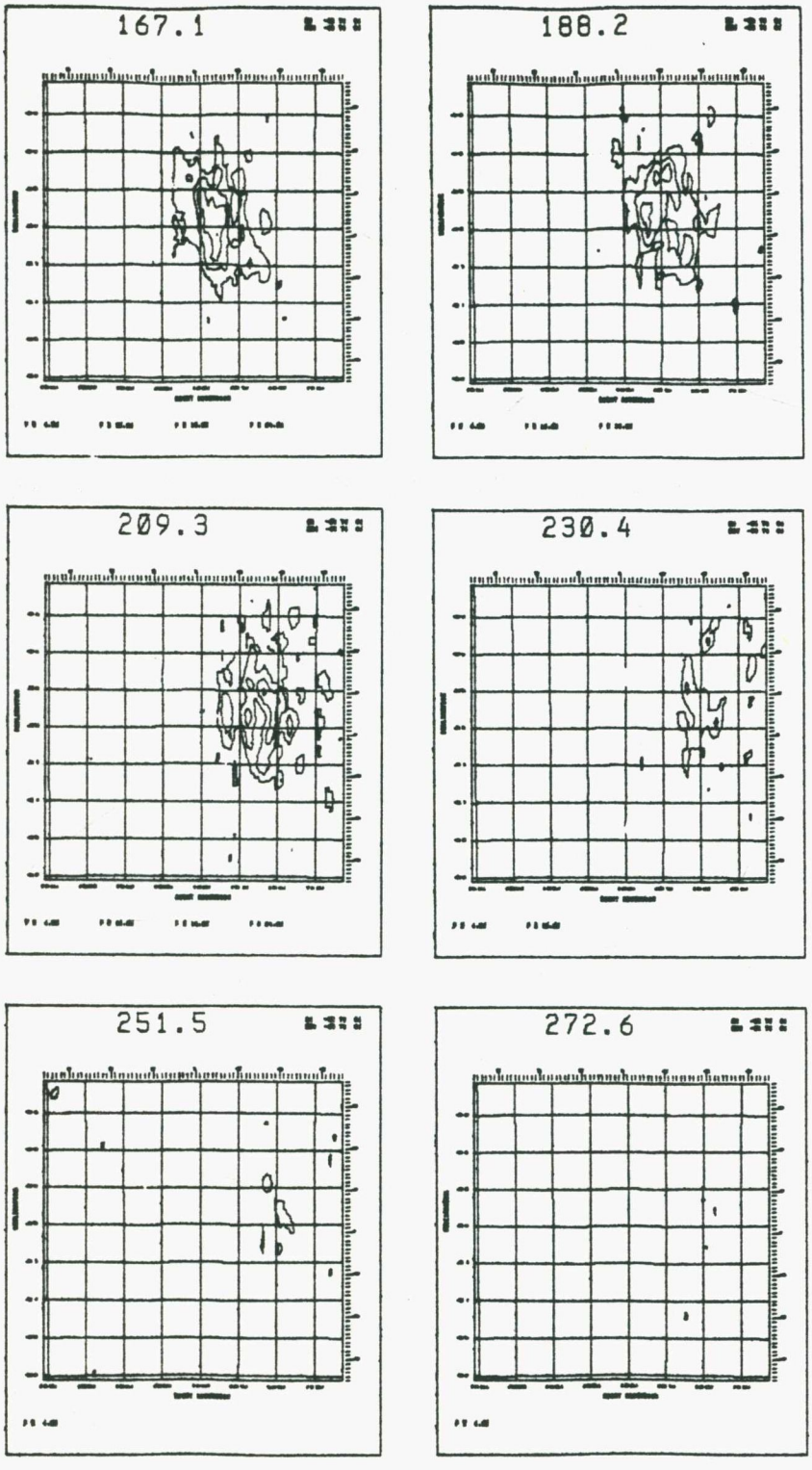

Figure 4-8 (...continued)

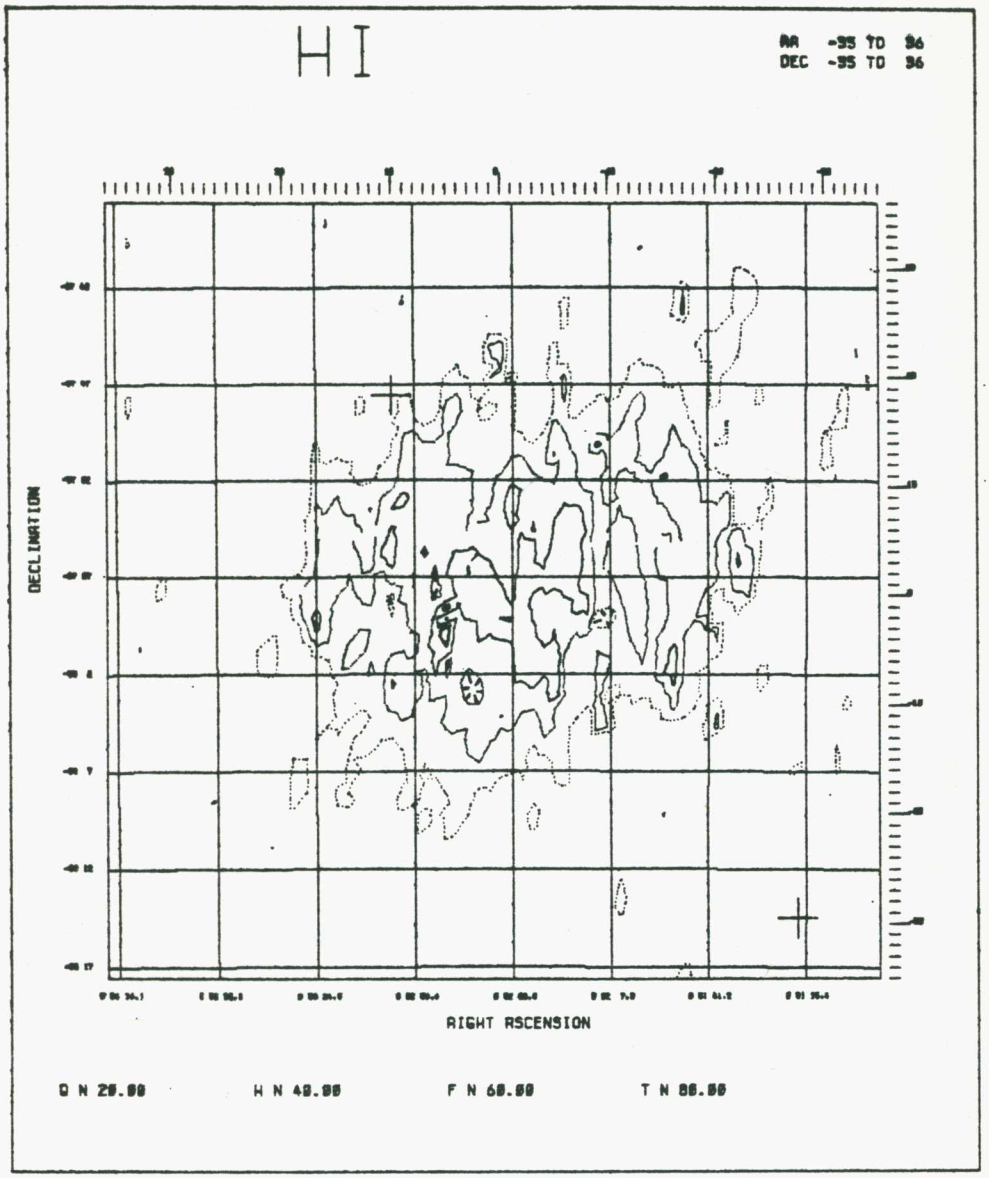

Figure 4-9 N300 - HI Distribution Map

A cut along the major axis (Figure 4-10) shows a simple spiral arm to the east and a complicated multiple arm to the west. A cut along the minor axis shows the arms to merge towards the center of the distribution, an apparent effect due to the inclination of the galaxy. There is a depressed valley in the distribution running up from the north to the center. There is no discernable central depression as noticed by other observers.

The total HI mass of the galaxy is $3.3(10)^9$ solar units. This can be compared with the value of $3.6(10)^9$ solar units obtained by Shobbrook and Robinson (1967), where the result has been scaled to the present adopted distance of the galaxy, and $2.5(10)^9$ solar units obtained by Rogstad, Crutcher, and Chu (1979). The M_H growth curve (Figure 4-11) starts to flatten out at a distance of 8 kpc from the center. About 18% of HI lies outside that radius. The HI mass center lies to the northwest (NW) of the optical center, at α (1950) $\simeq 52^m\ 31^s$ and δ (1950) $\simeq -37^\circ\ 57'$.

The total HI mass as obtained by (4-10) depends on the adopted distance of the galaxy. A distance independent parameter is given by the mean HI areal mass density, σ_H. This is defined as the HI mass density over the deprojected area of the galaxy,

$$\sigma_H = M_H/(\pi r_g^2) \qquad (4\text{-}11)$$

where r_g is the radial extent of the galaxy along the major axis. It is assumed that the galaxy resembles a circular disk.

To include all HI within the galaxy, M_H was

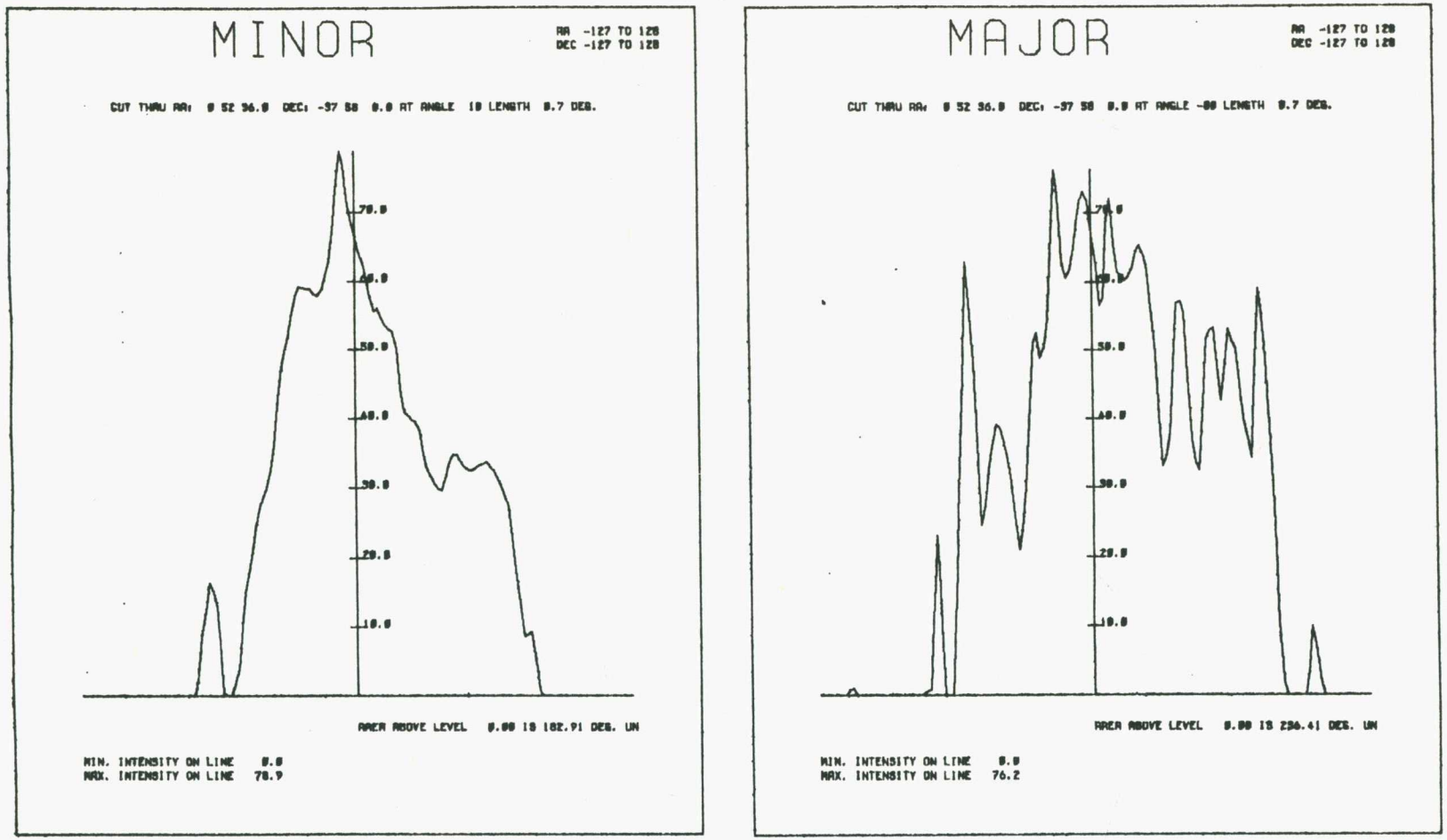

Figure 4-10 HI Distribution Along the Minor and Major Axis of N300

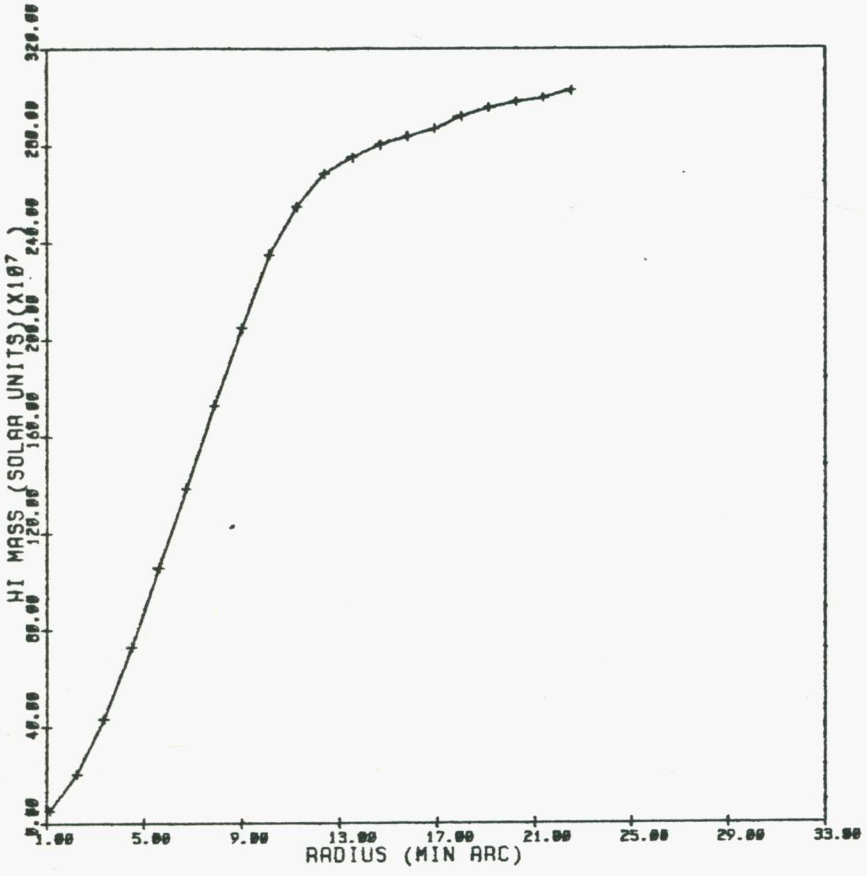

Figure 4-11 Growth Curve of Total HI Mass

obtained over a region larger than that given by the one σ'_{int} level on the distribution map. For the purpose of determining the area of the galaxy, the radial extent is taken to be 14 kpc. This is the extent to which the velocity field can be properly determined. The mean HI areal mass density of N300 is $1.1(10)^{-3}$ g/cm^2.

The distance independent parameter, HI mass to luminosity ratio, is 0.92 solar units.

4.8 Velocity Field

Selected velocity profiles are presented at 9' intervals on a rectangular grid centered at the optical center of the galaxy (Figure 4-12). The profiles are obtained from maps which have not been corrected for the primary beam pattern. The velocity field is shown in Figure 4-13. The accuracy in velocity is better than 6 km/s. The general shape of the velocity contours implies simple circular motion in N300 out to the limits of measurement. Model velocity fields are given in Appendix B.

There are deviations from the general shape of the field, indicating non-circular motions. The velocity contours to the southeast (SE) are at a position angle of 120°, a change of 10° anticlockwise from the distribution. This correlates well with the notion that there is a perturbing mass in that direction. The heliocentric systemic velocity is determined to be 147 km/s, given by the line of sight velocity at the optical center of the galaxy.

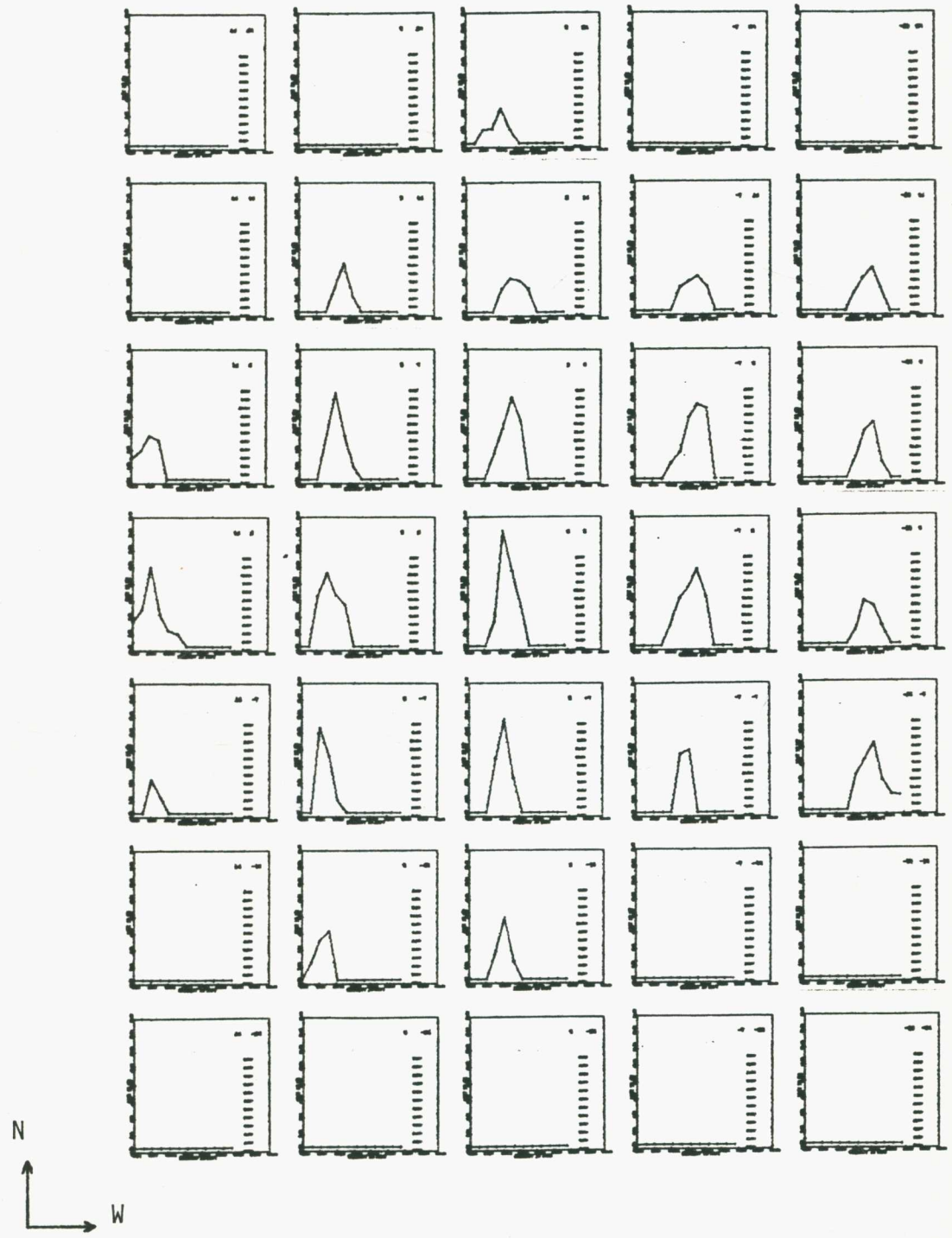

Figure 4-12 Sample Velocity Profiles

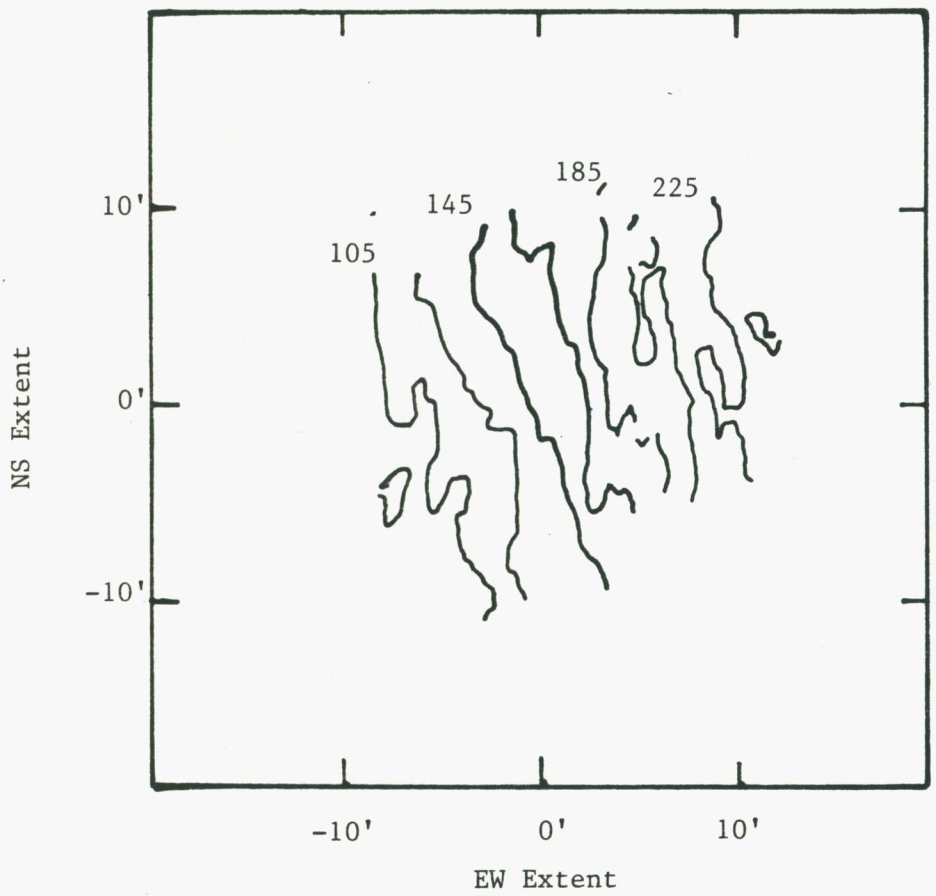

Figure 4-13 N300 - Velocity Field

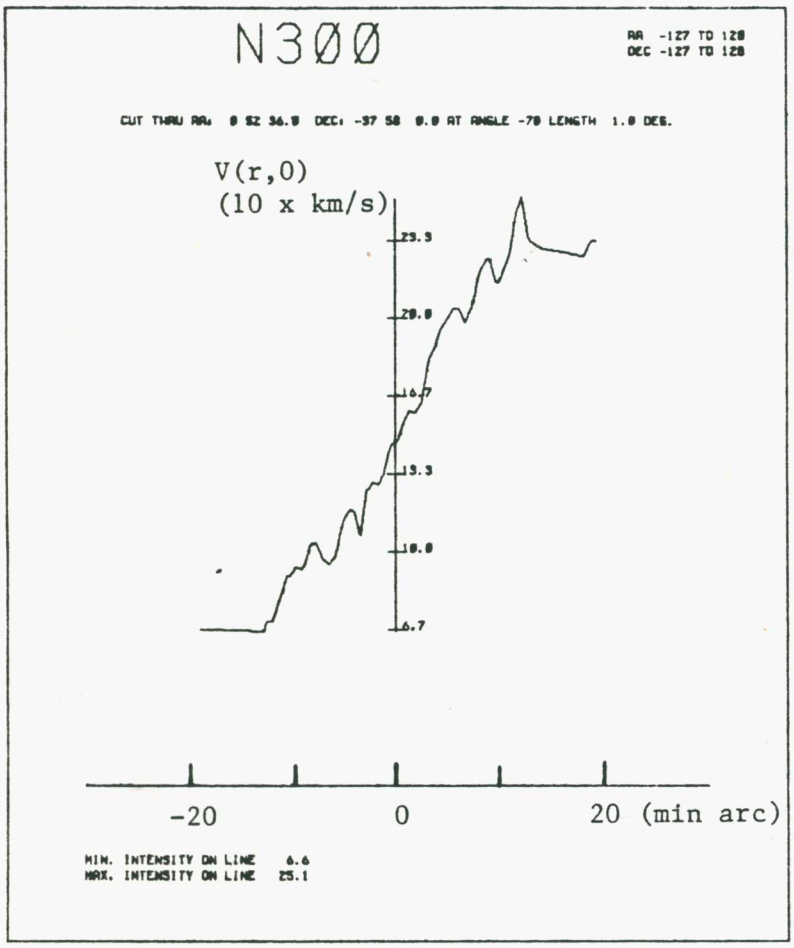

Figure 4-14 Line of Sight Velocity Along the Major Axis of N300

4.9 Rotation Curve

The variation of the line of sight velocity along the major axis is presented in Figure 4-14. If there is no motion normal to the plane of the galaxy, the rotational velocity can be found by equation (B-1),

$$v_\phi(r,\phi) = \{v(r,0) - v_o\}/\sin(i) \qquad (4\text{-}12)$$

The total mass, M_T, of N300 can be estimated from the law of gravitation. If $v_\phi(r_g,\phi)$ is the rotational velocity at the edge of the galaxy, then

$$M_T = r_g v_\phi^2(r_g,\phi)/G \qquad (4\text{-}13)$$

where $G \simeq 6.668(10)^{-11}$ $m^3/(kg\ s^2)$ is the universal constant of gravitation.

An inclination of 42.5^o is adopted for N300. The rotation curve is measured out to 13.8 kpc from the optical center to the SE, with a rotational velocity of -118 km/s, and 14.2 kpc to the NW, with a rotational velocity of 127 km/s. Taking r_g as 14 kpc and $v_\phi(r_g,\phi)$ as 122 km/s, the total mass of N300 was found to be $4.8(10)^{10}$ solar units.

The rotation curve starts to turn over at a distance of 9.3 kpc from the optical center of N300. The ratio of this turnover radius to the Holmberg radius is 0.95. This can be compared to the value of 0.8 deduced by Huchtmeier (1975) for a galaxy of type Sc - Scd. The total mass to luminosity ratio is 13 solar units. The HI mass to total mass ratio is 0.07. The respective values obtained by Shobbrook and Robinson (1967) are 10.9 solar units and 0.084.

4.10 References

Epstein, E. E. "Atomic Hydrogen in Galaxies", Astron. J., vol. 69, 490-520, 1964.

Frater, R. H., A. Watkinson, D. S. Retallack, and W. M. Goss. "Calibration Source Positions from the Fleurs Synthesis Telescope", Mon. Not. R. Astr. Soc., vol. 176, 487-493, 1976.

Huchtmeier, W. K. "Rotation-curves of Galaxies from 21 CM-line Observations", Astron. & Astrophys., vol. 45, 259-268, 1975.

Kerr, F. J. "Radio-Line Emission and Absorption by Interstellar Gas", Nebulae and Interstellar Matter, B. M. Middlehurst and L. H. Aller, ed. University of Chicago Press, 1968.

Rogstad, D. H., R. M. Crutcher, and K. Chu. "Aperture-synthesis Observations of HI in the Galaxy NGC300", Astrophys. J., vol. 229, 509-513, 1979.

Shobbrook, R. R. and B. J. Robinson. "21 cm Observations of NGC300"; Aust. J. Phys., vol. 20, 131-145, 1967.

Spitzer, L., Jr. "Diffuse Matter in Space". Interscience Publishers, 1968.

Whiteoak, J. B. and F. F. Gardner. "Observations of Neutral Hydrogen in Bright Southern Galaxies", Aust. J. Phys., vol. 30, 187-207, 1977.

CHAPTER V INTERFERENCE

5.1 Nature of Interference

The usefulness of a measurement is affected by the inherent noise in the measuring instrument and by interference. Both are detrimental to the measurement. Noise results from uncorrelated sources. Interference results from correlated sources.

Noise cannot be reduced by analytical methods. Interference, on the other hand, can be reduced by analytical methods. If the source of interference is known, its properties can be mathematically formulated and can be removed from the measurement. In a multichannel spectral line experiment, interferences which do not change with frequency can also be removed by the window method (section 3.8).

A correlation receiver (as used in the FST) has a mean output given by (2-19). The spectral density of the correlated quantities consists of two components, the spectral density of the radiation of interest, $S_r(\nu)$, and the spectral density of the interference, $S_i(\nu)$,

$$S_{s'}(\nu) = S_r(\nu) + S_i(\nu) \tag{5-1}$$

The mean output of the correlator can be rewritten as

$$o_s = K\{\int H_1(\nu)H_2^*(\nu)S_r^*(\nu)d\nu + \int H_1(\nu)H_2^*(\nu)S_i^*(\nu)d\nu\} \tag{5-2}$$

If $S_r(\nu)$ is constant over the frequency range of interest, the first term is given by (2-42). Two cases of $S_i(\nu)$

will be considered. In one case, $S_i(\nu)$ is assumed to be constant with frequency. In the other case, $S_i(\nu)$ assumes a value at only one frequency.

When $S_i(\nu)$ does not vary with frequency, (5-2) becomes

$$o_s = 2KH_1(\nu_i)H_2(\nu_i)\{S_r(\nu_i) + S_i(\nu_i)\}W \qquad (5\text{-}3)$$

When $S_i(\nu)$ exists only at one frequency and is covered by the receiver bandwidth, (5-2) becomes

$$o_s = 2KH_1(\nu_i)H_2(\nu_i)\{S_r(\nu_i)W + S_i\} \qquad (5\text{-}4)$$

Equation (5-4) shows that narrowband interference is more detrimental to a narrowband receiver than to a wideband receiver.

In a synthesis telescope, the effect of interference on the observed data depends on the intensity and the received phase of the interference. The maximum expected interference is determined by its intensity. But if the received phase goes through several cycles over an integration period of the receiver, the interference will be reduced. The expected maximum is attained only when the received phase of the interference becomes stationary. Knowledge of the conditions under which this occurs for different interfering sources is important in understanding the effect of the interferences.

5.2 Interference from Local Oscillator Noise

In a synthesis telescope such as the FST in which the local oscillator (LO) signal to the antennas is derived from a common source, any LO contribution to the IF will be correlated and can appear as interference

in the measurement. The expected maximum interference level can be minimised by restricting the frequency response in the LO path.

The signal flow in the Fleurs receiver has been depicted by the simplified diagram in Figure 2-13. The LO contribution to the IF at the output of the mixer can be represented by

$$l_{IF}(t) = l_*(t)e^{-j2\pi\nu_i t} \qquad (5\text{-}5)$$

where * is either 1 or 2, denoting respectively the two correlating channels. After delay compensation, phase rotation, correlation, and integration, the contribution becomes

$$o_1 = E\{l_1(t+\tau_1)l_2(t+\tau_2)e^{j2\pi(\delta\nu\delta\tau - \nu_t\tau_{\sigma_o})}\} \qquad (5\text{-}6)$$

The phase terms result from three different causes. The first term arises from a combination of frequency offset and delay tracking error. The second term arises from phase tracking by the pilot signals. The effect of the first term has been discussed in section 2.11. The effect of the second term will be investigated here.

The data collected by the FST are phase switched at one minute intervals. Demodulation is performed by software. The LO contribution to the measurement is not phase switched, and demodulation gives

$$o_{1_d}(t) = \Phi(t)o_1 \qquad (5\text{-}7)$$

where $\Phi(t) = \pm 1$ on alternate minutes is the phase switch function. The function can be Fourier expanded into

$$\Phi(t) = 2/(j\pi) \times \sum_{n \text{ odd}} e^{j2\pi n\nu_\Phi t}/n \qquad (5\text{-}8)$$

where ν_Φ is the switching frequency. It has been assumed that the function is aligned in time such that a transition from negative to positive occurs at t = 0. Other alignments can be accommodated by adding a constant phase to all the components.

Maximum interference occurs at the hour angle when the rate of rotation of the LO contribution equals that of the phase switch. Neglecting the normally small contribution from $2\pi\delta\nu\delta\tau$, the phase of the LO contribution can be expressed as (ψ_W for an EW array and ψ_S for a NS array)

$$\begin{aligned}\psi_W &\simeq -2\pi\nu_t/c \times r\cos(\delta_{\sigma_o})\sin(h_{\sigma_o}) \\ \psi_S &\simeq -2\pi\nu_t/c \times r\{\sin(\theta)\cos(\delta_{\sigma_o})\cos(h_{\sigma_o}) + \\ &\qquad \cos(\theta)\sin(\delta_{\sigma_o})\}\end{aligned} \qquad (5\text{-}9)$$

The rates of rotation are

$$\begin{aligned}d\psi_W/dt &\simeq -2\pi\nu_t/c \times r\cos(\delta_{\sigma_o})\cos(h_{\sigma_o})(dh_{\sigma_o}/dt) \\ d\psi_S/dt &\simeq 2\pi\nu_t/c \times r\sin(\theta)\cos(\delta_{\sigma_o})\sin(h_{\sigma_o})(dh_{\sigma_o}/dt)\end{aligned} \qquad (5\text{-}10)$$

where $dh_{\sigma_o}/dt = \Omega$ is the sidereal rate of rotation of the Earth.

The phase rotation stops when

$$d\psi_*/dt = -2\pi n\nu_\Phi \qquad (5\text{-}11)$$

where * denotes either W or S. The hour angles at which phase stopping occurs are

$$\begin{aligned}h_{\sigma_{oW}} &= \cos^{-1}\{c/\nu_t \times n\nu_\Phi/(r\cos(\delta_{\sigma_o}) \times \Omega)\} \\ h_{\sigma_{oS}} &= -\sin^{-1}\{c/\nu_t \times n\nu_\Phi/(r\sin(\theta)\cos(\delta_{\sigma_o}) \times \Omega)\}\end{aligned} \qquad (5\text{-}12)$$

for the EW and NS arrays respectively.

In the FST, the physical spacings are given by $(i + \frac{1}{2})d$ and $\Phi(t)$ switches at 1/120 Hz. The hour angles at which the phase is stopped by the fundamental component of the phase switch function are plotted at three declinations for spacings 1 to 32 (Figure 5-1). The frequency used is 1420 MHz. The location of the hour angles is symmetrical with respect to transit. It will be noted that for the restricted hour angle coverage of $\pm 60^{\circ}$ at Fleurs, more spacings are affected by this type of interference in a NS observation than in an EW observation.

From (5-6), it can be seen that when the phase tracking rate is high compared with the data sampling rate, $o_{1_d}(t)$ will be small. The range of hour angle over which the interference is effective and the intensity of the interference decrease for higher spacings. This is generally true, and low spacing data are particularly prone to various forms of interference. Similarly, interference produced by means of the higher harmonics of the phase switch is less effective.

The above analysis has been based on the LO noise as the source of interference. It can be generalised to include any disturbances which are common to both correlating telescopes and have bypassed the phase switch. The type of interference is portrayed in the data collected from one EW observation of the calibrator 1934-63 (Figure 5-2). Its effect is to produce a periodic pattern in the map domain (Figure 5-3). At Fleurs, the interference was minimised by inserting a narrowband

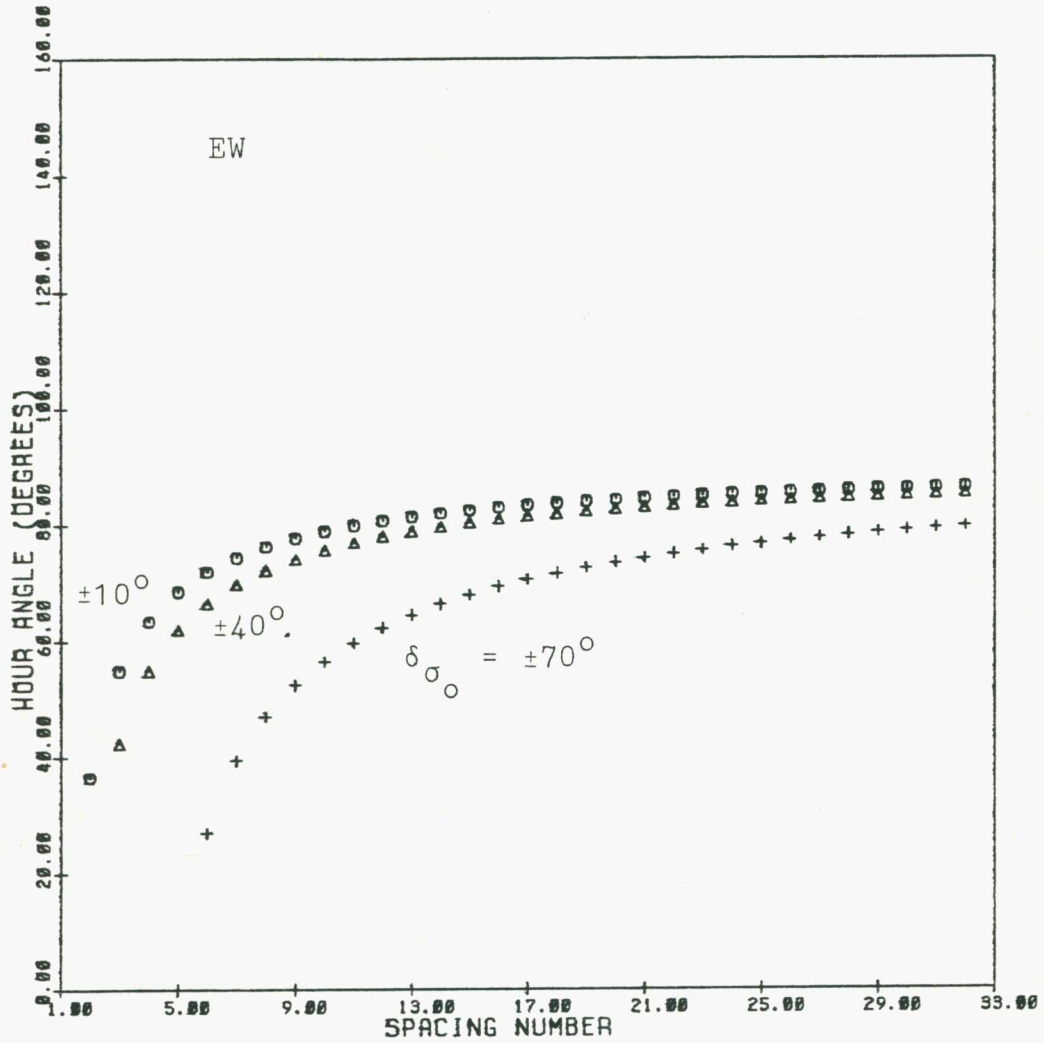

Figure 5-1a Hour Angles of Maximum LO Interference

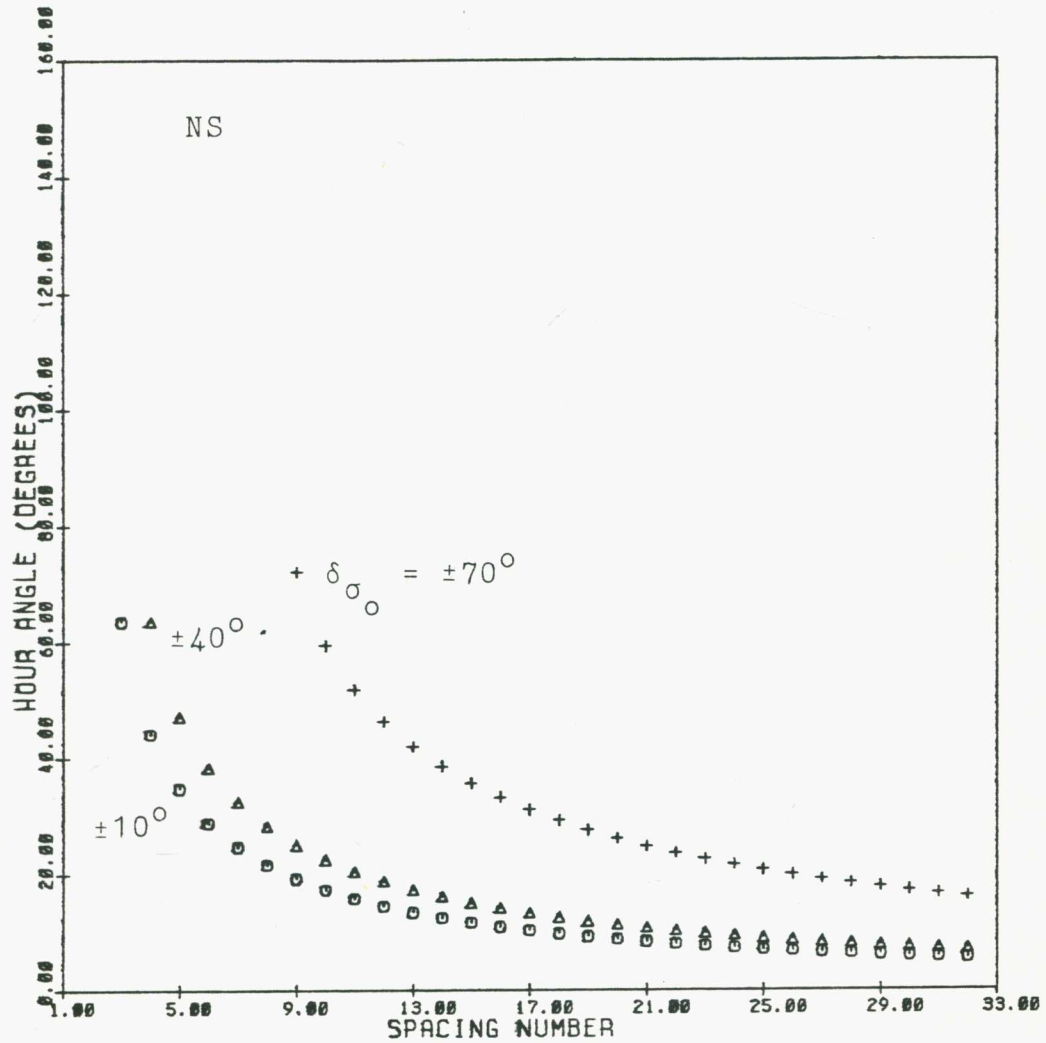

Figure 5-1b Hour Angles of Maximum LO Interference

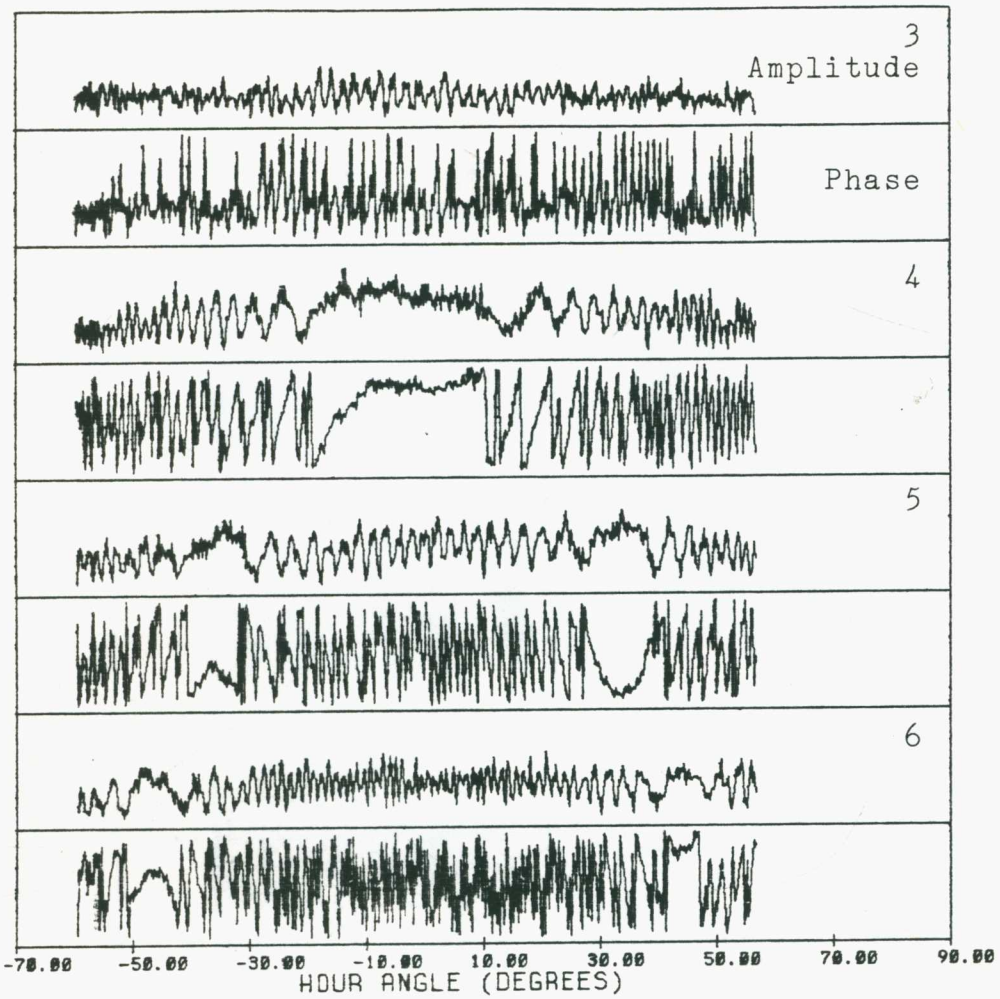

Figure 5-2 Channel Data with LO Interference

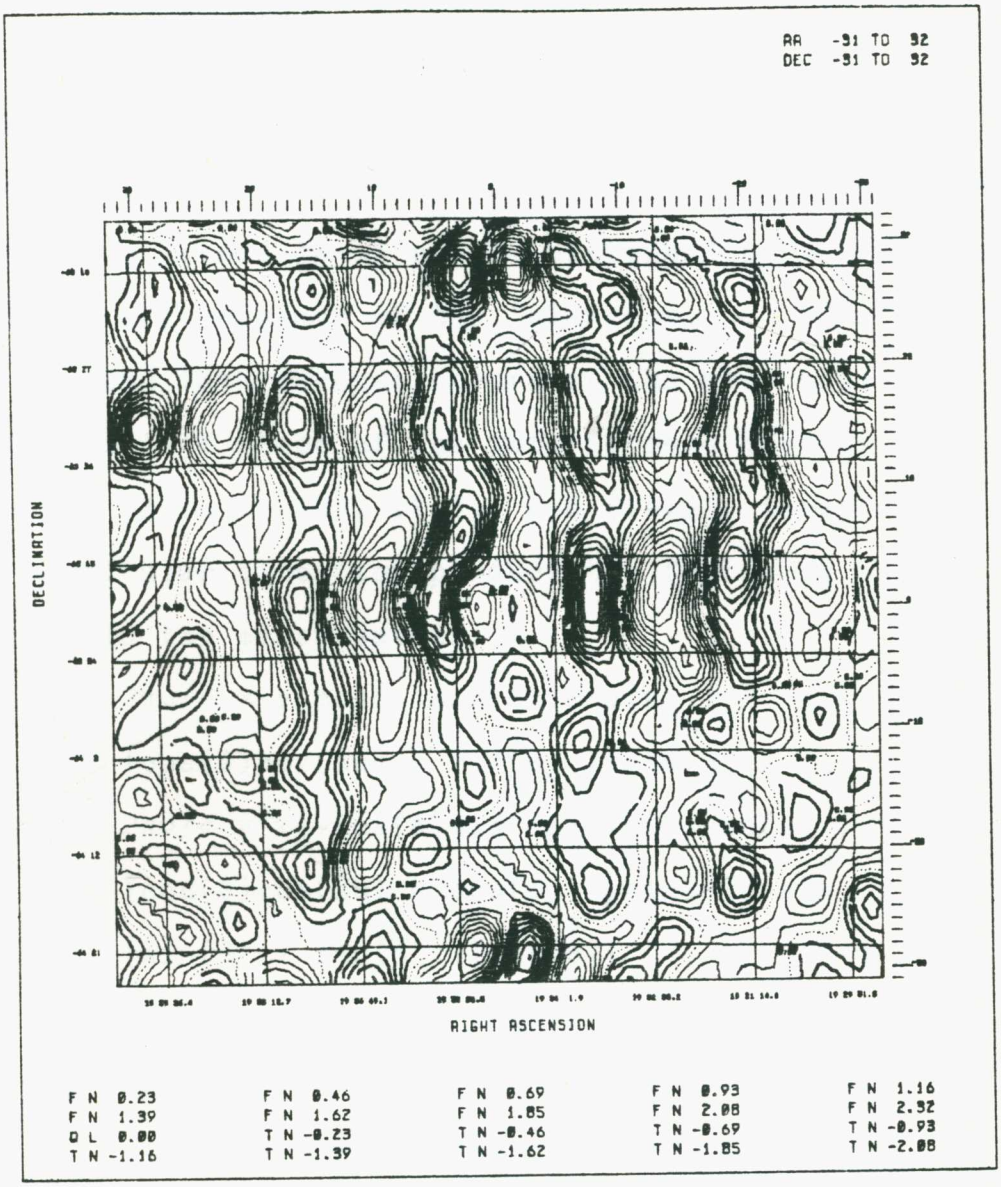

Figure 5-3 Map of LO Interference

tuned cavity filter in the LO path.

5.3 Interference from External Sources

In the observation of a radiation field, any contribution to the measurement from radiation outside the field will be regarded as interference. The expected maximum interference level can be minimised by restricting the primary sky response of the telescope.

Maximum interference occurs at the hour angle when the received phase of the interference becomes stationary. From (1-12), (1-7), and (1-14), interferences from a particular direction produce the following phase variations in the measurements,

$$\psi_W = 2\pi\nu/c \times r\{\cos(\delta)\sin(\Delta h)\cos(h_{\sigma_o}) + [\cos(\delta)\cos(\Delta h) - \cos(\delta_{\sigma_o})]\sin(h_{\sigma_o})\}$$

$$\psi_S = 2\pi\nu/c \times r\{-\cos(\delta)\sin(\Delta h)\sin(\theta)\sin(h_{\sigma_o}) + [\cos(\delta)\cos(\Delta h) - \cos(\delta_{\sigma_o})]\sin(\theta)\cos(h_{\sigma_o}) - [\sin(\delta) - \sin(\delta_{\sigma_o})]\cos(\theta)\} \quad (5\text{-}13)$$

where $\Delta h = -\Delta\alpha$. The rates of rotation are

$$d\psi_W/dh_{\sigma_o} = 2\pi\nu/c \times r\{-\cos(\delta)\sin(\Delta h)\sin(h_{\sigma_o}) + [\cos(\delta)\cos(\Delta h) - \cos(\delta_{\sigma_o})]\cos(h_{\sigma_o})\}$$

$$d\psi_S/dh_{\sigma_o} = -2\pi\nu/c \times r\{\cos(\delta)\sin(\Delta h)\sin(\theta)\cos(h_{\sigma_o}) + [\cos(\delta)\cos(\Delta h) - \cos(\delta_{\sigma_o})]\sin(\theta)\sin(h_{\sigma_o})\} \quad (5\text{-}14)$$

The hour angles at which phase stopping occurs are

$$h_{\sigma_{oW}} = \tan^{-1}\{[\cos(\Delta h) - \cos(\delta_{\sigma_o})/\cos(\delta)]/\sin(\Delta h)\}$$

$$h_{\sigma_{oS}} = \tan^{-1}\{\sin(\Delta h)/[\cos(\delta_{\sigma_o})/\cos(\delta) - \cos(\Delta h)]\} \quad (5\text{-}15)$$

Equations (5-15) are plotted for several values of $\cos(\delta_{\sigma_o})/\cos(\delta)$ (Figures 5-4 and 5-5). It will be

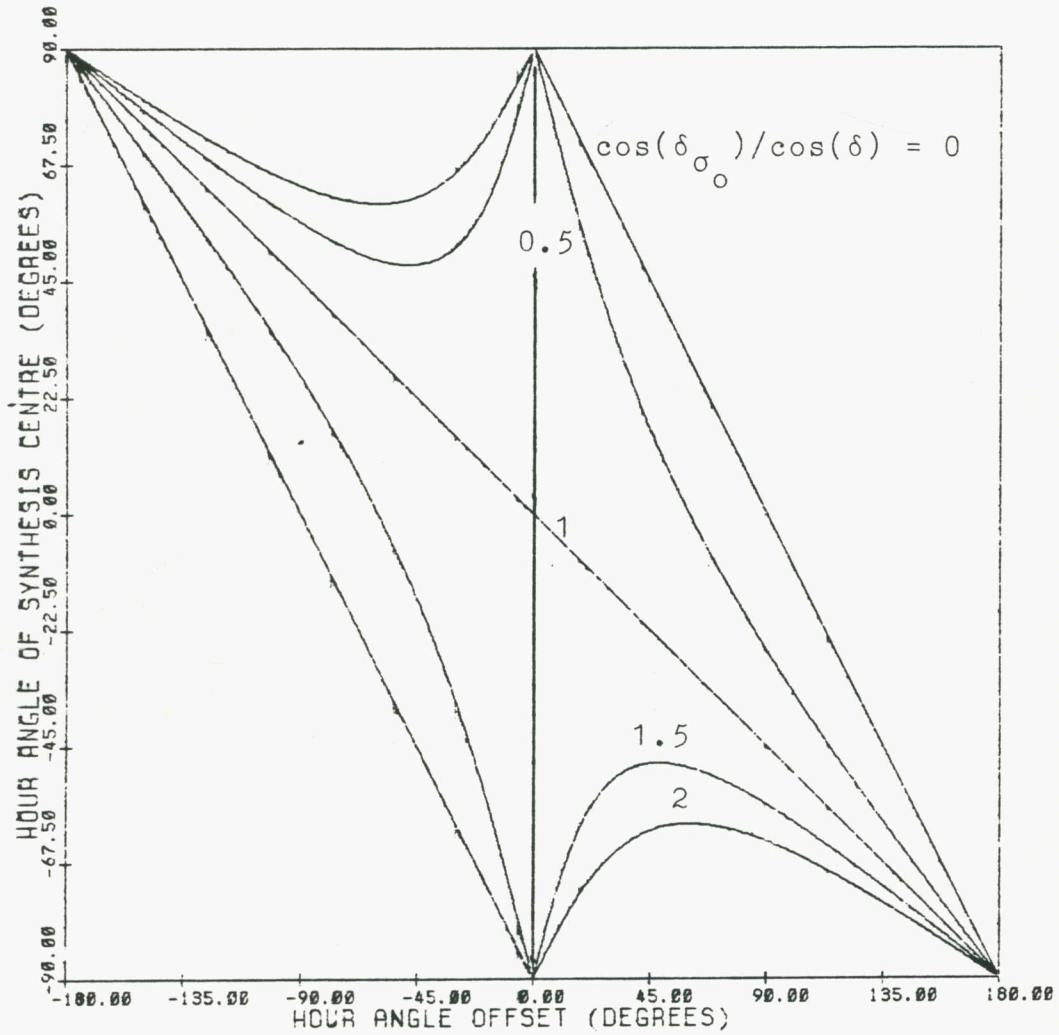

Figure 5-4 Interference from External Sources on an EW Observation

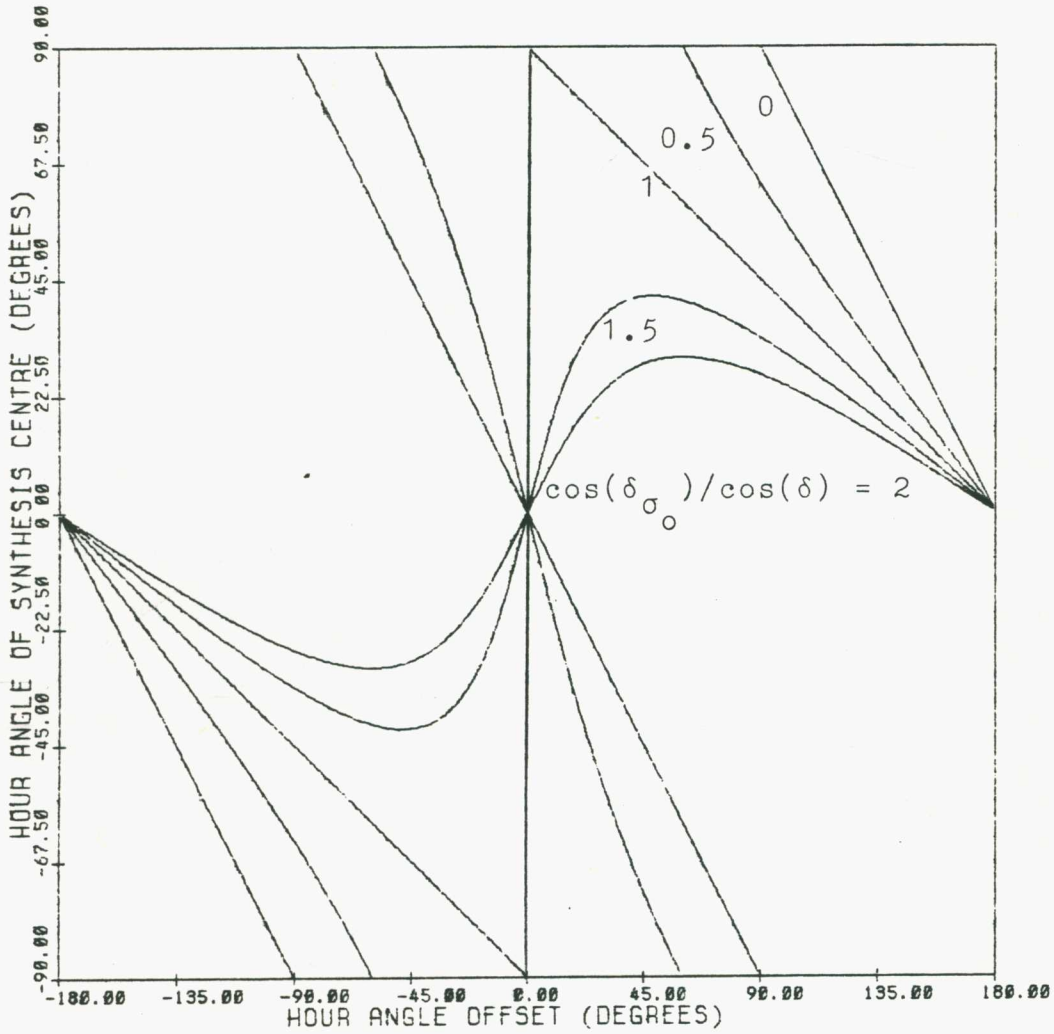

Figure 5-5 Interference from External Sources on a NS Observation

noted that for values less than unity, not all hour angles are interference susceptible. In particular, for an EW array, when the ratio is greater than sec(H) (H being a specified hour angle), then the range $-H \leq h_{\sigma_o} \leq H$ will be relatively free of interference. For Fleurs, the lower limit of the ratio is 2. In the case of a NS array, there will always be a region around transit which is prone to interference. Generally, the range of hour angle which is not affected by interference increases as $\cos(\delta_{\sigma_o})/\cos(\delta)$ increases. The interference maximises at the same hour angle for all spacings. However, for interfering sources from outside the field of view of the telescope, the maximum intensity of the interference decreases for increasing spacing numbers according to the data sampling restriction (section 1.10). Two frequently encountered interference sources will be discussed below. One is the Sun and the other is radiation over the horizon.

The Sun is a potent interfering source. The solar flux density at 1420 MHz can range from 0.1 MJy for the quiet Sun to as high as 100 MJy for the disturbed Sun. Any daytime observation may be susceptible to the interference from the Sun. The declination of the Sun lies between $\pm 23.5^{\circ}$, giving values of $\cos(\delta_{\sigma_o})/\cos(\delta)$ between 0 and 1.09. From the current position of the Sun, the hour angle offset for a particular observation can be calculated and the times of interference predicted. Armed with this information, the observation can be

scheduled to avoid the interfering period.

The direction of interference over the horizon will normally known by its azimuth. This can be converted to the equatorial co-ordinates by (1-22) and Figures 5-4 and 5-5 can be used to predict its occurrence. An interesting application of this is the reverse problem of finding the unknown direction of interference over the horizon. The measurements give the hour angle at which the phase of the interference becomes stationary. From (1-22), the following is obtained,

$$\cos(h_{\sigma_o} + \Delta h) = -\tan(\theta)\tan(\delta) \qquad (5\text{-}16)$$

which in conjunction with (5-15) and the measured h_{σ_o} gives Δh and δ. The azimuth of the interference can be found through (1-22).

APPENDIX A BASELINE ERRORS

Baseline errors modify the phase of a synthesis measurement. A baseline is defined by r, h_r, and δ_r. The phase of a measurement is given by (1-8). The phase errors due to the baseline errors Δr, Δh_r, and $\Delta\delta_r$ are

$$\Delta\psi_* = 2\pi\nu/c \times \{l(\partial r_x/\partial *) + m(\partial r_y/\partial *) + n(\partial r_z/\partial *)\}\Delta * \qquad (A\text{-}1)$$

where * denotes r, h_r, or δ_r.

The errors are measured by observing a point source at the synthesis center. Equation (A-1) becomes

$$\Delta\psi_* = 2\pi\nu/c \times \{\cos(\delta_{\sigma_o})(\partial r_y/\partial *) + \sin(\delta_{\sigma_o})(\partial r_z/\partial *)\}\Delta * \qquad (A\text{-}2)$$

Using (1-7), the phase error components can be obtained,

$$\begin{aligned}
\Delta\psi_r &= 2\pi\nu/c \times \{\cos(\delta_{\sigma_o})\cos(\delta_r)\cos(h_r - h_{\sigma_o}) + \\
&\quad \sin(\delta_{\sigma_o})\sin(\delta_r)\}\Delta r \\
\Delta\psi_{h_r} &= -2\pi\nu/c \times r\cos(\delta_{\sigma_o})\cos(\delta_r)\sin(h_r - h_{\sigma_o})\Delta h_r \\
\Delta\psi_{\delta_r} &= 2\pi\nu/c \times r\{-\cos(\delta_{\sigma_o})\sin(\delta_r)\cos(h_r - h_{\sigma_o}) + \\
&\quad \sin(\delta_{\sigma_o})\cos(\delta_r)\}\Delta\delta_r \qquad (A\text{-}3)
\end{aligned}$$

The total phase error due to the baseline errors is

$$\Delta\psi = \Delta\psi_r + \Delta\psi_{h_r} + \Delta\psi_{\delta_r} \qquad (A\text{-}4)$$

APPENDIX B MODEL VELOCITY FIELDS

The velocity measured in a spectral line observation is the velocity component along a line joining the telescope and the galaxy under observation. The relative velocity between the galaxy and the telescope is the systemic velocity v_o (the points of reference are normally the optical center of the galaxy and the phase center of the telescope). The galactic motion about its point of reference is represented by a radial velocity v_r, a rotational velocity v_ϕ, and a velocity in a direction normal to the plane of the galaxy, v_z (Figure B-1). For a galaxy inclined at an angle i with the lm plane, the line of sight velocity is

$$v(r,\phi) = v_o + v_r(r,\phi)\sin(\phi)\sin(i) + v_\phi(r,\phi)\cos(\phi)\sin(i) + v_z(r,\phi)\cos(i) \qquad \text{(B-1)}$$

Three model velocity fields are presented (Figure B-2). The galaxy is assumed to be a circular disk and v_z is zero. The axis of inclination (major axis of the projected ellipse) lies along l. The inclination is 45°. The fields are radially symmetrical, and only the right portion is shown. The systemic velocity is arbitrary. It only changes the numerical values of the velocities, and has no effect on the shape of the fields. The point of reference is taken to be the center of the disk.

The velocity field of a solid disk rotating at an angular velocity Ω_g is a set of parallel constant velocity contours normal to the major axis. The radial velocity is zero and the rotational velocity is

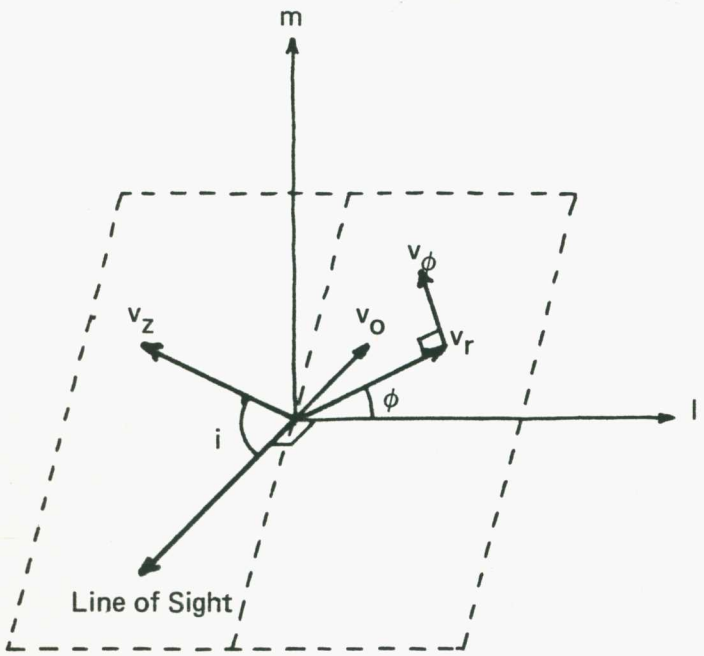

Figure B-1 Component Velocities in Galactic Motion

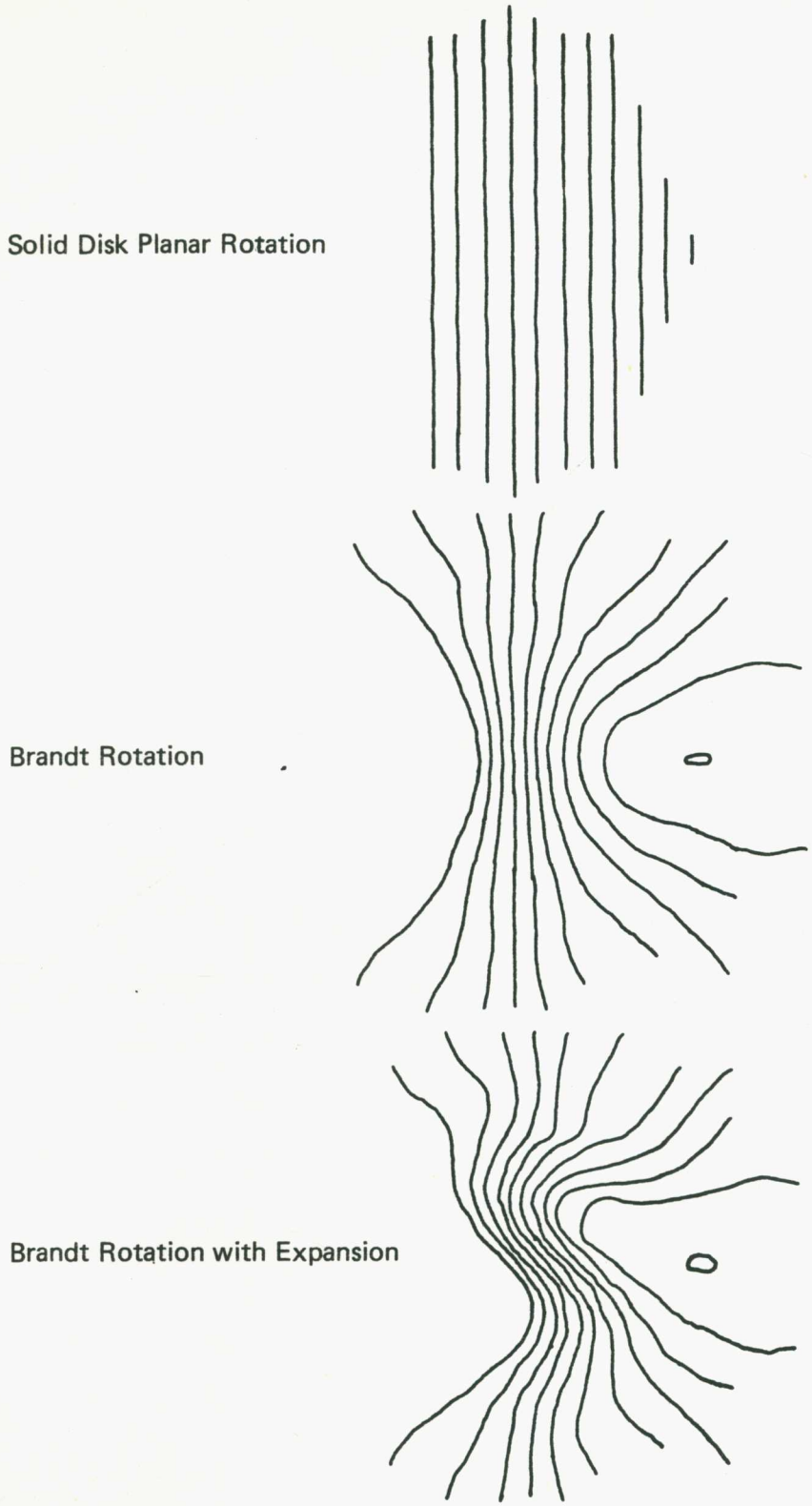

Figure B-2 Model Velocity Fields

$$v_\phi(r,\phi) = r\Omega_g \qquad \text{(B-2)}$$

A galaxy is not well represented by a solid rotational disk. The distribution of matter is not uniform and there is differential circular motion. The velocity field is obtained for the case where the differential motion is described by the Brandt curve (Brandt 1960)

$$v_\phi(r,\phi) = (r/r_{max})/\{1/3 + 2/3 \times (r/r_{max})^n\}^{3/(2n)} \times v_{\phi_{max}} \qquad \text{(B-3)}$$

The rotational velocity attains a maximum value of $v_{\phi_{max}}$ at the radius r_{max} (the turnover radius) and then decreases at a rate governed by n. In the model, r_{max} is half the radius of the disk and n is unity. The radial velocity is zero. The closed velocity contour encloses the turnover point on the major axis of the projected galaxy.

An expanding galaxy has in addition a radial velocity. This is added to the previous model. The radial velocity is assumed to be

$$v_r(r \leq r_{max},\phi) = (1 - r/r_{max})v_{\phi_{max}} \qquad \text{(B-4)}$$
$$v_r(r > r_{max},\phi) = 0$$

The symmetry of the velocity field with respect to the l and m axes observed in the previous two models disappears in this third model. The closed contour again identifies the turnover point on the major axis. The velocity contours at the right form an upward bending wedge around the galactic center. If either the radial or the rotational velocity reverses its direction, the wedge will bend downwards around the center.

Reference

Brandt, J. C. "On the Distribution of Mass in Galaxies. I. The large-scale Structure of Ordinary Spirals with Applications to M31", Astrophys. J., vol. 131, 293-303, 1960.